



Titre: An Investigation on the Dynamics of Epileptic Networks and
Title: Mechanisms Underlying Different Ictal Patterns

Auteur: Leila Abrishami Shokooh
Author:

Date: 2021

Type: Mémoire ou thèse / Dissertation or Thesis

Référence: Abrishami Shokooh, L. (2021). An Investigation on the Dynamics of Epileptic
Citation: Networks and Mechanisms Underlying Different Ictal Patterns [Ph.D. thesis,
Polytechnique Montréal]. PolyPublie. <https://publications.polymtl.ca/9192/>

 **Document en libre accès dans PolyPublie**
Open Access document in PolyPublie

URL de PolyPublie: <https://publications.polymtl.ca/9192/>
PolyPublie URL:

**Directeurs de
recherche:** Frédéric Lesage, Dang Khoa Nguyen, & Philippe Pouliot
Advisors:

Programme: Génie biomédical
Program:

POLYTECHNIQUE MONTRÉAL

affiliée à l'Université de Montréal

**An investigation on the dynamics of epileptic networks and mechanisms
underlying different ictal patterns**

LEILA ABRISHAMI SHOKOOH

Institut de génie biomédical

Thèse présentée en vue de l'obtention du diplôme de *Philosophiæ Doctor*

Génie biomédical

Aout 2021

POLYTECHNIQUE MONTRÉAL

affiliée à l'Université de Montréal

Cette thèse intitulée :

**An investigation on the dynamics of epileptic networks and mechanisms
underlying different ictal patterns**

présentée par **Leila ABRISHAMI SHOKOOH**

en vue de l'obtention du diplôme de *Philosophiæ Doctor*

a été dûment acceptée par le jury d'examen constitué de :

Alain VINET, président

Frédéric LESAGE, membre et directeur de recherche

Dang Khoa NGUYEN, membre et codirecteur de recherche

Philippe POULIOT, membre et codirecteur de recherche

Karim JERBI, membre

Igor TIMOFEEV, membre externe

DEDICATION

To you, Mojtaba

ACKNOWLEDGEMENTS

I would like to take this opportunity to acknowledge and thank everyone who has helped me throughout my Ph.D journey. First, I would like to express my gratitude to my supervisors Prof. Dang Khoa Nguyen and Prof. Frédéric Lesage who guided and supported me in my research.

I would also like to thank our colleagues and collaborators at CHUM and Polytechnique de Montréal: Dr. Philippe Pouliot, Dr. Denahin Toffa and Manon Robert whose helps have substantially improved my work.

I feel deeply thankful to my parents who has always supported and encouraged me.

Last but not least, my special thanks to my love, my husband Mojtaba, who has brightened my world and made me stronger.

RÉSUMÉ

L'étude de la dynamique des activités ictales aussi bien que les mécanismes sous-jacents qui les génèrent sont d'une importance cruciale pour améliorer notre compréhension de l'ictogénèse. Les crises ont déjà été étudiées pour comprendre les transitions d'états ictaux; cependant, ces tentatives ont généré des résultats contradictoires. Par exemple, certains résultats indiquent une connectivité très variable pendant les crises et une connectivité relativement stable dans les périodes pré-ictale et post-ictale [1] tandis que d'autres ont trouvé des changements rapides dans la géométrie du réseau aux moments de pré-crise et des changements géométriques plus lents pendant l'activité ictale ou aucune différence significative entre les taux de transition d'état ictale, pré-ictale et post-ictale [2,3]. Ces observations discordantes nous ont amenés à réexaminer la dynamique des transitions d'état au cours des crises. La transition des activités interictales aux activités ictales a également été largement étudiée pour améliorer notre compréhension des mécanismes sous-jacents de la génération de crises. Cependant, il est méconnu si les crises avec des patrons EEG distincts lors de leur initiation sont précédées par des interactions de réseau variables et si différents mécanismes neurophysiologiques sous-tendent des crises avec patrons EEG distincts lors de leur initiation.

Pour mieux comprendre comment le cerveau épileptique en tant que système dynamique module ses états, en utilisant différentes mesures de connectivité fonctionnelle, nous avons identifié des modèles d'états récurrents et étudié la dynamique des transitions d'états ictales à différentes échelles : localement et globalement. Nos résultats pointent vers des dynamiques distinctes pour les transitions d'état à ces différentes échelles spatiales. Alors que le modèle de transitions d'état global a conduit à la conclusion que le cerveau change d'état moins fréquemment pendant l'activité ictale, localement, il a subi un taux plus élevé de transitions d'état. De plus, nos résultats montrent différents modèles de transitions d'état dans la zone d'apparition des crises entre les patients sans crise (SC) et avec crise (AC) en postopératoire, ce qui pourraient avoir une application pratique dans la prédiction des résultats chirurgicaux (Chapitre 4, Article 1). Nous avons approfondi l'étude des transitions d'état ictal et étudié la transition des activités interictales aux activités ictales. Plus précisément, nous avons exploré si les interactions du réseau avant la génération de crises avec différents patrons EEG lors de leur initiation. À cette fin, nous avons classé 103 crises EEG intracrâniennes de 20 patients atteints d'épilepsie focale résistante aux médicaments basés sur le patron EEG lors de leur initiation. Nous avons ensuite étudié les interactions du réseau avant leur génération en calculant des matrices de connectivité fonctionnelle dirigée. Nos observations

suggèrent qu'à l'échelle du réseau, différentes interactions précèdent la génération de crises avec patron EEG distinct lors de leur initiation (chapitre 5, article 2). Ce résultat a soulevé une question importante quant à savoir si différents mécanismes physiologiques sous-tendent la génération de crises avec patron EEG distinct lors de leur initiation? En utilisant un modèle informatique qui prend en compte certains des événements physiologiques les plus pertinents (par exemple, le blocage de la dépolarisation, l'effondrement et la récupération de l'activité inhibitrice) et différents scénarios d'activité excitatrice-inhibitrice déséquilibrée, nous avons abordé cette question et exploré si les crises avec patron EEG distinct lors de leur initiation proviennent de différents mécanismes sous-jacents. Nos résultats de modélisation ont révélé que, selon le niveau d'excitation, des crises pourraient potentiellement être générées en raison à la fois de l'augmentation et de l'effondrement de l'inhibition pour des gammes de paramètres spécifiques. Alors que l'effondrement de l'inhibition a été largement rapporté comme un mécanisme principal sous-jacent à la génération de crises [4–7], certaines études expérimentales ont abordé l'augmentation de l'activité inhibitrice avant et au tout début des activités ictales [8–14]. Notre approche de modélisation pourrait unifier ces mécanismes apparemment contradictoires suggérés par les études expérimentales précédentes pour l'implication de l'activité inhibitrice dans la génération de crises [4–11,13,14] et reproduit avec succès certains des modèles d'apparition de crises couramment observés. Nos résultats ont indiqué que les crises avec patron EEG distinct lors de leur initiation peuvent, en fait, résulter de différents mécanismes sous-jacents (chapitre 6, article 3).

Dans l'ensemble, dans cette thèse, nous avons étudié la dynamique et la génération d'événements ictales à différentes échelles et sous différentes perspectives. Nous avons exploré différentes mesures fonctionnelles de connectivité de réseau pour mieux comprendre les transitions d'état ictale. Ensuite, les crises avec patron EEG distinct lors de leur initiation ont été classées et étudiées pour voir si différentes interactions de réseau précèdent leur génération. Enfin, en construisant un modèle, nous avons étudié les mécanismes qui pourraient générer des crises avec patrons EEG distincts lors de leur initiation et suggéré des voies pour la génération de crises qui pourraient expliquer certains mécanismes de génération de crises contradictoires observés dans les expériences.

ABSTRACT

Studying the dynamic of ictal activities as well as the underlying mechanisms generating them are of crucial importance for enhancing our understanding of ictogenesis. Seizures have previously been investigated to understand ictal state transitions; however, these attempts have generated conflicting results. For instance, some findings point towards highly varying connectivity during seizures and relatively stable connectivity in pre-ictal and post-ictal periods [1] while others have found rapid changes in network geometry in pre-seizure epochs and slower geometric changes during ictal activity or no significant differences among the ictal, pre-ictal and post-ictal state transition rates [2,3]. These discrepant observations led us to reexamine the dynamic of state transitions during seizures. The transition from interictal into ictal activities has also been widely investigated to enhance our understanding of the underlying mechanisms of seizure generation. However, it remains largely unclear whether seizures with distinct onset patterns are preceded by varying network interactions and whether different neurophysiological mechanisms underly different seizure onset patterns.

To better understand how the epileptic brain as a dynamical system modulates its states, using different functional connectivity measures, we identified patterns of recurrent states and investigated the dynamic of ictal state transitions on different scales: locally and globally. Our findings point towards distinct dynamics for state transitions at these different spatial scales. While the pattern of global state transitions led to the conclusion that the brain changes state less frequently during ictal activity, locally, it underwent a higher rate of state transitions. Further, our results show different patterns of state transitions in the seizure-onset-zone between seizure-free (SF) and non-seizure-free (NSF) patients which could have a practical application in predicting surgical outcome (*Chapter 4, Article 1*). We further expanded the study of ictal state transitions and investigated the transition from interictal to ictal patterns. More precisely, we explored if the network interactions before the generation of seizures with different onset patterns vary. To this end, we classified seizure onset patterns of 103 intracranial EEG seizures from 20 patients with drug-resistant focal epilepsy. We then surveyed network interactions prior to the generation of distinct seizure onset patterns by calculating directed functional connectivity matrices. Our observations suggest that, at the network scale, different interactions precede the generation of different seizure onset patterns (*Chapter 5, Article 2*). This result raised an important question of whether different physiological mechanisms underly different seizure onset patterns? By

employing a computational framework that takes into account some of the most relevant physiological events (e.g., depolarization block, collapse, and recovery of inhibitory activity) and different scenarios of imbalanced excitatory-inhibitory activity, we addressed this question and explored whether seizures with different onset patterns stem from different underlying mechanisms. Our modeling results revealed that, depending on the excitation level, seizures could potentially be generated due to both enhancement and collapse of inhibition for specific ranges of parameters. While the collapse of inhibition has been widely reported as a main mechanism underlying seizure generation [4–7], some experimental studies have addressed the enhanced inhibitory activity before and at the very onset of ictal activities [8–14]. Our modeling approach could unify these seemingly contradictory mechanisms suggested by the previous experimental studies for the involvement of inhibitory activity in seizure generation [4–11,13,14] and successfully reproduced some of the commonly observed seizure onset patterns. Our findings indicated that different onset patterns can, in fact, arise from different underlying mechanisms (*Chapter 6, Article 3*).

Taken together as a whole, in this thesis we investigated the dynamic and generation of ictal events at different scales and from different perspectives. We explored different functional network connectivity measures to better understand the ictal state transitions. Then, seizure onset patterns were classified and investigated to see if different network interactions precede seizures with different onset patterns. Finally, by constructing a computational model, we investigated the mechanisms that could generate seizures with different onset patterns and suggested pathways for seizure generation that could explain some contradicting seizure generation mechanisms observed in experiments.

TABLE OF CONTENTS

DEDICATION	III
ACKNOWLEDGEMENTS	IV
RÉSUMÉ.....	V
ABSTRACT.....	VII
TABLE OF CONTENTS	IX
LIST OF TABLES	XI
LIST OF FIGURES.....	XII
LIST OF SYMBOLS AND ABBREVIATIONS.....	XVII
LIST OF APPENDICES	XVIII
CHAPTER 1 INTRODUCTION.....	1
1.1 Epilepsy and epileptic seizures	1
1.2 The Neurobiology of Seizures.....	1
1.2.1 Ionic environment	1
1.2.2 Synaptic transmission.....	2
1.2.3 Neuronal network.....	2
1.3 Electroencephalography and epilepsy.....	3
1.4 Functional brain networks.....	4
1.5 Intracranial EEG seizure onset patterns	5
1.6 Computational models of ictal EEG.....	7
1.6.1 Biophysical network models	7
1.6.2 Integrate and fire neural network	8
1.6.3 Phenomenological models.....	9
1.6.4 Neural mass models	9
CHAPTER 2 LITERATURE REVIEW.....	11
2.1 Functional connectivity network in epilepsy	11
2.2 Dynamic of ictal state transition.....	11
2.3 Interictal to ictal transition: seizure generation	12
2.3.1 Seizure generation and impaired excitation-inhibition balance	12
2.3.2 Ictal patterns and impaired E-I balance.....	14
2.3.3 Models of spatiotemporal patterns of seizure onset	14
2.4 Research overview	15
CHAPTER 3 THEORY AND METHODOLOGY	19
3.1 Functional connectivity measures	19
3.1.1 Cross-correlation	19
3.1.2 Coherence.....	19
3.1.3 Phase locking value.....	20
3.1.4 Recurrence Plot, Recurrence Quantification Analysis, and Joint Recurrence Plot.....	20
3.1.5 Phase slope index	23
3.2 Jansen model: Neural mass model of cortical columns	24
3.2.1 Cortical columns	24
3.2.2 Jansen’s model of cortical columns	25
CHAPTER 4 ARTICLE 1: IDENTIFICATION OF GLOBAL AND LOCAL STATES DURING SEIZURES USING QUANTITATIVE FUNCTIONAL CONNECTIVITY AND RECURRENCE PLOT ANALYSIS.....	28
4.1 Introduction	29

4.2	Methodology	30
4.2.1	Patient population and intracranial EEG recordings	30
4.2.2	Pre-processing	31
4.2.3	Analysis	31
4.3	Results	39
4.3.1	Patient population	39
4.3.2	State transition	40
4.4	Discussion	47
4.5	Conclusion	49
CHAPTER 5 ARTICLE 2: INTRACRANIAL EEG SEIZURE ONSET AND TERMINATION PATTERNS AND THEIR ASSOCIATION		51
5.1	Introduction	52
5.2	Methodology	53
5.2.1	Patients	53
5.2.2	Pre-processing	54
5.2.3	Seizures	54
5.2.4	Analysis	55
5.3	Results	58
5.3.1	Seizure onset and termination patterns	59
5.3.2	Pattern distributions and their associations	61
5.3.3	The Flow Index and seizure patterns	63
5.4	Discussion	64
5.5	Conclusion	66
CHAPTER 6 ARTICLE 3: COMPUTATIONAL MODELING OF SEIZURE ONSET PATTERNS TO UNDERPIN THEIR UNDERLYING MECHANISMS		67
6.1	Introduction	68
6.2	Materials and Methods	70
6.3	Results	73
6.4	Discussion	83
CHAPTER 7 GENERAL DISCUSSION		87
CHAPTER 8 CONCLUSION AND RECOMMANDATIONS		92
REFERENCES		95
APPENDICES		130

LIST OF TABLES

Table 4-1 summary of the patients' clinical characteristics. SW = Spike and Wave; FLVA = Fast Low-Voltage Activity, IFG = inferior frontal gyrus; ITG = inferior temporal gyrus; STG = superior temporal gyrus, IPL = inferior parietal lobule, SMA = supplementary motor area, Ins = insular, OF = orbitofrontal, CPC = complex partial seizure, SPS = simple partial seizure, ES = electrical seizure.....	40
Table 4-2 The number of seizures and channels for each patient along with descriptive statistics on seizure duration.	42
Table 4-3 The patient-specific frequency bands and number of unique global states computed for each method.....	43
Table 4-4 a) Comparing global state transition rates between pre-ictal, ictal and post-ictal periods using one-way ANOVA conducted separately for SF and NSF patients. b) The adjusted p-values ($p\text{-value}_{adj}$) based on the post-hoc analysis using Tukey-Kramer test to control for the family-wise error rate of 5% (FWER = 5%).	44
Table 4-5 a) Calculated p-values for RQA measures for SF patients using one-way ANOVA. b) The adjusted p-values based on the post-hoc analysis of Table 5a using Tukey-Kramer test to control for the family-wise error rate of 5% (FWER = 5%).	45
Table 4-6 a) Calculated p-values for RQA measures for NSF patients using one-way ANOVA. b) The adjusted p-values based on the post-hoc analysis of Table 6a using Tukey-Kramer test to control for the family-wise error rate of 5% (FWER = 5%).	45
Table 5-1 Summary of the patients' clinical characteristics. IFG = inferior frontal gyrus; ITG = inferior temporal gyrus; STG = superior temporal gyrus, IPL = inferior parietal lobule, SMA = supplementary motor area, Ins = insular, OF = orbitofrontal, FUS = focal unaware seizure, FAS = focal aware seizure, ES = electrical seizure.....	57
Table 6-1 The model parameters used in Eq.6-1 and Eq.6-2.	72
Table 6-2 The values used for the simulated patterns. LVFA=Low Voltage Fast Activity, rSW=rhythmic Spike and Wave, HAFA=High Amplitude Fast Activity.....	83

LIST OF FIGURES

- Figure 1-1 Invasive and non-invasive electroencephalography electrodes. Non-invasive EEG electrodes are placed on the scalp surface and invasive EEG is recorded from intracranially implanted electrodes either with stereotactically inserted depth electrodes (sEEG) or electrodes placed directly on the neocortex (ECoG).4
- Figure 1-2 Intracranial EEG seizure onset patterns. a) Low-voltage fast activity recorded with electrodes located at right hippocampus, b) Low-frequency high-amplitude periodic spikes recorded with electrodes located at right hippocampus, c) Sharp activity recorded with electrodes located at left lingual gyrus, d) Spike-and-wave activity recorded with electrodes located at left hippocampus, e) Burst of high-amplitude polyspikes recorded with electrodes located at anterior aspect of right supplementary motor area, f) Burst suppression recorded with electrodes located at left orbitofrontal cortex, g) Delta brush recorded with electrodes located at left infero-parietal region (from Ref. [59]).6
- Figure 3-1 Recurrence plots of different time series. (A) homogeneous pattern representing uniformly distributed noise, (B) the checkboard pattern representing a periodic time series, (C) the pattern for a time series with drift and (D) disrupted patterns for Brownian motion noise [from Ref. [242]].22
- Figure 3-2 Phase slope index (PSI). a) phase differences between two signals in blue and red for three different frequencies b) The linear relationship between the phase differences versus frequencies for the signals presented in (a) (from Ref. [247]).23
- Figure 3-3 Six cortical layers represented by three different staining techniques (from Ref. [250]).25
- Figure 3-4 A representation of the computational model of a single cortical column. The average pulse density of the presynaptic neurons is transformed to average postsynaptic membrane potential by $h_e(t)$, $h_i(t)$ blocks. The Sigm blocks represent the static nonlinear sigmoid function converting the input potential of each population to average output pulse density (from Ref. [251]).26
- Figure 4-1 r-spectrum for 12 seizures of patient 1 averaged over all channels (colored lines) and the averaged r-spectrum for patient 1 over all 12 seizures (black line). For this patient, the beta band is the one with the largest modulation. The sharp drops at 60 and 120 Hz are due to the application of the notch filter.32
- Figure 4-2 A pictorial guide for the computation of the functional connectivity matrix of a 1s time-window based on PLV between channels 70 and 15 of seizure 1 from patient 1 (method III). The instantaneous phases for each time window are computed using Hilbert transform and $\lambda_{70,15}(m)$ is calculated based on equation 4-3. m denotes the window number.33
- Figure 4-3 a) recordings from seven channels of patient 1 (the total number of channels for this patient is 110). The dotted black lines at $t=0s$ and $t=78s$ delineate seizure onset and offset respectively. b) functional connectivity matrices based on coherence $C(m)$ for each 3s window of the recordings calculated based on equation 4-2 (method II). c) the configuration matrix constructed from all the unique pairwise connections of the normalized coherence matrices (averaged normalized coherence $\hat{C}(m)$). One configuration vector is shown on this figure with a dotted black line at $t=-52s$ (preictal). d) the configuration similarity matrix for the ictal period. Different states are identified based on section 4.3.3 and depicted with the black rectangles on this configuration similarity matrix.34

- Figure 4-4 a) The recording from one SOZ channel recorded from a patient in our database. The pre-ictal, ictal and post-ictal periods as depicted in blue, red and black respectively (these periods have the same duration). b) RPs for pre-ictal, ictal and post-ictal periods for the recording presented in (a). c) RQA measures calculated based on diagonal and vertical structures of the RPs in (b). The left panel shows DET calculated based on diagonal structures and the right panel represents LAM calculated based on the vertical structures. As we can see Ictal period displays lower values for both measures.36
- Figure 4-5 a) Rate of global state transition for patients with Engel I surgery outcome (SF). The lines show 95% confidence intervals. b) Rate of global state transition for patients with Engel II surgery outcome (NSF). The lines show 95% confidence intervals.42
- Figure 4-6 The number of unique global states identified in pre-ictal, ictal and post-ictal periods for all seizures using four different methods. For method I, the number of unique states during the ictal period did not show a significant difference from pre- and post-ictal periods. However, for method II it was significantly lower than the post-ictal period (p -value <0.05) and for method III and JRPs the number of unique states was remarkably lower than both other periods with p -value <0.05 and p -value <0.001 respectively.42
- Figure 4-7 *The comparison of global state transition rate during ictal activity between SF and NSF patients. None of the applied methods (I-IV) reported significant difference between these two groups (p -value >0.05).*44
- Figure 4-8 *RQA measures averaged over three different channel groups (seizure onset channels (SOZ), the channels to which the seizure propagated within the first 10s of ictal activity (Prop) and the channels with no ictal activity during the seizure (NoIct)) a) for SF patients. b) for NSF patients. The lines show the 95% confidence intervals over seizures.*46
- Figure 4-9 *Comparing RQA measures averaged over three different channel groups (seizure onset channels (SOZ), the channels to which the seizure propagated within the first 10s of ictal activity (Prop) and the channels with no ictal activity during the seizure (NoIct)) between SF and NSF patients. The lines show the 95% confidence intervals over seizures.* 47
- Figure 5-1 Calculating Flow Index (FI) for seizures with a1) slow and b1) fast onset patterns. The PSI matrices in gamma frequency band during the preictal periods (highlighted in a1 and b1) of recordings with slow and fast onsets are respectively displayed in top (a2) and (b2). In bottom (a2) and (b2) the averaged inflow and outflow to seizure onset zones are presented for the corresponding functional connectivity matrices. The Flow Index (FI) for these two networks are calculated based on Eq.5-1 and shown on the left side of the figure.....56
- Figure 5-2 Nine seizure onset patterns: a) Low Voltage Fast Activity (LVFA) recorded with an electrode located within the SOZ (Left superior temporal gyrus) of a patient with Engel-I surgery outcome, b) LVFA on a wave recorded with an electrode located within the SOZ (right inferior frontal gyrus) of a patient with Engel-I surgery outcome, c) High Amplitude Fast Activity (HAFA) recorded with an electrode located within the SOZ (insular) of a patient with Engel-I surgery outcome, d) Low Frequency High Amplitude (LFHA) recorded with an electrode located within the SOZ (left temporo-parietal junction) of a patient with Engel-II surgery outcome, e) rhythmic Spike/PolySpike and Wave (rSW/rPSW) recorded with an electrode located within the SOZ (left anterior insular) of a patient with Engel-II surgery outcome, f) rSW followed by LVFA recorded with an electrode located within the SOZ (left pre-central gyrus) of a patient with Engel-I surgery outcome, g) delta rhythmic activity recorded with an electrode located within the SOZ (Left insular) of a patient with Engel-II surgery outcome, h) rhythmic θ/α recorded with an electrode located within the SOZ (right orbitofrontal) of a patient with Engel-I surgery outcome, i) delta brush recorded

- with an electrode located within the SOZ (left mesial temporal) of a patient with Engel-I surgery outcome. The stars depict seizure onset time.60
- Figure 5-3 Six seizure termination patterns: a) rhythmic Spike and Wave (rSW/rPSW), b) High Amplitude Fast Activity (HAFA), c) rhythmic θ/α , d) rhythmic spikes, e) Burst Suppression (BS), f) delta brush. The stars depict seizure termination time.61
- Figure 5-4 Pie chart representing the prevalence of nine seizure onset and seven seizure termination patterns. The sliced region in (a) shows the percentage of all onset patterns starting with Low Voltage Fast Activity (LVFA) and the sliced region in (b) represents the percentages of all termination patterns with Burst Suppression (BS) pattern.62
- Figure 5-5 Histogram depicting the percentage of each seizure termination patterns for each seizure onset pattern. Numbers indicate the number of seizures per subgroup.62
- Figure 5-6 Histogram showing the percentage of each (a) seizure onset and (b) seizure termination patterns for all termination region categories (In, Out, In-Out, Diffuse). Numbers indicate the number of seizures per subgroup.63
- Figure 5-7 Calculated Flow Index (FI) of the recordings prior to two seizure onset groups: fast and slow. Fast group includes seizures with LVFA, LVFA on a wave and HAFA onset patterns and slow group includes the rSW/rPSW, delta rhythmic activity, LFHA, rhythmic θ/α onset patterns. The lines show 95% confidence intervals. Single star denotes significant results with p -value <0.05 and double star shows significant results with p -value <0.00164
- Figure 6-1 Excitatory inhibitory neuronal populational model and the activation functions. (a) The neuronal population model which is composed of excitatory and inhibitory components: pyramidal cells (PYR), excitatory interneurons (E), dendrite targeting inhibitory interneurons (I_d) and soma targeting inhibitory interneurons (I_s). (b) The nonlinear activation function of a neural population that relates the average postsynaptic potential to an average firing rate for that population. The dotted black curve represents the commonly used sigmoid function and the solid black curve shows the activation function we used which considers depolarization block. (c) Decreasing the depolarization block threshold for the inhibitory populations. In this figure, the red activation function has a lower depolarization block threshold ($\theta = 0$) compared to the black activation function ($\theta = 4$). 70
- Figure 6-2 Model simulations vs. real iEEG ictal recordings. The signals in blue are the simulated signals produced by our computational model and the signals in grey are the real depth iEEG recordings for (a) background, (b) Low Voltage Fast Activity (LVFA), (c) rhythmic slow spikes/sharp waves, (d) rhythmic Spike and Wave (rSW), (e) High Amplitude Fast Activity (HAFA), (f) rhythmic α/β and (g) burst suppression ictal activities.74
- Figure 6-3 The results from the Monte Carlo simulation. The colors represent the most probable pattern of ictal activity for each one-unit interval of the parameters A, B, and G with $\theta_d = \theta_s = 4$ for the left column and $\theta_d = \theta_s = 0$ for the right column.75
- Figure 6-4 The ranges of parameters B and G generating background activity. (a) For $A=3.5$ and $\theta_d = \theta_s = 4$, (b) for $A=3.5$ and $\theta_d = \theta_s = 0$ (c) for $A=7.5$ and $\theta_d = \theta_s = 0$. The region in blue represents background activity while the region in white corresponds to the range of parameters that did not result in a background activity.76
- Figure 6-5 Seizure generation with low preictal excitation. The seizure onset patterns in the left and right columns are respectively generated starting from the background activities represented in Fig.6-4a and Fig. 6-4b. The underlying mechanism that generated the patterns in the left column is the collapse of (a) soma targeting inhibitory interneurons ($\theta_s: 4 \rightarrow 0$), (b) dendrite targeting inhibitory interneurons ($\theta_d: 4 \rightarrow 0$), (c) both dendrite and soma

targeting inhibitory interneurons ($\theta_d: 4 \rightarrow 0, \theta_s: 4 \rightarrow 0$) and the mechanism responsible for the generating the onset patterns in the right column is the recovery of (d) soma targeting inhibitory interneurons ($\theta_s: 0 \rightarrow 4$), (e) dendrite targeting inhibitory interneurons ($\theta_d: 0 \rightarrow 4$), (f) both dendrite and soma targeting inhibitory interneurons ($\theta_d: 0 \rightarrow 4, \theta_s: 0 \rightarrow 4$). The region in white shows the range of parameters for which there was no background activity to start from and explore the transition to ictal patterns.....77

Figure 6-6 Low Voltage Fast Activity (LVFA) and rhythmic α seizure onset patterns. (a) LVFA seizure onset pattern with low excitation level (i.e., $A=3.5$). The parameters for the generation of this pattern are chosen from the ranges displayed in Fig. 6-5d and are presented in Table 6-2. (b) Rhythmic α seizure onset pattern with low excitation level (i.e., $A=3.5$) and parameters B and G from Fig. 6-5b. (c) The mechanism responsible for the generation of this onset pattern in (a) which is increasing the depolarization block threshold for some targeting interneurons (I_s). (d) The mechanism responsible for the generation of this onset pattern in (b) which is decreasing the depolarization block threshold for dendrite targeting interneurons (I_D).....78

Figure 6-7 Seizure generation with high preictal excitation. These seizure onset patterns are generated starting from the background activity represented in Fig. 6-4c. The underlying mechanism generating these patterns is the recovery of (a) soma targeting inhibitory interneurons ($\theta_s: 0 \rightarrow 4$), (b) dendrite targeting inhibitory interneurons ($\theta_d: 0 \rightarrow 4$), (c) both dendrite and soma targeting inhibitory interneurons ($\theta_d: 0 \rightarrow 4, \theta_s: 0 \rightarrow 4$). The region in white shows the range of parameters for which there was no background activity to start from and explore the transition to ictal patterns.....79

Figure 6-8 Rhythmic spike and wave (rSW) and rhythmic α seizure onset patterns. (a) RSW and (b) rhythmic α seizure onset patterns generated with the parameters B and G chosen from Fig. 6-7a (Table 6-2). (c) The mechanism that resulted in the generation of these two patterns in our model which is the recovery of the soma targeting interneurons and the consequent removal of the depolarization block of the excitatory population.80

Figure 6-9 An example for the 3-dimensional representation of the excitatory and inhibitory activation functions. (a) The dynamic change of the inhibitory activation function due to an increased threshold for the depolarization block of this population results in enhanced inhibitory activation. (b) The excitatory population is being drawn out of depolarization block due to its inhibitory input shown in (a).81

Figure 6-10 High Amplitude Fast Activity (HAFA) and burst suppression seizure onset patterns. (a) HAFA and (b) burst suppression seizure onset patterns generated with the parameters chosen from Fig. 6-7b (Table 6-2). The DC shift from the background to ictal activity is removed in this simulated signal. (c) The mechanism responsible for the generation of the onset patterns is shown in (a) and (b). The recovery of dendrite targeting inhibitory interneurons draws the excitatory population out of the depolarization block and initiates seizures.....81

Figure 6-11 Rhythmic slow spikes seizure onset pattern. (a) Rhythmic slow spikes seizure onset pattern which is generated with the parameters chosen from Fig. 6-7c. The DC shift from the background to ictal activity is removed in this simulated signal. (b) The mechanism resulting in the generation of the onset patterns shown in (a) which is the recovery of both dendrite and soma targeting inhibitory interneurons and the consequent removal of the depolarization block of the excitatory population.....82

Figure 6-12 A schematic figure depicting our suggested seizure onset and termination pathways considering the depolarization block mechanism. Depending on the initial excitability state, enhancing the excitation level could result in both seizure generation (Onset I) and termination (Termination I), similarly, decreasing the excitation level could result in both seizure generation (Onset II) and termination (Termination II).....	84
Figure 8-1 A visual summary of the main findings of this thesis. (a) Our main research questions displayed as Q ₁ to Q ₄ . (b) Our findings presented as A ₁ to A ₄ which respectively answer questions Q ₁ to Q ₄	94

LIST OF SYMBOLS AND ABBREVIATIONS

This list presents the symbols and abbreviations used in the thesis or dissertation in alphabetical order, along with their meanings.

4-AP	4-aminopyrimidine
BS	Burst Suppression
DET	Determinism
Diffuse	The ictal activity upon seizure termination is in all channels
D _{In}	Ingoing links
D _{Out}	Outgoing links
DRE	Drug-resistant epilepsy
E-I	Excitatory-Inhibitory
ECoG	Electrocorticography
EEG	Electroencephalographic
FI	Flow index
fMRI	Functional MRI
HAFA	High amplitude fast activity
In	The ictal activity upon seizure termination is limited to SOZ
In-Out	The ictal activity upon seizure termination is in both SOZ and NonSOZ but not in all channels
JRP	Joint recurrence plot
LAM	Laminarity
LFHA	Low frequency high amplitude
LVFA	Low voltage fast activity
MEG	Magnetoencephalography
MRI	Magnetic resonance imaging
NoIct	Channels with no ictal activity during the seizure
Non-SOZ	Non-seizure-onset-zone
NSF	Non-seizure-free (after surgery)
Out	The ictal activity upon seizure termination is in Non-SOZ
PET	Positron emission tomography
PSI	Phase slope index
PLV	Phase Locking Value
Prop	Channels to which the seizure propagated within the first 10s of ictal activity
RP	Recurrence plot
RQA	Recurrence quantification analysis
rSW/rPSW	Rhythmic spike/polyspike and wave
sEEG	stereoelectroencephalography
SF	Seizure-free (after surgery)
SOZ	Seizure onset zone
SPECT	Single-photon emission computed tomography

LIST OF APPENDICES

Appendix A130
Appendix B139
Appendix C141

CHAPTER 1 INTRODUCTION

1.1 Epilepsy and epileptic seizures

Epilepsy, commonly characterized by the emergence of recurrent and spontaneous transient behavioral manifestations due to abnormal excessive neural activity, is one of the most common and most disabling neurological disorders [15]. It can occur across all age groups [16] and affects 50 million people worldwide [17]. Epilepsy can be due to gliosis from acquired causes (e.g., stroke, trauma, hypoxia, infections, autoimmune diseases), brain malformations, tumors, vascular malformations or genetic mutations; in many patients, the cause remains unknown [15]. About 30% of patients with epilepsy do not respond to available antiseizure medications and alternate treatment such as resective surgery, neurostimulation and dietary therapies may be considered [18]. Epileptic seizures are generally classified as *focal* and *generalized* seizures. Focal seizures arise from a circumscribed region in the brain whereas generalized seizures involve bilateral hemispheres rapidly [19].

1.2 The Neurobiology of Seizures

To gain a better understanding of how seizures can be generated, it would be beneficial to recap the fundamentals of neuronal activities as well as their transmembrane properties and synaptic transmission. Diverse mechanisms have been suggested to underly seizure generation and below, at three different levels, we discuss some of the most widely addressed mechanisms.

1.2.1 Ionic environment

The neuronal activity depends on its ionic environment which forms the electrochemical gradients and gives rise to neuronal electrical activity. Therefore, at the most fundamental level, here we review the effect of the neurons ionic environment on their excitability and generation of ictal events.

The major extracellular cation is sodium while potassium forms the main intracellular cation and the imbalance of these cations can result in abnormal activities [20,21]. Ion channels are crucial for neural activity. Voltage-gated sodium channels play an essential role in the initiation and propagation of action potential while the opening of potassium channels draws the membrane potential back to its resting potential [22]. The activity of voltag-gated calcium channels not only

can change the membrane potential but also is involved in neurotransmitter release (e.g., [23]). A considerable proportion of chloride channels are GABA-gated and these channels are pivotal in regulating neuronal excitability [24]. Abnormality of these sodium, potassium, calcium and chloride channels have been extensively studied and suggested to be involved in epileptogenesis (e.g., [21]).

Another mechanism that maintain the transmembrane balance of different ions is the activity of ion pumps. Ion pumps are membrane pores that consume energy derived from adenosine triphosphate (ATP), an organic compound that provides energy in living cells [25]. Therefore, malfunction of ion pumps and more specifically the sodium/potassium pump can lead to seizure which has been reported in experimental models of epilepsy [26–29].

1.2.2 Synaptic transmission

Synaptic transmission is important in controlling the excitation inhibition balance. Previous studies have shown that malfunction of the diverse molecular mechanisms involved in synaptic transmission could result in epilepsy [30].

Glutamate and GABA, respectively, as the main excitatory and inhibitory neurotransmitters have been extensively studied (e.g., [31]). However, these neurotransmitters do not always exert a direct effect on seizure generation. GABA receptors are mainly permeable to chloride which usually flows into the cell down its concentration gradient and hyperpolarize the cell. Though, if the chloride concentration gradient changes, for example due to defects in K^+Cl^- co-transporters (KCCs), GABAergic synapses can result in depolarization [32,33]. The glutamatergic activity also might not always result in increased excitation. Glutamatergic synapses innervate both excitatory and inhibitory neurons and, therefore, the net effect of these synaptic transmissions could become negligible or even inhibitory as the GABAergic neurons could reach their threshold for lower inputs and with faster dynamics (e.g., [34]).

1.2.3 Neuronal network

Excessive discharges are not necessarily epileptic; however, synchronization of network of neurons can lead to ictal activity which makes the study of synchronization in neural networks crucial for gaining a better understanding of ictal events [34]. There are different mechanisms that can lead to neural synchronization. The glutamatergic synapses make the pyramidal neurons highly

interconnected which could be one mechanism underlying synchronization. Another mechanism leading to synchronization could be gap junctions. Gap junctions are specialized channels that connect neighbouring cells and allow rapid cell-cell communication which can facilitate synchronization [35]. Due to their low number, formerly gap junctions were not deemed to be involved in neural synchronization; nonetheless, more recent studies have shown that even a few gap junctions could considerably modulate network dynamics [36]. The next mechanism promoting synchronization could be GABAergic activity [37,38]. GABAergic interneurons innervate numerous pyramidal cells and consequently, activity of a single inhibitory interneuron can synchronously hyperpolarize many excitatory cells. Hyperpolarization can deactivate some channels such as T-type calcium channels, which in turn, can lead to synchronous depolarization, caused by GABAergic inhibition [39]. Finally, synaptic reorganization and changes within the brain of patients with epilepsy, such as growth of axon collaterals, could result in synchronization with possible impact on the recurrent nature of seizures [40].

1.3 Electroencephalography and epilepsy

Electroencephalography, widely referred to as EEG, is the recording of the electrical signal arising from the synchronous action of neurons [41], and is one of the most useful tools for diagnosing epilepsy and identifying the seizure focus and areas of seizure propagation [42–44]. EEG, can be classified as invasive and non-invasive. Non-invasive EEG is measured using electrodes placed on the scalp surface while invasive EEG is obtained from intracranially implanted electrodes [45]. There are two types of invasive EEG recordings depending on method of implantation: stereoelectroencephalography (sEEG) and electrocorticography (ECoG). sEEG is measured using stereotactically inserted depth electrodes while ECoG recordings use subdural grid and/or strip electrodes placed directly on the neocortex after a craniotomy (depth electrodes may also be inserted but not stereotactically but using neuronavigation) (Fig.1-1). Since invasive electrodes are placed directly inside or on the surface of the brain, such recordings have enhanced amplitudes and better spatial resolution compared to non-invasive recordings which are attenuated and distorted due to skull impedance and the intervening tissue layers between the scalp and brain [46].

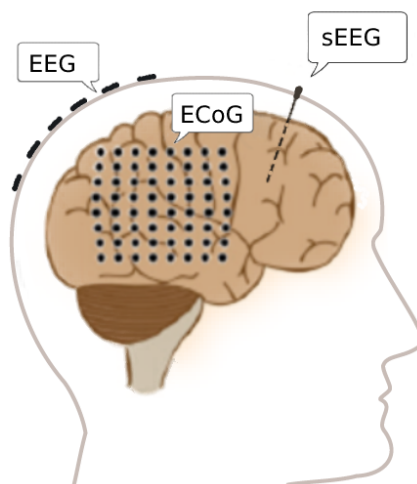


Figure 1-1 Invasive and non-invasive electroencephalography electrodes. Non-invasive EEG electrodes are placed on the scalp surface and invasive EEG is recorded from intracranially implanted electrodes either with stereotactically inserted depth electrodes (sEEG) or electrodes placed directly on the neocortex (ECoG).

For patients that are identified as drug-resistant epilepsy (DRE), invasive EEG recordings are carried out when surface EEG and other non-invasive localization techniques [e.g., magnetic resonance imaging (MRI), ictal single-photon emission computed tomography (SPECT), positron emission tomography (PET), and magnetoencephalography (MEG)] cannot reliably localize the epileptogenic zone to allow direct surgery [45].

1.4 Functional brain networks

Functional connectivity networks can be inferred from imaging techniques such as functional MRI (fMRI), MEG, EEG to evaluate the temporal statistical dependencies between time series of different regions in the brain [47]. Dynamic coordination between different brain regions gives rise to different brain functions and reflects the synchrony of neural oscillations [48–52]. When the oscillations between different regions are synchronized, information transmission between these regions is facilitated [53]; however, the brain constantly adjusts the flow of information by dynamically changing the synchrony between different neural ensembles [54–57]. Functional connectivity network analysis can estimate this inter-regional synchrony in electrophysiological data [58]. In these networks, nodes represent the recording sites and the edge between each pair of nodes could be any measure of coupling between the recordings from those nodes [58]. Functional

connectivity measures can be classified into two broad categories: non-directed and directed. Non-directed measures describe the interdependence between the time series without quantifying the direction of the interactions while directed measures estimate the direction of influence and causality between recordings [58].

1.5 Intracranial EEG seizure onset patterns

Studying the electrophysiological features of ictal intracranial EEG recordings has resulted in the definition of distinct seizure onset patterns [59,60] which are central in the understanding of ictogenesis and the transition from interictal to ictal activity [59–64]. For instance, the association between seizure onset patterns and the underlying pathological substrates [59,64,65] as well as the relevance of seizure onset patterns in predicting the outcome of the resection surgery have been widely investigated [66–68].

Based on the frequency, amplitude, and morphological features of these patterns, previous studies have described the following types of seizure onset patterns [59]:

- Low-voltage fast activity: rhythmic activity with frequency higher than 13Hz and amplitude lower than 10 μ V (Fig.1-2a);
- Low-frequency high-amplitude periodic spikes: high-voltage spiking with the frequency of 0.5-2 Hz (Fig.1-2b);
- Sharp activity: sharply contoured rhythmic activity with low to medium amplitude and frequency lower than 13 Hz (Fig.1-2c);
- Spike-and-wave activity: spike-and-wave with medium to high amplitude and frequency of 2–4 Hz (Fig.1-2d);
- Burst of high-amplitude polyspikes: a short burst of spikes with high amplitude (Fig.1-2e);
- Burst suppression: short bursts of spiking activity with medium to high amplitude and short periods of attenuation (Fig.1-2f);
- Delta brush: rhythmic delta activity with frequency of 1–2 Hz and superimposed high frequency activity with frequency of 20–30Hz (Fig.1-2g).

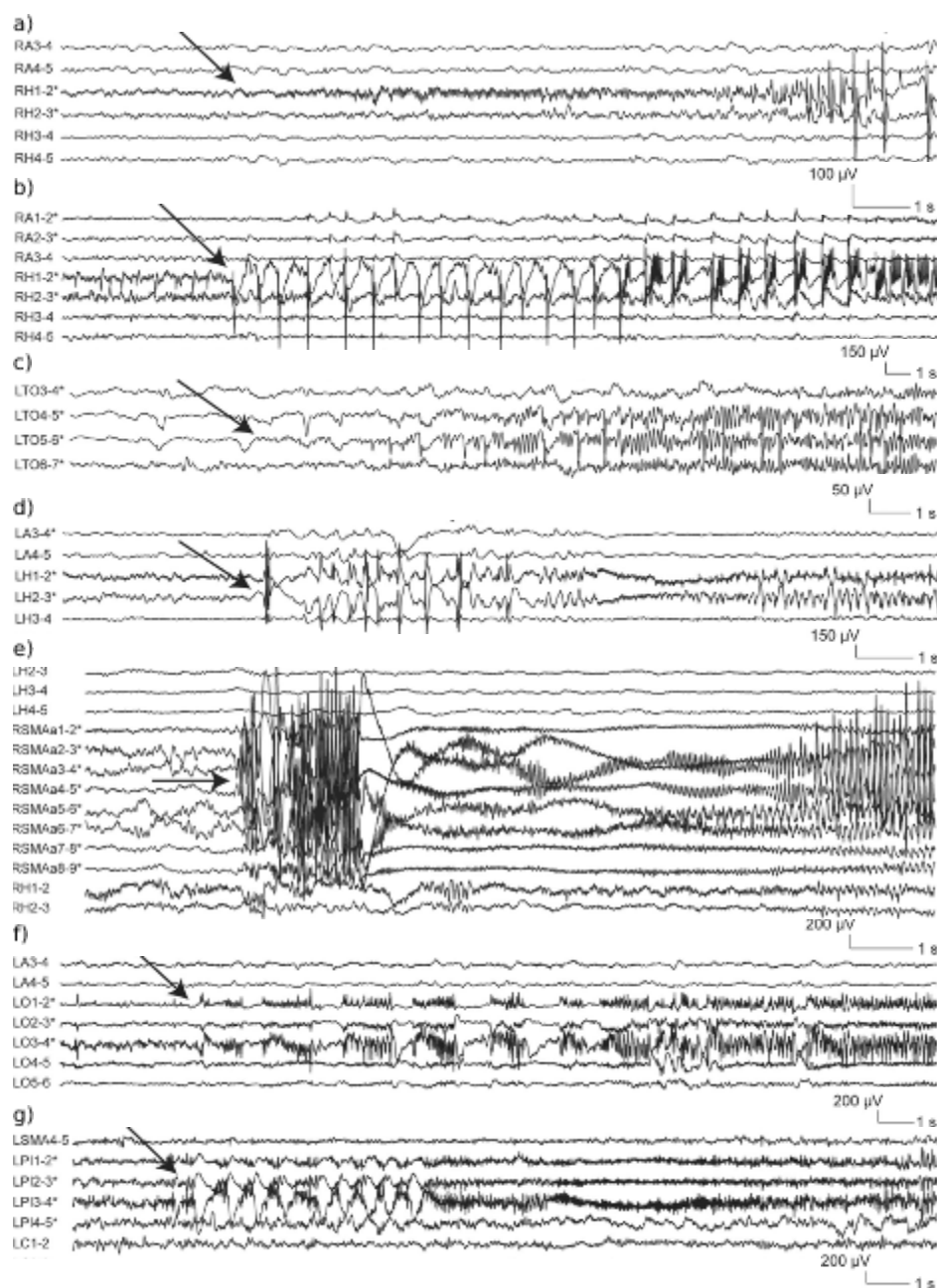


Figure 1-2 Intracranial EEG seizure onset patterns. a) Low-voltage fast activity recorded with electrodes located at right hippocampus, b) Low-frequency high-amplitude periodic spikes recorded with electrodes located at right hippocampus, c) Sharp activity recorded with electrodes located at left lingual gyrus, d) Spike-and-wave activity recorded with electrodes located at left hippocampus, e) Burst of high-amplitude polyspikes recorded with electrodes located at anterior aspect of right supplementary motor area, f) Burst suppression recorded with electrodes located at left orbitofrontal cortex, g) Delta brush recorded with electrodes located at left infero-parietal region (from Ref. [59]).

1.6 Computational models of ictal EEG

Computational models have been applied to explore the mechanisms that underly different ictal activities measured using EEG [69] such as the activities in different frequency bands as well as during different portions of the seizure (at onset, during propagation or upon termination) [70–72].

Electrophysiology and imaging studies have suggested various mechanisms for ictogenesis at different scales from single ion channel up to neural populations and whole brain networks [73,74].

Computational models are a powerful approach for integrating these various observations to obtain a comprehensive understanding of the mechanisms that give rise to EEG ictal recordings and formulating new hypotheses [75,76]. The model predictions can directly be validated and compared against experimental findings and EEG recordings [77]. In general, there are three dominant approaches in constructing mathematical models of ictal activity: biophysical network models, phenomenological models, and neural mass models.

1.6.1 Biophysical network models

Biophysically realistic network models of epilepsy are used to explore the influence of different molecular and synaptic characteristics of ictogenesis. However, these models are computationally expensive and rely on detailed cellular and synaptic mechanisms which could lead to highly parameterized and complicated models [78–82].

There are many insightful models of epilepsy within this computational modeling framework that investigate the effect of various neuronal network properties on the generation of ictal-like-events [76,83–89]. Some biophysically realistic models of epilepsy report the enhanced excitation responsible for seizure generation while some more recent models, by constructing a network model of excitatory and inhibitory neurons, have reported the emergence of seizure-like events caused by decreased excitation [84,90,91]. These findings agree with experimental observations reporting transition to ictal activity as a result of the application of AMPA receptor blocker [4]. While challenging the widely accepted concept of enhanced excitation to be pro-epileptic, the unexpected findings of these computational models offered new possible ictogenesis mechanisms to be further investigated.

Another example comes from the work of the Destexhe group who have developed a biophysical realistic model of the thalamocortical network aimed at studying absence seizures and reported a

critical role of the interplay between the thalamus and cortex in the generation of these seizures [80,92,93] which was validated experimentally by Bal et al. [94]. The generation of high frequency oscillations and their transition to ictal events have been intensively studied by Traub et al. [79,95–97]. By implementing a biophysically detailed network model, they found the electrical coupling between the axons of pyramidal cells through gap junctions to be responsible for the generation of fast oscillations [79,95–97].

1.6.2 Integrate and fire neural network

Integrate and fire models are one of the most widely used neuron models and, mathematically, they are based on a simpler framework compared to biophysical models [98,99]. Since action potentials of a neuron have the same shape, it is suggested that modeling the shape of action potentials cannot provide new information. Therefore, in integrate and fire modeling approach, without describing the shape of action potentials, their exact timing are predicted [100]. These models are comprised of two fundamental components: an equation that simulates the dynamic of the membrane potential and a mechanism that generates action potentials [98].

Integrate and fire models have been widely applied in modeling ictal activity [101,102]. In a study, Ursino et al., using a network of integrate and fire spiking neurons, have studied the impact of altering synaptic activities (i.e., excitation/inhibition balance) on the ictal EEG patterns [102]. By changing only a few parameters, their model could produce different patterns of activity characterized by different time domain and frequency domain features which qualitatively resembled the real ictal ECoG recordings [102]. In another study, using integrate and fire network of neurons with excitatory and inhibitory synapses, neural synchronization has been studied [103]. Their findings showed that when inhibition in their model is decreased, a pattern of desynchronized spikes could result in network synchronization [103]. Moreover, they showed that the application of a low amplitude stimulation could suppress the network synchronization [103]. Within the integrate and fire modeling framework, Hall et al. has investigated the velocity of the propagation of ictal activity [104]. Using two different parameter sets, their model could simulate the propagation speed of seizure like events from two different animal slice models: GABA antagonist model and the low extracellular $[Mg^{2+}]$ model [104].

1.6.3 Phenomenological models

Phenomenological models, in a simplified framework using the minimum number of parameters and without reference to physiological mechanisms, describe the dynamic of the system (i.e. the observed phenomenon) [105,106]. A well-known example of this approach in computational epilepsy is Epileptore [107]. It consists of one fast and one slow subsystem, each of which is further comprised of two state variables. The fast subsystem generates the fast activity whereas the slow one triggers sharp-wave-events (SWEs). In these models, there is another state variable which acts on a very slow time scale and simulates the transition from normal to ictal events. Within this framework, Epileptor can reproduce some of the ictal patterns observed in human and experimental models of epilepsy [107–109].

Because of their lower dimensionality, phenomenological models are generally viewed to be more tractable and computationally less expensive [107,110]. These models, despite being straightforward in their implementation, do not possess a physiological equivalent in their elements. Thus, findings are disconnected from physiological phenomena, resulting in limited interpretation when designing therapeutic measures.

1.6.4 Neural mass models

Neural mass models, takes a hybrid approach as they lie between biophysically realistic and phenomenological models and have the benefits of both approaches through incorporating the relevant biophysical features into a simple framework [111].

Because of the enormous complexity of the brain with millions of neurons and billions of synapses, modeling even a small region of the brain in full detail requires a large number of parameters, making it a rather difficult task. However, neural mass models without considering the biophysical details of different cells simulate the average activity of neural populations.

The simplest neural mass model is a coupled excitatory-inhibitory neural population. In the study of epilepsy, the neural mass model has been used to model the transition from interictal to ictal activity in mesial temporal lobe epilepsy (MTLE) and reported enhanced excitation underlying seizure generation [112–114]. These models have been further expanded to account for different types of inhibitory populations (i.e., dendrite targeting and soma targeting inhibitory interneurons) and to explore the effect of differently impairing these distinct inhibitory populations in ictogenesis

[112]. The findings of this modeling approach showed that the background activity converts into low voltage fast ictal activity when the dendrite targeting interneuron population is impaired [112].

The neural mass modeling approach has also been adopted to study absence seizures by considering four neural populations: pyramidal cells, interneurons, thalamocortical relay cells, and thalamic reticular nucleus cells. The results showed that the transition between interictal to absence seizures could occur in a bistable system, owing to variations in external inputs [115].

CHAPTER 2 LITERATURE REVIEW

2.1 Functional connectivity network in epilepsy

Functional connectivity analysis has been widely utilized to understand the complex networks of the brain with billions of neurons and connections [116–121] and expanded to the study of pathological states such as epilepsy [122,123].

Considering the spatial organization of the epileptic brain and the dynamic of ictal propagation, epilepsy is commonly described as a network disorder [124–131]. Characterizing the functional connectivity metrics of epileptic networks and the network organization of seizures has been vastly expanded in recent years [122,123,132–134]. As a few examples, these methods have been applied for understanding the dynamics of the epileptic brain network [135], localizing the seizure onset zone (SOZ) [136–141], and predicting the resective surgical outcome [142–146]. In an attempt to localize the SOZ, using connectivity analysis, higher connection weights within the SOZ [147] has been identified and it has been shown that the SOZ becomes isolated at seizure onset and more connected to other regions towards the end of the seizure [1]. Studies using functional connectivity analysis of the epileptic network have associated the resection of regions of high frequency activity with improved surgical outcome [139,148–154].

2.2 Dynamic of ictal state transition

Functional connectivity analysis has decidedly improved our understanding of the spatiotemporal interactions in epileptic networks and has identified different connectivity patterns during ictal activities. Yet, an interesting avenue for research in this regard would be the temporal dynamic of these ictal network reconfiguration and state transitions.

A large body of studies has investigated the dynamical evolution of synchrony in epileptic networks during interictal and ictal activities [125,155–158]. Previously, seizures were known as a hypersynchronous state of neural activity in the brain and this hypersynchrony was considered as the emergence of predominantly strong functional connections. But more recently, it has been suggested that at the level of large neuronal populations, seizures are not uniformly in hypersynchronous states. Higher synchrony at ictal onset and termination [159–164] and desynchronization during seizure propagation [165,166] have been reported. In their study on the

evolution of the epileptic network, Kramer et al. [164] have reported the emergence of a large subnetwork close to seizure onset and termination and higher network fragmentations in between. In the same study, they also reported that, despite noticeable changes in the dynamic of the recordings during seizures, the measure of density did not change and accordingly postulated that the ictal networks reorganize rather than reducing or increasing their edges [164].

Concerning the connection strength in epileptic networks, it has been suggested that a dynamical change among strong and weak connections is present in the course of a seizure [160,164,167,168]. Some studies have attempted to explore the dynamics of these changes by considering node centrality and changes in functional connectivity measures [1,2,169]. A study by Khambhati et al. [2] found more weak connections in the pre-ictal period and more strong connections during ictal activity. They hypothesized that their findings on the weak connectivity prior to seizure initiation is a mechanism through which the system becomes more flexible to drive rapid ictal activities. They also reported the shortening of stronger connections along with the seizure generation and towards its termination and interpreted this observation as a potential control mechanism to suppress the disruptive activity of the epileptiform network [2].

These studies collectively point towards network reconfigurations during ictal activities. Methods which are capable of exploring the dynamics of functional connectivity in the brain can help us to study the state transitions in epileptic network. Burns et al. [1] have demonstrated that the epileptic network goes through recurring state transitions. They suggested that, despite the highly complex brain activity, there is a less complex, low-dimensional space of brain dynamic. On the contrary, Khambhati et al. [2] reported rapid reorganization in network geometry during pre-ictal period and slower geometric changes during ictal activity while Liu et al. [3] found no significant differences among the ictal, pre-ictal, and post-ictal state transition rates. These discrepant observations necessitate the reconsideration of the dynamic of state transitions during seizures.

2.3 Interictal to ictal transition: seizure generation

2.3.1 Seizure generation and impaired excitation-inhibition balance

To gain a mechanistic understanding of epilepsy and its underlying mechanisms, studying the transition from interictal into ictal activity (i.e., seizure generation) is of great importance [30]. The primary focus of a large body of research on seizure generation has been the imbalance between

synaptic excitation and inhibition [34,71,170–177]. The overall abnormally enhanced glutamatergic excitation and decreased GABAergic inhibition have been widely believed to be pro-epileptic and the main driver for seizure generation, while the enhanced GABAergic inhibition was viewed as anti-epileptic [4–7]. Contrary to these views, the synchronized activity of inhibitory neurons has been found critical for the hyperexcitability of pyramidal cells and seizure onset [178,179] which could be caused by their abundant and strong connections to multiple postsynaptic neurons [180,181]. More recent studies have not only found the GABAergic inhibitory activity preserved and functional before seizure onset in the 4-aminopyrimidine (4-AP) animal model of epilepsy [182] but also have reported enhanced inhibition before and at the very onset of seizures [8–14,112,183,184]. The *in vitro* study of postsurgical human tissue has also revealed that inhibition is retained, and ictal activity could rely on GABAergic inhibition [33,185,186]. These recent findings have challenged the widely held belief on the role of GABAergic network in ictogenesis. The first report on the involvement of inhibitory activity in the initiation of seizure-like-events came from the Avoli group in a 4-AP rat model of epilepsy [187,188] which was further corroborated by other studies [189–194].

Trevelyan et al. [4,195] have suggested that the enhanced inhibitory activity prior to the seizure initiation was a mechanism preventing the generation of ictal events by shutting off the excitatory neurons; they further proposed that failure of such a mechanism results in seizure generation. This rationale has also received support from another study by Cammarota et al. [7]. Using a brain slice model, they reported the role of inhibitory activity in restraining seizure propagation and found the failure of the inhibitory network caused by depolarization block responsible for the propagation of ictal discharges [7]. Seizure initiation due to depolarization block of inhibitory activity has been observed in other *in vitro* studies as well [196–198]; however, this interpretation has never been validated *in vivo*.

In summary, the role of excitatory-inhibitory balance in the generation of ictal-like-events is open to discussion. While many studies are reporting the loss of inhibitory interneurons both in human and animal models of epilepsy [199,200], mounting studies are pointing towards the enhanced activity of the inhibitory network in generating seizures. As proposed by Williams et al. [201], it should also be considered that the alterations in the GABAergic network could be either pro-epileptic or anti-epileptic depending on the brain area and the inhibitory pathways.

2.3.2 Ictal patterns and impaired E-I balance

Seizure onset patterns are central in the understanding of ictogenesis [61,63,64]; however, whether different underlying mechanisms give rise to distinct seizure onset patterns is yet to be fully understood.

A few onset patterns such as low voltage fast activity (LVFA) and hypersynchronous onset patterns have been associated with specific synaptic mechanisms [175,202]. Both LVFA and hypersynchronous patterns have been found in experimental models of epilepsy [203–208]. In a study using the *in vitro* 4-AP rodent model and optogenetic control of GABAergic interneurons, Shiri et al. [202] have reported the involvement of these cells in the generation of LVFA seizure onset pattern which has been validated *in vivo* as well [14]. In another *in vitro* study, the enhanced activity of inhibitory interneurons in the entorhinal cortex of the guinea pig model of epilepsy was found to temporarily mute the activity of principal cells and initiate LVFA seizure onset pattern [209].

On the other hand, the hypersynchronous seizure onset pattern has been reported to emerge due to overall enhanced excitatory activity [175,202]. Using brain slices in low magnesium and high potassium perfusate, the simultaneous enhancement of excitation and inhibition has been reported during the preictal period; however, when the GABAergic inhibition became exhausted, a seizure of the hypersynchronous onset pattern type was initiated, suggesting an association between the generation of this seizure onset pattern and enhanced cortical excitability [196,206,210]. In conclusion, depending on the pattern observed at the onset of a seizure, different paradigms of excitatory-inhibitory imbalance could be in charge.

2.3.3 Models of spatiotemporal patterns of seizure onset

There are many computational models that have reproduced the real ictal EEG recordings [75,211–213]. A phenomenological model developed by Jirsa et al. could simulate the synchronized EEG activity patterns; however, using this modeling approach addressing the responsible neurophysiological processes is not straightforward [107,214]. In another attempt, by constructing a phenomenological network model of seizure onset, Creaser et al. have investigated the role of the intrinsic node properties and node coupling weights in driving different spatiotemporal patterns of seizure onset [215].

To explore specific neurophysiological processes and their roles in seizure generation, biophysical models have been used. For instance, intracellular and extracellular potassium [84,216] as well as transmembrane chloride dynamics [217], and calcium-dependent activities [218] have been investigated in biophysical modeling framework. Using a biophysically inspired model, Liou et al. could simulate EEG and multiunit array recordings from patients with epilepsy [71]. Their findings highlighted the role of inhibition exhaustion and synaptic plasticity in the generation of ictal events [71]. To explore the transition from interictal to different ictal activities, Saggio et al. considered the abrupt transitions at seizure onset as bifurcations in a dynamical system and defined a taxonomy of seizure dynamics [219].

Wang et al. simulated a cortical sheet by coupling 150 by 150 minicolumns which were modeled using Wilson-Cowan neural mass model [220] and generated two different onset patterns of focal seizures which qualitatively resembled the real ictal recordings: the low amplitude fast and high amplitude slow onset patterns [221]. Their results showed that the surround excitability level plays a critical role in the generation of seizure onset patterns and they proposed that in devising the therapeutic measures the type of seizure onset pattern should be considered [220]. More specifically, their model suggested that seizure freedom for patients with high amplitude seizure onset patterns could be achieved by controlling the excitability level of the surround while patients with low amplitude fast seizure onset patterns could benefit from resective surgery [220]. In their model, Wang et al. did not consider different high amplitude onset patterns as suggested in clinical studies such as spike and wave, high amplitude spikes and sharp waves [222,223]. Despite the large body of research on modeling seizure generation [224], a complete understanding of the basic biophysical processes that lead to seizures with different onset patterns is largely missing.

2.4 Research overview

The overarching theme of this thesis is to improve our understanding of epilepsy by studying the dynamic reconfiguration of epileptic networks as well as the mechanisms generating ictal events.

To explore the dynamic reconfiguration of epileptic networks, some previous studies have identified recurrent states and investigated the transition of these states which have generated conflicting results and encouraged us to reconsider ictal state transitions (*chapter 4*).

The transition from interictal into ictal activities (i.e., seizure generation) has been widely explored and different activity patterns at the onset of seizures have been described. Studying seizure termination patterns, however, have been largely overlooked [225,226] and the associations between seizure onset and termination patterns remains unexplored. Knowing the associations between seizure onset and termination patterns could aid us developping alternate therapeutic approaches to control seizures. Concerning seizure onset patterns, another topic that has been largely untouched is whether seizures with distinct onset patterns are preceded by varying network interactions. One possible way to address this question is via studying the functional connectivity networks prior to the generation of seizures of distinct onset patterns which is explored in *chapter 5*.

Seizure generation involves the interaction of many complex cellular and synaptic components [227,228]. Experimental studies have reported different and sometimes contrary mechanisms for the generation of ictal activities [4–13]. A modeling approach that considers all these different mechanisms using a unified framework could aid us in understanding seizure generation and further help us investigate and articulate whether different underlying mechanisms could lead to seizures with different onset patterns. By constructing a neural mass model in *chapter 6*, we aimed at providing insights on whether different physiological mechanisms underly different seizure onset patterns?

Our **aims** and **hypothesis** in this thesis can be summarized as follows:

AIM 1: To investigate the epileptic network dynamics and ictal state transition.

We **hypothesized** that the epileptic brain, as a dynamical system, constantly modulates its state, and that the patterns of these recurrent states can be identified by exploring the dynamic of functional connectivity networks.

Article 1: Shokooh, L. A., Toffa, D. H., Pouliot, P., Lesage, F., & Nguyen, D. K. (2020). Identification of global and local states during seizures using quantitative functional connectivity and recurrence plot analysis. *Computers in biology and medicine*, 122, 103858.

AIM 2: To identify different seizure onset and termination patterns and their associations as well as pinpoint the driver region for different seizure onset patterns.

We **hypothesized** that 1) there is an association between different seizure onset and termination patterns and 2) the network interactions are different before the generation of seizures of distinct onset patterns.

Article 2: Shokooh, L. A., Toffa, D. H., Pouliot, P., Lesage, F., & Nguyen, D. K. (2021). Intracranial EEG seizure onset and termination patterns and their association. *Epilepsy Research*, 176, 106739.

AIM 3: To explore whether different mechanisms underly the generation of seizures of distinct onset patterns at the neural population scale using a computational modeling approach.

We **hypothesize** that seizures with distinct onset patterns arise from different underlying mechanisms which can be identified by implementing a computational model that includes some of the most relevant biophysical features.

Article 3: Shokooh, L. A., Lesage, F., & Nguyen, D. K. (2021). Computational modeling of seizure onset patterns to underpin their underlying mechanisms. *Journal of Neural Engineering*, in revision.

Conference abstracts:

Shokooh, L. A., Toffa, D. H., Pouliot, P., Lesage, F., & Nguyen, D. K. (2020). How brain global and local states change during seizures? North American Virtual Epilepsy Meeting, 24-27 September 2020.

Shokooh, L. A., Toffa, D. H., Pouliot, P., Lesage, F., & Nguyen, D. K. (2020). Epileptic network as a pathological state with disturbed relaxation and increased network noise, American Epilepsy Society Annual Meeting, 4-8 December 2020.

Shokooh, L. A., Toffa, D. H., Pouliot, P., Lesage, F., & Nguyen, D. K. (2021). Rethinking the seizure generation and termination mechanisms underlying diverse onset and offset ictal patterns: A computational approach, American Clinical Neurophysiology Society Annual Meeting, 10-14 February 2021.

Shokooh, L. A., Toffa, D. H., Pouliot, P., Lesage, F., & Nguyen, D. K. (2021). Identifying different seizure onset and termination patterns and detecting the driver region preceding different onset patterns, 34th International Epilepsy Congress, 28 August - 1 September 2021.

CHAPTER 3 THEORY AND METHODOLOGY

3.1 Functional connectivity measures

To construct the functional connectivity networks and quantify the linear, nonlinear or causal interactions in these networks, we first need to determine the coupling measure [229]. Different measures could quantify the network interactions from different perspectives and with different assumptions. For instance, for some measures, we need to filter the data in specific frequency bands and for some others, we may need the embedding dimensions to construct the phase space. There is a substantial number of connectivity analysis methods, ranging from linear methods (such as cross-correlation in the time domain or coherence in the frequency domain) to nonlinear methods (such as mutual information and nonlinear regression analysis) [58,230,231]. Recent studies, however, have argued that the linear and nonlinear connectivity measures have comparable performance in capturing the relationships in macroscopic datasets [231]. The rest of this section provides a brief description of the functional connectivity measures we applied in this thesis.

3.1.1 Cross-correlation

Cross-correlation is one of the simplest non-directed functional connectivity measures which calculates the linear relationship between two time series in the time domain as presented in Eq.3-1.

$$\rho_{x,y}(m) = |E[(x(t) - \mu_x)(y(t) - \mu_y)]| \quad (3-1)$$

Where, $\rho_{x,y}(m)$ is the normalized cross-correlation between the two time series x and y and μ_x and μ_y are the average of the two recordings.

3.1.2 Coherence

Coherence is a normalized measure ranging between 0 and 1 that quantifies phase synchrony and could be interpreted as the frequency domain equivalence of cross-correlation. In a pair of time series, coherence, as a function of frequency can quantify the amount of variance in one time series that can be explained by the other one and can be calculated based on Eq.3-2.

$$coh_{xy}(\omega) = \frac{|S_{xy}(\omega)|^2}{S_{xx}(\omega).S_{yy}(\omega)} \quad (3-2)$$

here, $S_{xy}(\omega)$ represents the cross-spectrum density between time series x and y at frequency ω while $S_{x,x}(\omega)$ and $S_{y,y}(\omega)$ shows the autospectrum densities of the time series x and y.

3.1.3 Phase locking value

Phase Locking Value (PLV) is one of the most common measures to calculate phase interactions between two signals. It is calculated based on Eq.3-3 as a complex vector with unit-length representing the mean phase difference between two time series [232,233]. When the signals are independent PLV equals zero while for two strongly coupled signals PLV approach one.

$$\lambda_{x,y}(m) = \frac{1}{N} \left| \sum_{t=1}^N e^{j|\varphi_x(t) - \varphi_y(t)|} \right|, \quad (3-3)$$

here, $\lambda_{x,y}(m)$ is the PLV between time series x and y and $\varphi_x(t)$ and $\varphi_y(t)$ represent their instantaneous phases calculated using Hilbert transform and N is the total number of samples. PLV is suggested to be a better estimation of the phase synchrony compared to coherence because in calculating coherence the phase differences are weighted by the amplitude correlations.

3.1.4 Recurrence Plot, Recurrence Quantification Analysis, and Joint Recurrence Plot

Recurrence Plot (RP) first introduced by Ekmann et al. [234] is a graphical representation of the dynamical characteristics of a signal which has been successfully applied to nonstationary and short time series where other methods may fail [6–9]. Recurrence Quantification Analysis (RQA) as introduced by Zbilut et al. [235,236], quantifies the structures and information of the RPs, and Joint Recurrence Plot (JRP) is a bivariate version of RP. For creating RPs and JRPs from time series and performing RQA, we first need to construct the phase space as it is described in the next section.

3.1.4.1 Phase space reconstruction

A phase space is a representation of all states of a dynamical system. Each point in phase space shows one possible state of the system. To reconstruct the phase space, we applied Takens' theorem [237]. In this method, the trajectories in the d-dimensional phase space are constructed using delayed versions of the original time series. The time delays and the embedding dimension are

calculated respectively using “*minimum mutual information*” and “*false nearest neighbor*” algorithms [238,239].

Mutual information between two signals measures their dependence and therefore, using the minimum mutual information of $x(t)$ and $x(t + \tau)$, we can obtain the time delay τ for which $x(t)$ and $x(t + \tau)$ have the least dependence and can be calculated based on the framework introduced in [238].

To reconstruct the phase space, after estimating the time delay, we need to calculate the embedding dimension and the time delay vectors (Eq.3-4).

$$y = (x_i, x_{i+m_0}, \dots, x_{i+m_0(d-1)}), \quad (3-4)$$

where d represents the embedding dimension and x_i is the i^{th} element of the time series x . For true dimension d , the data points that are in close vicinity to each other, remain neighbors in dimension $d + 1$ and are called true neighbors otherwise false neighbors [239]. The false nearest neighbor algorithm by starting from a low value for dimension finds the embedding dimension as the dimensionality for which the number of false neighbors equals zero [240].

3.1.4.2 RPs and RQA

RPs visualize the dynamics of phase space trajectories. Considering $x_i, i = 1, \dots, N$ (N = the total number of samples), to be the i^{th} element of the phase space trajectory, a dot at location (i, j) on the two-dimensional $N \times N$ square matrix RP shows that the distance between the points i and j is less than a threshold parameter r (Eq.3-5). The parameter r was chosen equal to 10% of the maximum phase space diameter [235,241].

$$R_{i,j}(x(t)) = \begin{cases} 1, & \text{if } d(x(i), x(j)) < r, \\ 0, & \text{otherwise,} \end{cases} \quad (3-5)$$

here, $d(x(i), x(j))$ represents the distance between the i^{th} and j^{th} points of the trajectory.

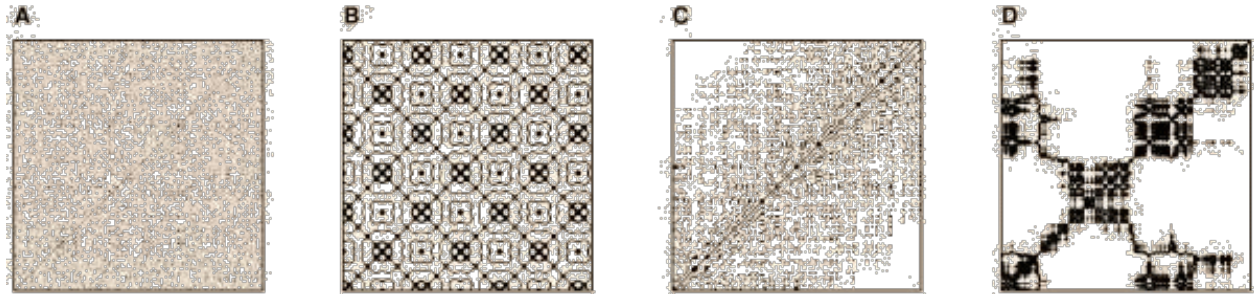


Figure 3-1 Recurrence plots of different time series. (A) homogeneous pattern representing uniformly distributed noise, (B) the checkboard pattern representing a periodic time series, (C) the pattern for a time series with drift and (D) disrupted patterns for Brownian motion noise [from Ref. [242]].

The structures on the RP describe the temporal evolution and the dynamical characteristics of the phase space trajectories. Fig.3-1 represents these plots for four different signals with distinct dynamics. The homogeneous RP in Fig.3-1a is from a random time series while the diagonal lines and the checkboard structure of the RP in Fig.3-1b represent a system with a periodic dynamic. A system with a slowly changing variable and a drift in its dynamic results in a RP with bright corners as depicted in Fig.3-1c. The RP in Fig.3-1d with white regions is from a system with abrupt changes.

Apart from these large-scale patterns, the small-scale texture of these plots can also describe the dynamical characteristics of the underlying system. Single isolated dots mean that the states do not persist while diagonal structures emerge on the RPs when the same state is revisited at different times. The length of the vertical structures on these plots displays the time length that a unique state persists and does not change. These diagonal and vertical small-scale structures represent the system dynamics [241,243,244] and could be quantified using RQA by *Determinism (DET)* and *Laminarity (LAM)* [245,246] which respectively compute the ratio of the points forming diagonal and vertical lines.

3.1.4.3 JRPs

The JRP as the bivariate version of RP can be calculated as presented in Eq.3-6.

$$JR_{i,j}(x(t), y(t)) = R_{i,j}(x(t)) \cdot R_{i,j}(y(t)) \quad (3-6)$$

here, $JR_{i,j}$ represents the JRP between the time series x and y and $R_{i,j}$ is the recurrence plot as defined in Eq.3-5. There is a dot on the location (i,j) of the JRP when the $R_{i,j}$ for both time series equals 1 which points to the simultaneous recurrence of x and y .

3.1.5 Phase slope index

The phase Slope Index (PSI) measures the directionality of information flow between two signals by estimating the slope of the phase difference between the driver and recipient versus the frequency [247]. Different waves travel with the same speed and consequently, the phase difference between the driver and receiver increases with the frequency which leads to a positive slope of the phase spectrum. As an example, Fig.3-2 shows the application of this measure. In this figure, based on the phase difference between the red and blue signals (ϕ_{r-b}) in a specific frequency (either 20Hz, 25Hz, or 33.33Hz), it is not possible to determine the driver and recipient; however, this ambiguity could be resolved by looking across frequencies which could be observed in the graph depicting the phase difference versus the frequency in Fig.3-2b. In this figure, the linear relationship between phase differences and the corresponding frequencies, would imply a constant time shift and accordingly specify the red signal the driver and the blue one the recipient.

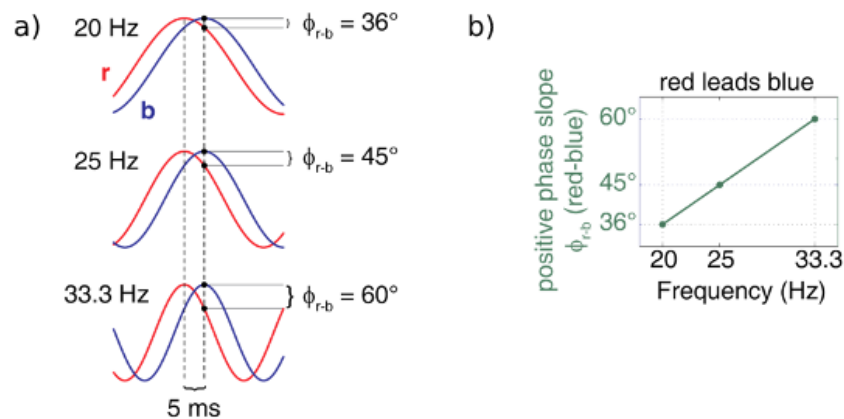


Figure 3-2 Phase slope index (PSI). a) phase differences between two signals in blue and red for three different frequencies b) The linear relationship between the phase differences versus frequencies for the signals presented in (a) (from Ref. [247]).

As presented in Eq.3-7, PSI is calculated from the complex coherency and the sign of PSI determines which signal is the driver.

$$\hat{\psi}_{ij} = \Im(\sum_{f \in F} C_{ij}^*(f) C_{ij}(f + \delta f)), \quad (3-7)$$

here, $C_{ij}(f) = S_{ij}(f) / \sqrt{S_{ii}(f) S_{jj}(f)}$ represents the complex coherency and S is the cross-spectral matrix. δf is the frequency resolution and $\Im(\cdot)$ keeps the imaginary part and f shows the range of frequencies.

3.2 Jansen model: Neural mass model of cortical columns

3.2.1 Cortical columns

The cerebral cortex is the largest part of grey matter in the brain with two to four millimeters thickness covers the surface of the cerebral hemispheres and is folded into ridges (called gyri) and depressions (called sulci). The neocortex forms 90% of the cerebral cortex and is described as a uniform structure consisting of six horizontally organized layers named layer I (at the surface) to VI (next to the white matter) which are characterized by their cell types and neuronal connections (Fig.3-3). Neurons in the cortex could be classified into two broad categories: projection neurons and interneurons. Projection neurons are excitatory cells, mainly pyramidal cells, forming about 80% of cortical neurons and existing in all cortical layers except cortical layer I. Interneurons, on the other hand, are mainly inhibitory neurons and makeup about 20% of cortical neurons and could be located in all layers [248]. Many neurons in the neocortex extend their axons and dendrites from superficial cortical layers to the white matter and form a columnar structure in the cortex called cortical columns. Cortical columns are vertical structures extended across all six layers with about 0.5 mm diameter and 2 mm length. They are considered as functional units of the neocortex; however, their cell organization and thickness are not uniform across the cerebral cortex, and consequently, they are divided into regions with homogenous features and specific functions (e.g., visual, auditory, and motor cortex) [248,249].

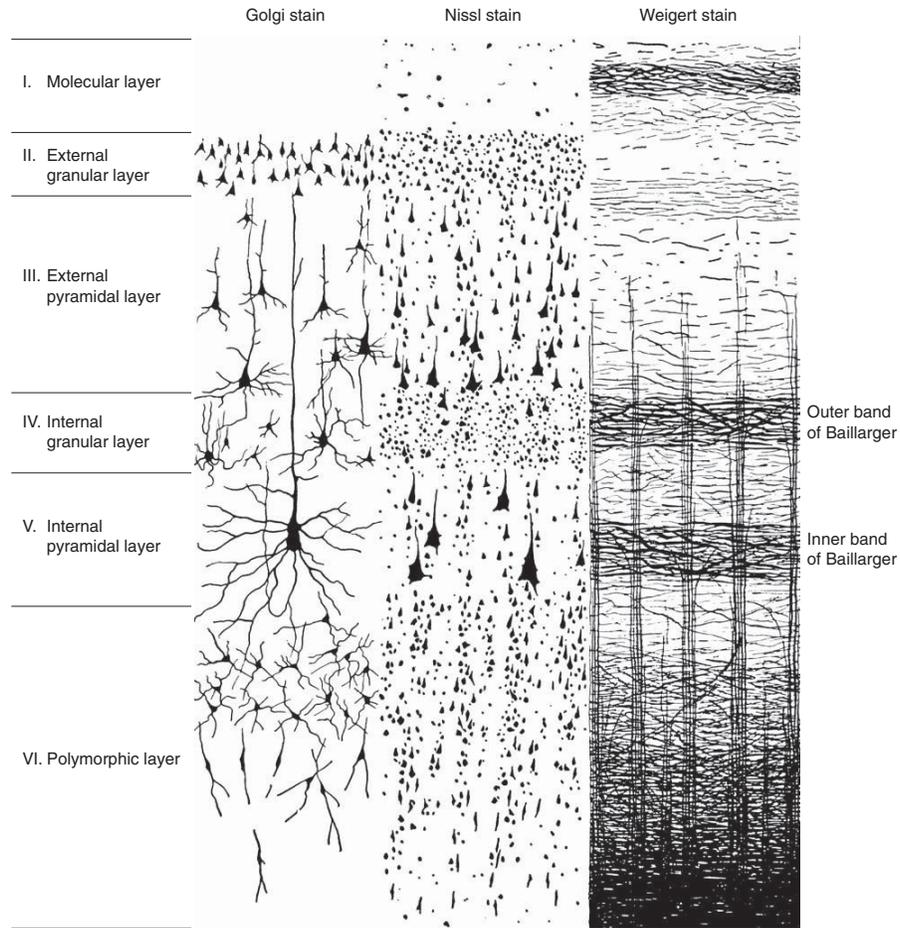


Figure 3-3 Six cortical layers represented by three different staining techniques (from Ref. [250]).

3.2.2 Jansen's model of cortical columns

Jansen et al [251] developed a method to simulate EEG recordings of visual evoked potentials by modeling cortical columns as an interconnected population of excitatory and inhibitory neurons. Their computational approach was an extension of a model originally constructed by Lopes Da Silva et al. and Van Rotterdam et al. [252,253] to reproduce EEG recordings of the brain's rhythmic activities.

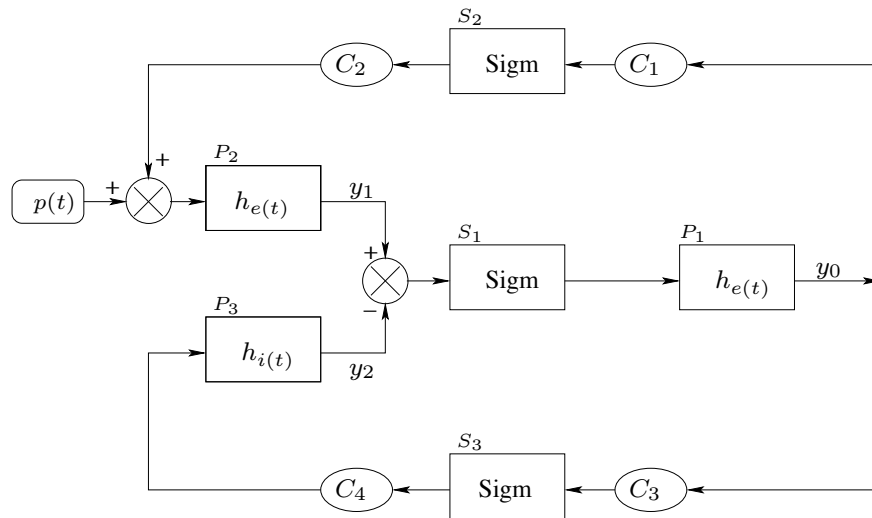


Figure 3-4 A representation of the computational model of a single cortical column. The average pulse density of the presynaptic neurons is transformed to average postsynaptic membrane potential by $h_e(t)$, $h_i(t)$ blocks. The Sigm blocks represent the static nonlinear sigmoid function converting the input potential of each population to average output pulse density (from Ref. [251]).

Jansen's model is comprised of three neural populations: pyramidal neurons, excitatory interneurons, and inhibitory interneurons. In their model, the pyramidal population receives excitatory and inhibitory projections from interneurons located within their column as well as excitatory inputs from other columns and subcortical regions. Fig.3-4 represents the structural configuration of this model for one column in which $P(t)$ models noise and input from other regions. In this figure, each modeled neural population is represented by two blocks. The first block converts the average presynaptic firing rate of action potentials into average postsynaptic membrane potential which can be either excitatory or inhibitory respectively with impulse responses $h_e(t)$ and $h_i(t)$ as in Eq.3-8 and Eq.3-9.

$$h_e(t) = \begin{cases} Aate^{-at} & t \geq 0 \\ 0 & t < 0 \end{cases}, \quad (3-8)$$

$$h_i(t) = \begin{cases} Bbte^{-bt} & t \geq 0 \\ 0 & t < 0 \end{cases}, \quad (3-9)$$

Where A and B respectively are the excitatory and inhibitory synaptic gains and a and b stand for synaptic transmission delays. These blocks are equivalent to solving the differential equation in Eq.3-10.

$$\ddot{y}(t) = Wgx(t) - 2g\dot{y}(t) - g^2y(t), \quad (3-10)$$

where the parameters $W = A$, $g = a$ for excitatory populations and $W = B$, $g = b$ for inhibitory populations. The second-order differential equation in Eq.3-10 can be rewritten as:

$$\begin{cases} \dot{y}(t) = z(t) \\ \dot{z}(t) = Wgx(t) - 2gz(t) - g^2y(t) \end{cases} \quad (3-11)$$

where, $x(t)$ and $z(t)$ respectively represent the input and output of the block.

The second block is a nonlinear component in the form of a sigmoid function which transforms the average postsynaptic potential into the average firing rate (Eq.3-12).

$$Sigm(v) = \frac{2e_0}{1+e^{r(v_0-v)}}, \quad (3-12)$$

here, e_0 represents the maximum firing rate, r is the slope of the sigmoid and v_0 the half activation potential.

Using Eq.3-11 and Eq.3-12, the model could be written as:

$$\begin{cases} \dot{y}_0(t) = y_3(t) \\ \dot{y}_3(t) = AaSigm[y_1(t) - y_2(t)] - 2ay_3(t) - a^2y_0(t) \\ \dot{y}_1(t) = y_4(t) \\ \dot{y}_4(t) = Aa\{P(t) + C_2Sigm[C_1y_0(t)]\} - 2ay_4(t) - a^2y_1(t) \\ \dot{y}_2(t) = y_5(t) \\ \dot{y}_5(t) = Bb\{C_4Sigm[C_3y_0(t)]\} - 2by_5(t) - b^2y_2(t) \end{cases} \quad (3-13)$$

here, y_0 , y_1 and y_2 are the blocks outputs and C_1 through C_4 represent the connectivity constants which shows the total number of synapses between the neural populations.

In the following chapters, by using the methodology introduced here, we will address the research questions presented in Chapter 2.

CHAPTER 4 ARTICLE 1: IDENTIFICATION OF GLOBAL AND LOCAL STATES DURING SEIZURES USING QUANTITATIVE FUNCTIONAL CONNECTIVITY AND RECURRENCE PLOT ANALYSIS

Leila Abrishami Shokooh^{a,b,*}, Dènahin Hinnoutondji Toffa^c, Philippe Pouliot^{a,d}, Frédéric Lesage^{a,d†}, Dang Khoa Nguyen^{c†}

^a École Polytechnique de Montréal, Université de Montréal, C.P. 6079, succ. Centre-Ville, Montreal, H3C 3A7, Canada

^b Centre de Recherche du Centre Hospitalier de l'Université de Montreal (CHUM), Montreal, QC, Canada

^c Neurology Division, Centre Hospitalier de l'Université de Montréal (CHUM), 1000 Saint-Denis, Montreal, H2X 0C1, Canada

^d Research Centre, Montreal Heart Institute, Montreal, Canada

* Correspondence to Leila Abrishami Shokooh, École Polytechnique, Université de Montréal, C.P. 6079 succ. Centre-Ville, Montreal, H3C 3A7; e-mail : Leila.abrishami-shokooh@polymtl.ca

† Equally contributing PIs

This article has been published in the journal of Computers in biology and medicine, June 2020.

Abstract

Introduction: As a dynamical system, the brain constantly modulates its state and epileptic seizures have been hypothesized to be low dimensional periodic states of the brain. With this assumption, seizures have previously been investigated to identify patterns of these recurrent states; however, these attempts have generated conflicting results. These discrepant observations led us to reconsider the dynamic of state transitions during seizures.

Methods: Using intracerebral recordings of 17 refractory epilepsy patients assessed prior to surgery, we studied ictal states with several state-of-the-art methods in order to investigate their dynamics. Global states were identified based on distinct functional connectivity measures in the time domain, frequency domain, and phase-space. We further investigated the state transitions in different brain regions locally using a univariate measure based on dynamical system analysis named the Recurrence Plot (RP).

Results: For the ictal period, we detected lower global state transition rates compared to pre- and post-ictal periods ($p < 0.05$ for seizure-free (SF) and $p > 0.05$ for non-seizure-free (NSF) groups post-surgery); however, the structure of RPs pointed towards higher state transition rates in some regions like the seizure-onset-zone ($p < 0.001$ for SF and $p > 0.05$ for NSF group). Moreover, a direct comparison of state transition dynamics between SF and NSF patients revealed different patterns for local state transitions between SF and NSF patients ($p < 0.05$ for seizure-onset-zone

while $p > 0.05$ for other regions) and no significant difference in global state transition rates ($p > 0.05$).

Conclusion: Our findings pointed to distinct dynamics for state transitions at different spatial scales. While the pattern of global state transitions led to the conclusion that the brain changes state less frequently during ictal activity, locally, it experienced a higher rate of state transition. Furthermore, our results for different patterns of state transitions in the seizure-onset-zone between SF and NSF patients could have a practical application in predicting surgical outcome.

4.1 Introduction

Seizures have previously been thought of as a hypersynchronous state of neural activity in the brain and such hypersynchrony is explained by the emergence of strong functional connections in the epileptic network. However, it has recently been suggested that large neuronal populations within the epileptic focus are not uniformly hypersynchronous during seizures and the epileptic network undergoes state transitions [107,124].

Investigations of state transitions using graph theory analyses of seizures recorded using intracerebral EEG electrodes have provided conflicting findings [1–3]. In these studies, each electrode contact was considered as a node in a graph, while edges between pairs of nodes were coded through a measure of the similarity between node recordings in the time or frequency domain. Brain connectivity was then assessed from the temporal evolution of the reconstructed network. Within this framework, Burns et al. [1] have reported highly varying connectivity during seizures and relatively stable connectivity in pre-ictal and post-ictal periods. Although they did not directly address the dynamics of state transition rates, a high ictal state transition rate was expected based on the high number of identified states in ictal epochs compared to pre- and post-ictal epochs. Conversely, Khambhati et al. [2] found rapid changes in network geometry in pre-seizure epochs and slower geometric changes during ictal activity (the post-ictal period was not studied) while Liu et al. [3] reported no significant differences among the ictal, pre-ictal and post-ictal state transition rates.

These conflicting findings could be due to differences in methodology, datasets, or the validity of the underlying assumption about the existence of recurrent states. Specifically, their methodology differed both on the applied functional connectivity measures and their choice of clustering

algorithm which makes addressing the source of inconsistent findings difficult. Furthermore, in all those studies, the different states were identified based on the overall pattern of functional connectivity; thus, global states were studied rather than local state transitions in different regions. Investigating local state transitions could improve not only our understanding of the dynamic of seizures but could eventually work towards novel therapeutic solutions such as modulation of seizures through the local electrical stimulation of a specific region.

To address these issues, we first explored global state transitions on a set of intracranially-recorded seizures using different approaches. To facilitate the comparison among different approaches employed in this study, we restricted the variation among them to their choice of functional connectivity measures, while the adopted clustering algorithm remained the same. However, the optimal parameters utilized within the clustering algorithm were optimized separately for each approach. To allow comparison with results from past studies, we also implemented the functional connectivity measures proposed by Refs. [1–3] and calculated the *global state* transition rates on the same dataset. Moreover, with the application of a univariate measure based on phase space reconstruction of each channel, we investigated *local states* in different regions throughout the course of seizures. To this end, for each channel recording in phase-space, Recurrence Plots (RPs) were constructed. RPs can be used to quantify the complexity of the network and order in the data based on the features of the phase space trajectories of the system [241]. By quantifying relevant features from these plots, we further studied the dynamic of local states.

4.2 Methodology

4.2.1 Patient population and intracranial EEG recordings

Intracranial EEG recordings of seizures used for analyses were obtained from 17 epileptic patients being investigated for potential epilepsy surgery; 11 patients seizure free (SF) after surgery (Engel I outcome) and 6 non-seizure-free (NSF) patients (Engel II), at the Centre Hospitalier de l'Université de Montréal (CHUM). Recordings were collected at a sampling rate of 2 kHz over a period of ~2 weeks using a 128-channel EEG monitoring system (Stellate Harmonie System, Montreal). The implantation scheme (the type of intracranial electrodes used, number and location of electrode contacts) varied for each patient and was elaborated by the clinical team based on presurgical non-invasive data (seizure semiology, surface EEG, magnetoencephalography, ictal

single-photon computed tomography, and interictal positron emission tomography data). We considered the following inclusion criteria for patient selection: (1) availability of at least 3 recorded electroclinical seizures; (2) pre-ictal period without sustained (≥ 1 s) or frequent (≥ 1 element/15s) artifacts; (3) minimum of 1h pre-ictal and 1h post-ictal period without electrical or electroclinical seizures.

4.2.2 Pre-processing

Onset and offset of seizures used for analyses were marked by a board-certified epileptologist (DHT). For analysis, we chose pre-ictal and post-ictal epochs of similar duration as the seizure itself. The data were low-pass filtered (third-order Butterworth, zero-phase digital filtering) below 200 Hz, and notch filtered (third-order Butterworth, zero-phase digital filtering) at 60 Hz and 120 Hz. Channels recording non-neuronal signals from faulty electrodes were labeled as bad channels and removed from the database.

4.2.3 Analysis

The dynamic of “local states” for each channel was inferred using RPs (section 4.2.3.1) while the global states were detected based on the overall pattern of the network connections. Briefly, to identify the global states, we first constructed the functional connectivity matrices based on cross-correlation, coherence, phase-locking value (section 4.2.3.1), and a bivariate variation of RPs (Joint Recurrence Plots) (section 4.2.3.2) [1–3]. Then with the application of a state identification algorithm (section 4.2.3.3), we detected the global states. For the sake of easier referencing, our approaches of global state detection based on cross-correlation, coherence, phase-locking value, and Joint Recurrence Plots (JRP) measures were named methods I, II, III, and IV respectively.

4.2.3.1 Functional connectivity measures (normalized cross-correlation, averaged normalized coherence and phase-locking value)

In the first approach (*Method I*) [2], we used the normalized cross-correlation on 1s time windows with no overlap (Eq. 4-1).

$$\rho_{k,l}(m) = |E[(x_k(t) - \mu_{x_{k,m}})(x_l(t) - \mu_{x_{l,m}})]| \quad (4-1)$$

Here, $\rho_{k,l}(m)$ is the normalized cross-correlation between k^{th} and l^{th} channels in the m^{th} time window and $\mu_{x_{k,m}}$ and $\mu_{x_{l,m}}$ are the recording mean value of the m^{th} time window for channel k and l respectively. We then computed the functional connectivity matrices as detailed below.

The second and third methods were employed within a selected patient-specific frequency band. These bands are shown in Table 4-3. To do so, we calculated the average r-spectrum over all channels for each patient and the frequency band with the greatest ictal modulation was determined (see details in Appendix A). Fig.4-1 presents an example of the average r-spectrum for 12 seizures of one patient from our database.

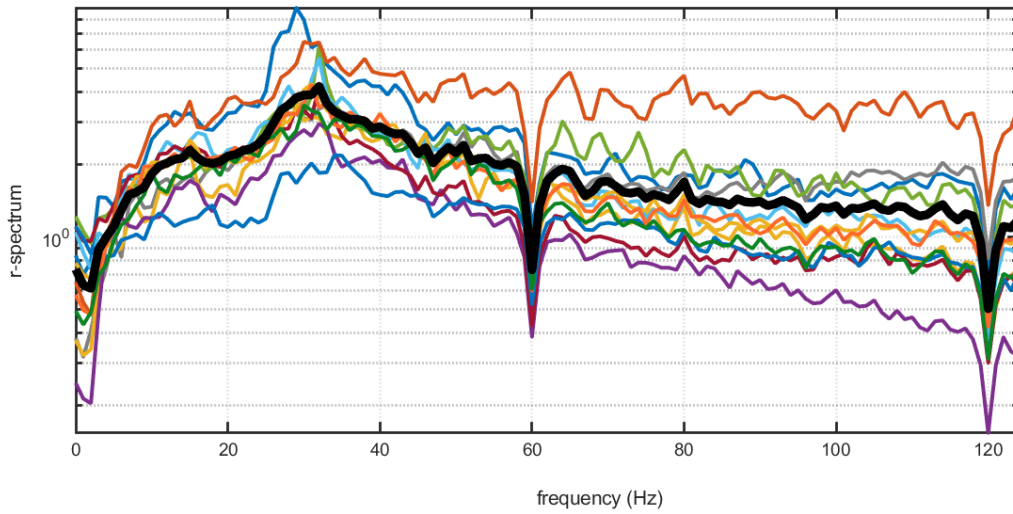


Figure 4-1 r-spectrum for 12 seizures of patient 1 averaged over all channels (colored lines) and the averaged r-spectrum for patient 1 over all 12 seizures (black line). For this patient, the beta band is the one with the largest modulation. The sharp drops at 60 and 120 Hz are due to the application of the notch filter.

In the second approach (*Method II*) [1], within the patient-specific frequency band in each 3s time window with 2s overlap, we computed the functional connectivity matrices based on the averaged normalized coherence $\hat{C}(m)$, starting with:

$$C_{kl}(m) = \frac{|P_{k,l}(m)|^2}{P_{k,k}(m) \cdot P_{l,l}(m)}, \quad (4-2)$$

where, $P_{k,l}(m)$ denotes the cross-spectrum density between the k^{th} and l^{th} channels in the m^{th} time window and $P_{k,k}(m)$ and $P_{l,l}(m)$ represent the autospectrum densities of the k^{th} and l^{th} channels respectively. Then, to find the averaged normalized coherence $\hat{C}(m)$, we calculated the coherence

matrices during 10 min interictal period within the same frequency band and with the same time window length; each element of the matrix $C(m)$ was subtracted by the mean (μ) and divided by the standard deviation (σ) of the elements in the interictal coherence matrices.

In the third approach (*Method III*), within the patient-specific frequency band, for each 1s time window with no overlap, we calculated the functional connectivity matrices using the phase-locking value (PLV):

$$\lambda_{k,l}(m) = \frac{1}{N} \left| \sum_{t=1}^N e^{j|\varphi_k(t) - \varphi_l(t)|} \right|, \quad (4-3)$$

where, $\lambda_{k,l}(m)$ is the PLV between the k^{th} and l^{th} channels for the m^{th} time window and $\varphi_k(t)$ and $\varphi_l(t)$ represent the instantaneous phase of k^{th} and l^{th} channels calculated using Hilbert transform and N is the total number of samples in the time window. Fig. 4-2 shows a pictorial description of this method for the 1s segment of two channels from the recording of one patient in our database.

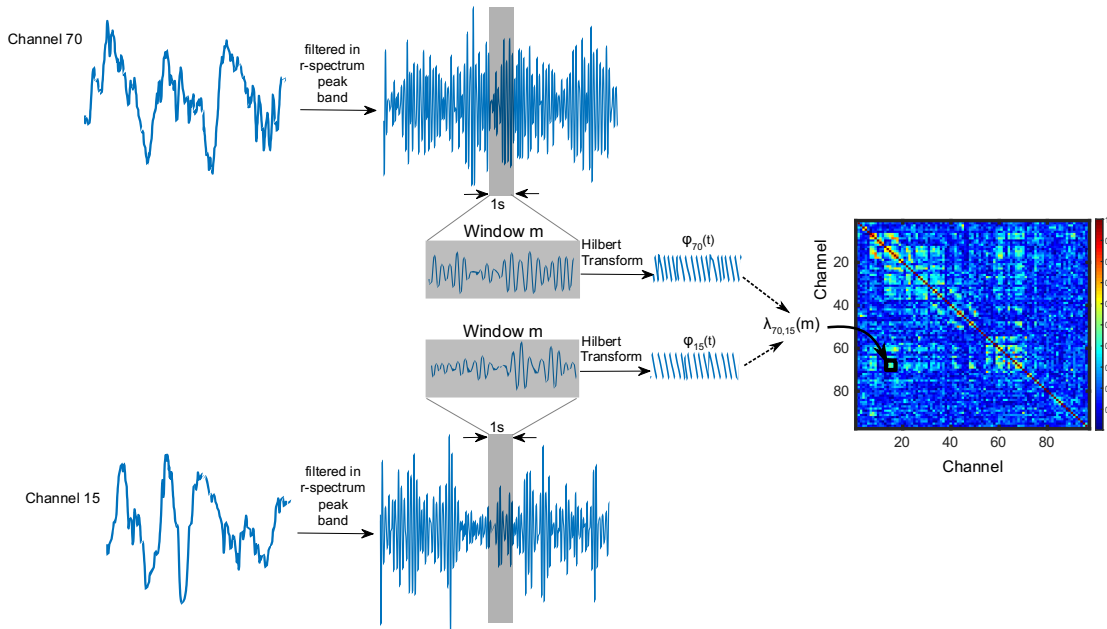


Figure 4-2 A pictorial guide for the computation of the functional connectivity matrix of a 1s time-window based on PLV between channels 70 and 15 of seizure 1 from patient 1 (method III). The instantaneous phases for each time window are computed using Hilbert transform and $\lambda_{70,15}(m)$ is calculated based on equation 4-3. m denotes the window number.

Using these three different methods the functional connectivity matrices were calculated for all time windows during the ictal, pre-ictal and post-ictal periods for each recording (Fig. 4-3b). Then, as it will be explained in section 4.2.3.3, using these functional connectivity matrices, the

configuration similarity matrices were constructed and clustered to detect different states (Fig. 4-3c & 4-3d).

Our fourth approach (*Method IV*), detailed in the section 4.2.3.2.3 and the Appendix A, is based on the dynamical and geometrical characteristics of the system, which can be studied by representing it in its phase space. A phase space is a space in which all states of a dynamical system are described, with each point reflecting one possible state of the system. We reconstructed the d -dimensional phase space using a method based on Takens' theorem [237] which reconstructs the attractor from the time series through using delayed versions of the signal. To estimate the appropriate embedding dimension d and the time delay, we used “*false nearest neighbor*” and “*minimum mutual information*” algorithms, respectively [238,239]. The basis of this method is further detailed in the Appendix A.

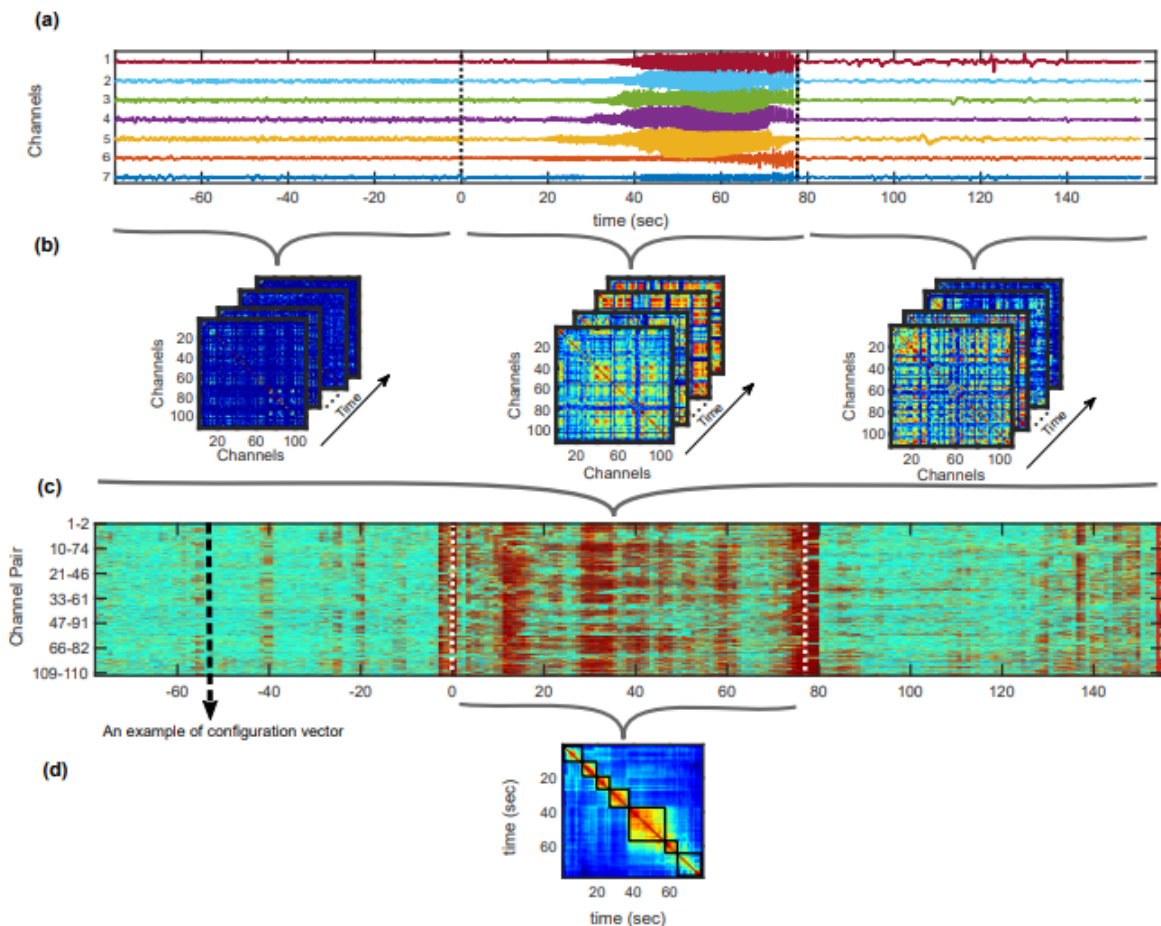


Figure 4-3 a) recordings from seven channels of patient 1 (the total number of channels for this patient is 110). The dotted black lines at $t=0$ and $t=78$ s delineate seizure onset and offset

respectively. b) functional connectivity matrices based on coherence $C(m)$ for each 3s window of the recordings calculated based on equation 4-2 (method II). c) the configuration matrix constructed from all the unique pairwise connections of the normalized coherence matrices (averaged normalized coherence $\tilde{C}(m)$). One configuration vector is shown on this figure with a dotted black line at $t=-52s$ (preictal). d) the configuration similarity matrix for the ictal period. Different states are identified based on section 4.3.3 and depicted with the black rectangles on this configuration similarity matrix.

4.2.3.2 Recurrence Plot (RP), Recurrence Quantification Analysis (RQA) and Joint Recurrence Plot (JRP)

The characteristics of trajectories in phase space for each channel were explored and quantified using the *RPs* and RQA to capture the dynamic of local states. Additionally, in order to compare the performance of RPs with our previous approaches of global state identification (*Method I, II, and III*), we also exploited a bivariate variation of RPs -*JRPs*- to identify global states (*Method IV*). These concepts are further explained in the following sections.

4.2.3.2.1 Recurrence Plot (RP)

Natural systems like the brain are complex, and they have transitions between different behaviors ranging from ordered to chaotic regimes and linear approaches may not be sufficient for their description [254,255]. Ekmann et al. [234] presented an efficient graphical method called Recurrence Plots (RPs) as a tool to compute dynamical parameters from time series. This technique can be applied to nonstationary and rather short time series of complex systems [234,256–260] while, most of the suggested nonlinear descriptors such as Lyapunov exponents and fractal dimensions [261–264], require long data segments [255,265] which is not feasible in the case of ictal recordings as the duration of seizures is not very long (e.g. in this study 67.0 sec on average). Previous studies have shown the suitability of RPs to identify the qualitative changes in the system (even for noisy or short time series data), which is not easily detectable using other methods [6–9].

For creating RPs from a time series, we first constructed the phase space following the procedure described in Appendix A. This yielded an attractor embedded in a d -dimensional space. Assuming vector x_i to be the i^{th} point of the trajectory of the system in the phase space for $i = 1, \dots, N$ (N = the total number of samples), the RP would be an array of dots in a $N \times N$ square plot. A dot at the location (i, j) in this plot means that the distance between x_j and x_i in the phase space is less than the threshold parameter r which was defined as follows: The minimal and maximal component of

x_i for $i = 1, \dots, N$ was determined, i.e. x_{Min} and x_{Max} and were defined as vectors with all minimum and all maximum components, respectively. The maximum phase space diameter was calculated as $|x_{Max} - x_{Min}|$. Then the parameter r was chosen such that a sphere with radius r centered at point x of the reconstructed attractor surrounded 10% of the maximum phase space diameter [235,241].

As represented by Eq.4-4, the RP is a two-dimensional squared matrix \mathbf{R} with two time axes.

$$R_{i,j}(x(t)) = \begin{cases} 1, & \text{if } d(x(i), x(j)) < r, \\ 0, & \text{otherwise,} \end{cases} \quad (4-4)$$

where $d(x(i), x(j))$ shows the distance between the i^{th} and j^{th} points of the trajectory and r is the threshold. As mentioned, in the RP a black dot at (i,j) is plotted if $R_{i,j}=1$.

Changes in the system dynamics are reflected in the changes in the RP patterns [241,243,244]. But in order to interpret these changes accurately, quantification is required. Fig. 4-4 provides examples of these plots for the ictal, pre- and post-ictal periods for one channel of a recording from one of the patients in our database.

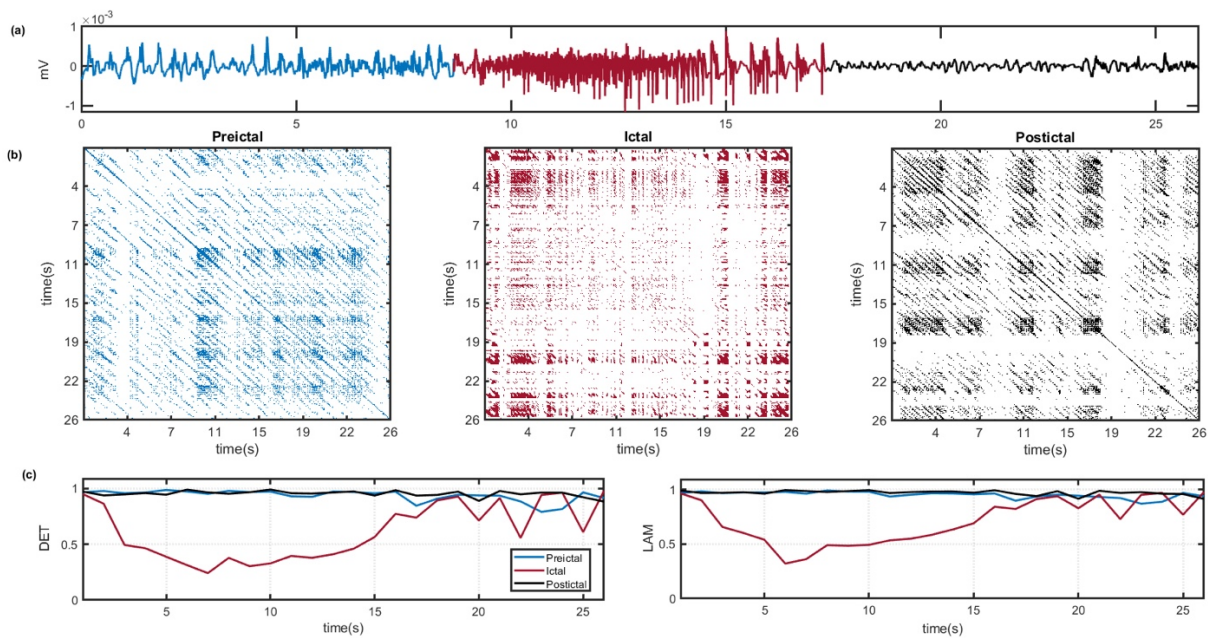


Figure 4-4 a) The recording from one SOZ channel recorded from a patient in our database. The pre-ictal, ictal and post-ictal periods as depicted in blue, red and black respectively (these periods have the same duration). b) RPs for pre-ictal, ictal and post-ictal periods for the recording presented in (a). c) RQA measures calculated based on diagonal and vertical structures of the RPs in (b). The left panel shows DET calculated based on diagonal structures and the right panel represents LAM

calculated based on the vertical structures. As we can see Ictal period displays lower values for both measures.

4.2.3.2.2 Recurrence Quantification Analysis (RQA)

Visual inspection of RPs shows different patterns; however, in order to more systematically quantify the information on RPs, we used Recurrence Quantification Analysis (RQA), as introduced by Zbilut et al. [235,236]. RQA was applied to several physical and biological studies [256,266–268] and has been shown to be useful for the analysis of slight changes and identification of state transitions in the dynamics of complex systems [26–30,33]; e.g. monitoring state transition in environmental signals [272,273], detecting state shifts in electrocardiogram [274] and electroencephalogram recordings [275].

The RP patterns are related to the dynamic of the system [235] and RQA quantifies different structures of these plots; e.g. the diagonal, vertical and horizontal lines [245,246]. The diagonal lines on the RP mean the trajectory visits the same state at different times (state recurrence) and vertical/horizontal lines mean the states persist for a longer time. Since these structures contain relevant information concerning the state transition, in this study they were quantified using two different RQA measures; DET and LAM which respectively define diagonal and vertical/horizontal structures with the following expressions [245,246]:

- *Determinism (DET)* computes the ratio of diagonal line points to recurrent points as calculated based on Eq. 4-4. A diagonal line with length L on the RP means that the trajectory revisited the same region in phase space for L times. Therefore, high DET points towards a lower number of unique states.
- *Laminarity (LAM)* indicates the percentage of recurrent points forming the vertical lines. This is equivalent to the definition of DET for diagonal lines. Since vertical structures display the duration that a state persists, this measure bears an inverse relation to the state transition rate.

The values for DET and LAM changes between 0 and 1. Fig. 4-4b shows the pre-ictal, ictal and post-ictal RPs for one channel of the recordings from one of the patients in our database (Fig. 4-4a) and the two introduced measurements are depicted in Fig. 4-4c. As shown, for this recording,

during the ictal period there are less diagonal and vertical structures compared to pre- and post-ictal periods.

These measurements were calculated for each ictal, pre- and post-ictal epochs for each channel and were averaged over three different channel groups: seizure onset channels (SOZ), the channels to which the seizure propagated within the first 10s of ictal activity (Prop) and the channels with no ictal activity during the seizure (NoIct). These channels were identified for each seizure separately by a board-certified epileptologist (DHT).

4.2.3.2.3 Joint Recurrence Plot (JRP)

To find the global states based on the reconstructed phase space, we first calculated the Joint Recurrence Plots (JRPs) for each 1s time window with no overlap (Eq. 4-5):

$$JR_{i,j}(x^{km}(t), x^{lm}(t)) = R_{i,j}(x^{km}(t)) \cdot R_{i,j}(x^{lm}(t)) \quad (4-5)$$

where, $JR_{i,j}$ is the joint recurrence plot between the k^{th} and l^{th} channels for the m^{th} time window and $R_{i,j}$ is the recurrence plot as defined in Eq. 4-3. In the JRP between two channels, a black dot at (i,j) is plotted if $R_{i,j}$ for both channels equals 1. Therefore, the JRP between every two channels is an $N \times N$ matrix ($N =$ the total number of samples). In the next step, for each time window based on the calculated JRPs, the functional connectivity matrix A was constructed as follows ([276] for more details). Each element of the functional connectivity matrix A was calculated based on the measure introduced in Eq. 4-6.

$$Z_{kl}(m) = \frac{\sum_{i>j} JR_{i,j}(x^{km}(t), x^{lm}(t)) - nq_{km}q_{lm}}{\sqrt{nq_{km}q_{lm}(1-q_{km}q_{lm})}} \quad (4-6)$$

Where q_{km} and q_{lm} denote the rates of the points in the triangular parts of $R(x_{km}(t))$ and $R(x_{lm}(t))$ respectively.

Since the distribution of points in the upper (or lower) triangular half of the JRPs is binomial with the size of $n=s(s-1)/2$, for sufficiently large n , Eq. 4-5 follows the normal distribution with mean 0 and standard deviation of 1. When the element Z_{kl} in time window m is at 0.05 significance level, the element A_{kl} of the functional connectivity matrix for that time window was set to 1, equated zero otherwise.

4.2.3.3 State identification

To identify the global states for each functional connectivity matrix constructed with the application of the described approaches (methods I, II, III, or IV), a configuration vector was formed using the unique pairwise network connections, Fig. 4-3c. We then constructed the configuration matrix by concatenating the configuration vectors of all-time windows as depicted in Fig. 4-3c for one of our recordings. Using the correlation coefficient, the similarity between configuration vectors was then quantified for ictal, pre-ictal and post-ictal periods which resulted in a $T \times T$ configuration similarity matrix for each of these periods Fig. 4-3d.

In the next step, to identify the states, the communities on the configuration similarity matrix were detected using a Louvain-like locally greedy algorithm and by maximizing the modularity index Q (for more details, see [277,278]). These detected communities partitioned the ictal, pre-ictal and post-ictal periods of each seizure into different states; a resolution parameter (γ) defines the scale at which the communities are determined. In this study, the optimal value of this parameter in each method (i.e. I, II, III or IV) was calculated separately for each ictal, pre-ictal and post-ictal period (details in Appendix A).

4.2.3.4 Statistical interpretation

In order to study the dynamic of state transition, separately for each method, we conducted a one-way ANOVA. Then we performed Post-hoc analysis using the Tukey-Kramer test to control for the family-wise error rate of 5% ($\text{FWER} = 5\%$). In the following sections the adjusted p-values are reported as “p-value_{adj}”. In the case of local states, the tests were performed separately for each channel group.

4.3 Results

4.3.1 Patient population

Intracranial EEG recordings from 17 patients (aged between 18 and 49 years old) containing 101 seizures (average duration of 67.0 sec) were analyzed. Table 4-1 summarizes the patients' clinical characteristics, and Table 4-2 provides information regarding the ictal events.

4.3.2 State transition

4.3.2.1 Global state transition rates

From our four different methods to calculate global state transition rates, our results for SF patients indicate significantly lower global state transition rates for the ictal epoch compared to both pre- and post-ictal epochs ($p\text{-value}_{\text{adj}}$ less than 0.05 for methods II, III and less than 0.001 for methods I, IV) (Fig. 4-5a and Table 4-4a and 4-4b). While our findings using these four methods displayed a decrease in state transition rate, only Methods II and III saw a significant decrease ($p\text{-value}_{\text{adj}} < 0.05$ and $p\text{-value}_{\text{adj}} < 0.001$ respectively) in the number of unique states during the ictal period compared to both pre-/post-ictal periods (Fig. 4-6).

Table 4-1 summary of the patients' clinical characteristics. SW = Spike and Wave; FLVA = Fast Low-Voltage Activity, IFG = inferior frontal gyrus; ITG = inferior temporal gyrus; STG = superior temporal gyrus, IPL = inferior parietal lobule, SMA = supplementary motor area, Ins = insular, OF = orbitofrontal, CPC = complex partial seizure, SPS = simple partial seizure, ES = electrical seizure.

<i>Patient ID</i>	<i>Sex</i>	<i>Age at Onset/Surgery</i>	<i>Electrode types</i>	<i>Location of interictal activity</i>	<i>Location of seizure onset</i>	<i>Seizure type</i>	<i>Onset pattern</i>	<i>MRI</i>	<i>Engel class</i>
<i>S1</i>	<i>M</i>	<i>16/49</i>	<i>Grid/strips and depths</i>	<i>R precuneus > R lat T</i>	<i>R precuneus</i>	<i>ES + CPC + 2nd</i>	<i>Sharp wave + multifocal LVFA</i>	<i>Non lesional</i>	<i>I</i>
<i>S2</i>	<i>F</i>	<i>1/32</i>	<i>Grid/strips and depths</i>	<i>R post-CG > L mesial T > R mesial T</i>	<i>R post-CG, pre-CG, pINS >> L mesial T</i>	<i>CPC + ES</i>	<i>Gamma oscillations + focal LVFA</i>	<i>Non lesional</i>	<i>I</i>
<i>S3</i>	<i>F</i>	<i>5/38</i>	<i>Grid/Strips and depths</i>	<i>L (ant ins, IFG, ant STG)</i>	<i>L (ant ins, ant STG)</i>	<i>CPC</i>	<i>Focal LVFA</i>	<i>Non lesional</i>	<i>I</i>
<i>S4</i>	<i>F</i>	<i>21/35</i>	<i>Grid/strips and depths</i>	<i>R IFG > R orbito-F > R ant lat T > R MFG</i>	<i>R IFG > R orbito-F > R ant lat T</i>	<i>CPS + ES</i>	<i>SW + LVFA</i>	<i>Non lesional</i>	<i>I</i>
<i>S5</i>	<i>M</i>	<i>26/35</i>	<i>Grid/Strips/Depths</i>	<i>R IFG, R OF, R med FG/SMA</i>	<i>Non localizing</i>	<i>CPC + ES</i>	<i>Focal LVFA</i>	<i>Non lesional</i>	<i>I</i>
<i>S6</i>	<i>M</i>	<i>16/46</i>	<i>Grid/strips and depths</i>	<i>L Pop-pINS</i>	<i>L Pop-INS</i>	<i>CPC + ES</i>	<i>Focal LVFA</i>	<i>Non lesional</i>	<i>I</i>
<i>S7</i>	<i>F</i>	<i>12/24</i>	<i>Grid/strips</i>	<i>L post-central and precentral gyrus</i>	<i>Left pre-central and post-central gyrus</i>	<i>FIAS, FAS, ES</i>	<i>SW + Focal LVFA</i>	<i>Non lesional</i>	<i>I</i>
<i>S8</i>	<i>M</i>	<i>30/46</i>	<i>Grid/ strips and depths</i>	<i>L Fp, or L SFG, or L mT, or L mid-Ins, or L IFG</i>	<i>L mT, or L Fp, or L F op</i>	<i>FIAS, FAS, ES</i>	<i>LVFA</i>	<i>Non lesional</i>	<i>I</i>

S9	M	20/34	Strips and depths	[R OF + R IFG +/- R ant Ins], or [R Fp +/- R OF], or R mT, or R ant Ins	R OF +/- post ITG	FIAS	SW or slow wave + LVFA	Dysembryoplastic neuroepithelial tumor	I
S10	M	5/23	Grid/strips and depth	R Ant Lat T, R lingual gyrus, R mT, R F op, R MTG, R ITG	R Ant Lat T, R ITG	FIAS	Rhythmic spikes or rhythmic SW	Non lesional	I
S11	F	14/19	Grids/ strips and depths	IPL, heterotopia nodule, cuneus, Post Lat T	IPL, heterotopia nodule, cuneus	FAS +++, FIAS	LVFA	Heterotopia (both periventricular H., and band H.), FCD	I
S12	F	31/32	Grid/strips and depths	L ins + m-T (++++)	L ins + m-T (++++)	SPS + CPC	LVFA	Non lesional	II
S13	F	10/18	Grid/ strips and depths	L Ant Ins, L F op, post OF, L sub-T	L Ant Ins + L IFG	FIAS	Rhythmic SW or rhythmic spikes	Non lesional	II
S14	M	0.5/29	Grid/ strips and depths	R Ant T, R Ant Ins, R MFG, R IFG, R OF, R Fp	R Ant T, R Ant Ins	FAS, FIAS, Absences	Rhythmic SW +/- LVFA	Non lesional	II
S15	M	6/22	Grid/ strips and depth	R Fp, R OF, R MFG, R Ant cingulum, R IFG	R Fp, ROF	FAS, FIAS	Slow wave + LVFA	Non lesional	II
S16	M	10/21	Grid/ strips and depths	LmT, L OF, L Ant Ins, L MTG, L SFG, L parieto-occipital junction, L IPL	L Ant Lat T + L SFG + L MFG + L IFG + L IPL + L parieto-occipital junction	FIAS + FBTCS	Rhythmic slow wave + LVFA	Non lesional	II
S17	M	32/36	Grid, strips and depth	L Ant Ins, L middle Ins, L mT, L IFG, L OF? L Ant cingulum	L [OF + IFG + Ant Ins]	ES, FAS, FIAS, FBTCS	Rhythmic SW or spikes + focal LVFA	FCD	II

For NSF patients, implementing methods I, II and III did not reveal significant differences in global state transition rates between ictal and pre-/post-ictal periods ($p\text{-value}_{\text{adj}} > 0.05$) (Fig. 4-5b, Table 4-4a and 4-4b). The global state transition rates calculated by the last method using JRPs showed a significant difference between the ictal and other periods ($p\text{-value}_{\text{adj}} < 0.001$).

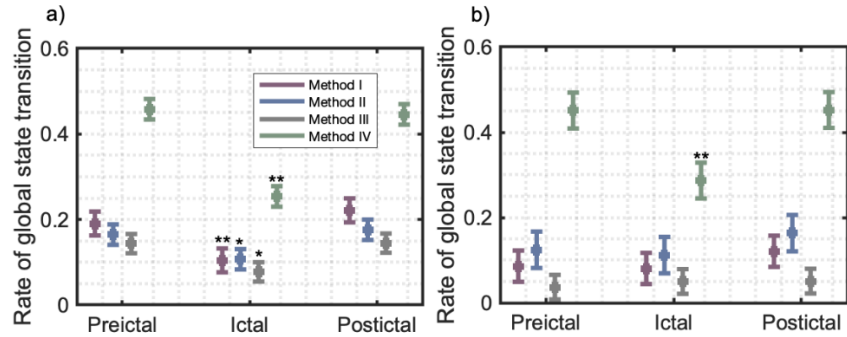


Figure 4-5 a) Rate of global state transition for patients with Engel I surgery outcome (SF). The lines show 95% confidence intervals. b) Rate of global state transition for patients with Engel II surgery outcome (NSF). The lines show 95% confidence intervals.

We further investigated if SF and NSF patients experienced different global state transition rates during ictal activity. Although Fig. 4-5, suggested a more notable decrease in our measures for SF compared to the NSF group, direct comparison between SF and NSF patients revealed no significant difference in global state transition rates during the ictal period ($p\text{-value}_{\text{adj}} > 0.05$ for all four methods) (Fig. 4-7).

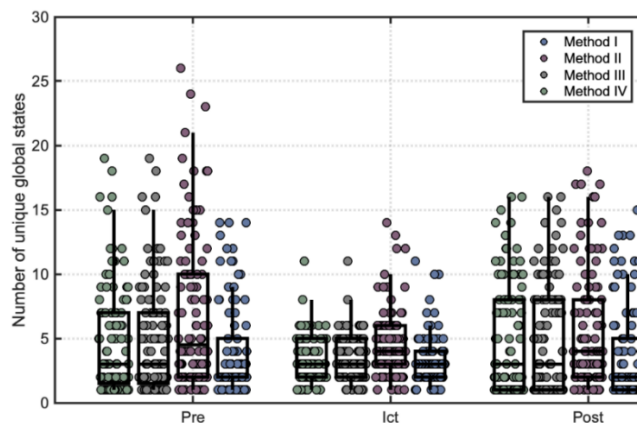


Figure 4-6 The number of unique global states identified in pre-ictal, ictal and post-ictal periods for all seizures using four different methods. For method I, the number of unique states during the ictal period did not show a significant difference from pre- and post-ictal periods. However, for method II it was significantly lower than the post-ictal period ($p\text{-value} < 0.05$) and for method III and JRP's the number of unique states was remarkably lower than both other periods with $p\text{-value} < 0.05$ and $p\text{-value} < 0.001$ respectively.

Table 4-2 The number of seizures and channels for each patient along with descriptive statistics on seizure duration.

<i>Patents ID</i>	<i>Number of seizures</i>	<i>Number of channels</i>	<i>Average seizure duration (Sec)</i>	<i>Standard deviation (Sec)</i>	<i>Shortest seizure (Sec)</i>	<i>Longest seizure (Sec)</i>
<i>S1</i>	12	97	43.4	10.8	26.1	70.2
<i>S2</i>	19	105	32.3	7.2	22.9	47.6
<i>S3</i>	9	61	54.4	20.7	23.3	78.9
<i>S4</i>	5	82	19.6	3.5	16.3	24.6
<i>S5</i>	7	93	42.1	12.8	27.1	64.3
<i>S6</i>	4	90	112.6	63.8	67.9	204.1
<i>S7</i>	4	73	63.6	26.8	26.1	89.7
<i>S8</i>	3	110	69.7	44.6	18.2	97.1
<i>S9</i>	5	106	190.6	181.8	72.6	495.3
<i>S10</i>	4	105	86.2	32.0	38.9	109.2
<i>S11</i>	3	113	35.8	18.4	15.3	51.0
<i>S12</i>	4	102	59.9	46.7	15.3	111.2
<i>S13</i>	3	105	93.1	1.7	91.9	94.3
<i>S14</i>	5	101	114.9	10.8	105.8	131.9
<i>S15</i>	4	114	19.1	3.0	15.1	22.4
<i>S16</i>	5	106	37.2	13.2	23.9	59.4
<i>S17</i>	5	111	64.1	14.7	41.9	76.9
<i>total</i>	101		67.0			

Table 4-3 The patient-specific frequency bands and number of unique global states computed for each method.

Patient ID	frequency band	Method I	Method II	Method III	Method IV
		$(\mu_{Pre} \pm \sigma_{Pre}, \mu_{Ict} \pm \sigma_{Ict}, \mu_{Post} \pm \sigma_{Post})$	$(\mu_{Pre} \pm \sigma_{Pre}, \mu_{Ict} \pm \sigma_{Ict}, \mu_{Post} \pm \sigma_{Post})$	$(\mu_{Pre} \pm \sigma_{Pre}, \mu_{Ict} \pm \sigma_{Ict}, \mu_{Post} \pm \sigma_{Post})$	$(\mu_{Pre} \pm \sigma_{Pre}, \mu_{Ict} \pm \sigma_{Ict}, \mu_{Post} \pm \sigma_{Post})$
S1	Beta	(6.0±3.3,3.9±1.3,5.9±2.8)	(9.5±5.2,6.0±3.1,14.3±5.1)	(9.4±3.1,3.9±1.8,9.1±1.6)	(9.2±3.3,6.4±2.6,9.3±3.9)
S2	Gamma	(9.0±3.1,5.7±2.5,9.1±3.3)	(4.8±5.3,3.7±2.9,6.5±6.8)	(9.4±3.1,3.9±1.8,9.1±1.6)	(10.2±1.5,6.8±1.7,9.5±1.5)
S3	Gamma	(1.4±0.5,2.1±0.8,2.0±0.7)	(3.3±1.3,3.8±1.1,3.0±0.7)	(9.4±3.1,3.9±1.8,9.1±1.6)	(6.9±1.3,5.2±1.9,7.4±1.5)
S4	Theta	(2.4±1.1,2.2±1.3,1.8±0.8)	(4.8±2.0,5.4±1.3,4.8±0.4)	(5.0±1.4,4.8±0.8,5.4±1.1)	(11.2±0.4,7.0±1.0,9.0±1.9)
S5	Delta	(1.7±0.7,1.7±0.5,1.7±0.8)	(8.1±0.7,5.4±0.5,6.8±1.5)	(7.1±1.9,5.6±0.5,6.6±1.7)	(8.8±1.4,6.0±2.3,8.6±2.5)
S6	Theta	(1.5±0.6,2.5±0.6,1.5±0.6)	(1.7±0.9,3.5±0.6,1.5±0.6)	(9.7±6.3,4.5±1.7,8.5±5.2)	(10.7±1.5,6.0±0.0,8.3±3.0)
S7	Delta	(1.5±1.0,2.5±1.3,2.2±1.3)	(7.5±5.0,4.5±2.1,7.7±6.9)	(8.0±3.9,2.5±0.6,6.7±7.6)	(7.7±1.2,5.5±1.9,7.7±1.3)
S8	Beta	(5.3±5.8,3.3±1.5,5.0±4.4)	(9.0±6.2,4.3±2.3,4.7±3.1)	(2.3±2.3,3.0±1.7,3.0±2.6)	(10.0±6.1,7.7±4.7,10.0±5.3)
S9	Beta	(1.2±0.4,3.0±0.7,1.8±0.4)	(6.2±6.1,3.8±1.1,8.2±8.9)	(1.0±0.0,2.4±0.5,1.2±0.4)	(7.0±1.0,3.0±0.0,4.7±1.1)
S10	Beta	(1.5±0.6,2.5±0.6,1.5±0.6)	(8.5±6.4,5.0±1.4,8.0±5.0)	(3.2±4.5,2.5±0.6,1.5±0.6)	(9.5±3.7,6.5±3.3,10.2±2.1)
S11	Gamma	(2.7±2.1,3.3±2.3,5.7±6.4)	(10.7±4.2,9.7±4.0,9.7±1.5)	(3.0±1.7,1.0±0.0,1.7±1.1)	(10.7±1.5,6.3±2.1,9.0±1.7)
S12	Delta	(1.4±0.5,2.6±1.1,1.8±1.3)	(2.4±1.5,2.6±1.5,2.8±2.5)	(5.6±2.3,4.0±1.6,3.8±2.2)	(6.8±0.8,6.4±2.4,5.6±1.5)
S13	Beta	(1.5±0.7,2.5±0.7,2.0±1.4)	(2.0±0.0,3.0±0.0,3.0±1.4)	(1.3±0.6,2.3±0.6,2.3±1.5)	(5.0±0.0,4.5±0.7,9.0±2.8)
S14	Alpha	(2.0±0.0,2.8±0.8,1.8±0.8)	(1.4±0.5,4.2±1.2,1.8±0.8)	(1.0±0.0,2.2±0.4,1.4±0.5)	(6.0±1.0,5.0±1.0,7.4±1.1)

S15	Beta	(2.5±1.9,3.5±1.3,2.0±0.8)	(6.5±1.3,5.2±0.5,5.7±1.3)	(1.5±1.0,2.0±0.0,3.0±2.8)	(8.8±3.0,7.4±1.7,7.8±1.5)
S16	Gamma	(1.6±1.3,2.0±1.2,1.8±1.3)	(5.8±6.1,5.8±5.5,14.4±5.9)	(1.0±0.0,1.0±0.0,1.0±0.0)	(9.2±0.8,7.8±1.1,8.8±2.2)
S17	Beta	(1.0±0.0,2.8±0.8,2.2±0.8)	(5.0±2.1,5.2±1.3,6.2±4.5)	(1.0±0.0,4.2±0.8,2.2±0.8)	(10.6±1.7,5.4±0.9,14.0±3.7)

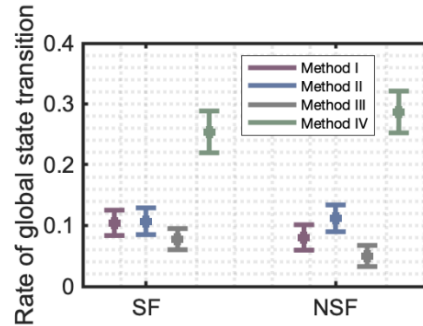


Figure 4-7 The comparison of global state transition rate during ictal activity between SF and NSF patients. None of the applied methods (I-IV) reported significant difference between these two groups ($p\text{-value} > 0.05$).

Table 4-4 a) Comparing global state transition rates between pre-ictal, ictal and post-ictal periods using one-way ANOVA conducted separately for SF and NSF patients. b) The adjusted p-values ($p\text{-value}_{adj}$) based on the post-hoc analysis using Tukey-Kramer test to control for the family-wise error rate of 5% (FWER = 5%).

a)	Method I		Method II		Method III		Method IV	
	SF	NSF	SF	NSF	SF	NSF	SF	NSF
F	$F(2,225)=12.86$	$F(2,75)=1.02$	$F(2,225)=6.59$	$F(2,75)=1.13$	$F(2,225)=7.98$	$F(2,75)=0.20$	$F(2,225)=57.89$	$F(2,75)=17.03$
P-values	5.1e-6	0.36	0.0016	0.32	4.47e-4	0.81	9.4e-21	7.2e-7

b)	Method I		Method II		Method III		Method IV	
	SF	NSF	SF	NSF	SF	NSF	SF	NSF
Pre-ictal	9.1e-4	0.98	0.0129	0.93	0.0017	0.84	9.5e-10	9.27e-6
Post-ictal	2.9e-6	0.39	0.0020	0.32	0.0014	1.00	9.5e-10	7.33e-6

4.3.2.2 Local state transition rates

Using DET and LAM, as indicators of local state transitions, we respectively studied the diagonal and vertical structures on the RPs and observed remarkable changes during the ictal period compared to pre- and post-ictal periods. These measures were averaged over three different channel groups (SOZ, Prop and NoIct) as explained in section 4.2.3.2.2.

For SF patients, both DET and LAM showed a significant decrease during the ictal period compared to pre- and post-ictal periods for SOZ ($p\text{-values}_{\text{adj}} < 0.001$) and Prop groups ($p\text{-value}_{\text{adj}}$ less than 0.05 and 0.001 compared to pre- and post-ictal periods respectively). However, for the NoIct group, the decrease was only significant when compared to the pre-ictal epoch ($p\text{-value}_{\text{adj}} < 0.05$) (Fig. 4-8a, Table 4-5).

Table 4-5 a) Calculated p-values for RQA measures for SF patients using one-way ANOVA. b) The adjusted p-values based on the post-hoc analysis of Table 5a using Tukey-Kramer test to control for the family-wise error rate of 5% (FWER = 5%).

a)	DET			LAM		
	SOZ	Prop	NoIct	SOZ	Prop	NoIct
F	$F(2,192)=24.27$	$F(2,180)=8.81$	$F(2,108)=0.0056$	$F(2,192)=23.95$	$F(2,180)=8.88$	$F(1,108)=5.46$
P-values	$3.9e-10$	$2.2e-4$	0.28	$5.2e-10$	$2.08e-4$	0.0055

b)	DET			LAM		
	SOZ	Prop	NoIct	SOZ	Prop	NoIct
Pre-ictal	$9.12e-8$	0.0036	0.0038	$4.41e-8$	0.0023	0.0037
Post-ictal	$1.33e-9$	$2.41e-4$	0.2841	$2.03e-9$	$2.91e-4$	0.2594

For NSF patients those measurements showed no significant changes for SOZ and NoIct groups ($p\text{-values}_{\text{adj}} > 0.05$). However, for the Prop group, they decreased when compared to either pre-ictal or post-ictal periods ($p\text{-values}_{\text{adj}} < 0.05$) (Fig. 4-8b, Table 4-6).

Table 4-6 a) Calculated p-values for RQA measures for NSF patients using one-way ANOVA. b) The adjusted p-values based on the post-hoc analysis of Table 6a using Tukey-Kramer test to control for the family-wise error rate of 5% (FWER = 5%).

a)	DET			LAM		
	SOZ	Prop	NoIct	SOZ	Prop	NoIct
F	$F(2,72)=0.23$	$F(2,72)=3.51$	$F(2,36)=0.70$	$F(2,72)=0.34$	$F(2,72)=3.89$	$F(2,36)=0.80$
P-values	0.7926	0.0350	0.5009	0.7116	0.0249	0.4558

b)	DET			LAM		
	SOZ	Prop	NoIct	SOZ	Prop	NoIct
Pre-ictal	0.8028	0.0372	0.6726	0.7553	0.0239	0.6640
Post-ictal	0.9952	0.1232	0.9553	0.9999	0.1289	0.9288

These findings suggested a more noticeable decrease in the calculated measures for SF patients compared to NSF patients (Fig. 4-8). To explore this difference further during the ictal activity, we conducted a direct comparison between SF and NSF patients separately for each channel group.

As we can see in Fig. 4-9, DET, and LAM measures reported remarkably lower values for SF compared to NSF patients for SOZ group (with p-values 0.0016 and 0.005 respectively) while the Prop and NoIct group revealed no significant difference between SF and NSF patients during the ictal activity (p-values>0.05).

We observed notable variations for the average embedding dimensions and time delays that were applied in constructing the RP. We calculated the embedding dimensions and time delays used in constructing the RPs for each channel separately. Their average values over all channels for each seizure is represented in Appendix A, Fig. A5 which displays notable variations over different periods. In particular, the averaged embedding dimension for both SF and NSF patients was significantly higher for the ictal period comparing the pre-ictal (p-value<0.05) and post-ictal (p-value<0.001) periods. The average time delay was significantly lower during the ictal period in comparison to both pre- and post-ictal periods for SF patients (p-value<0.05 and p-values<0.001 respectively) and only to the post-ictal period for NSF patients (p-value<0.001).

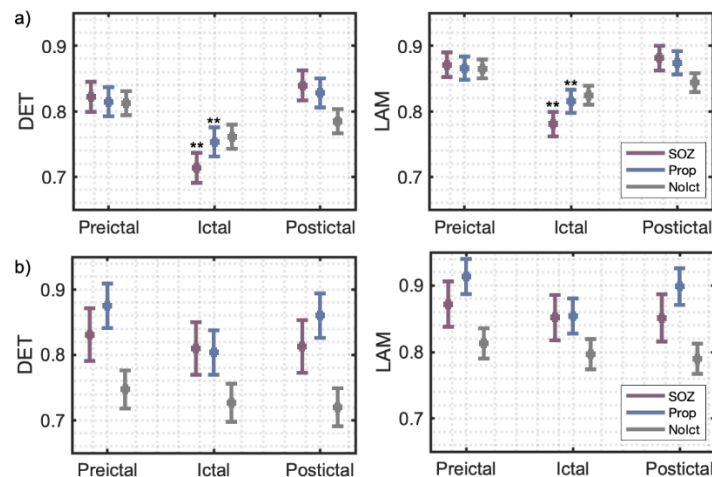


Figure 4-8 RQA measures averaged over three different channel groups (seizure onset channels (SOZ), the channels to which the seizure propagated within the first 10s of ictal activity (Prop) and the channels with no ictal activity during the seizure (NoIct)) a) for SF patients. b) for NSF patients. The lines show the 95% confidence intervals over seizures.

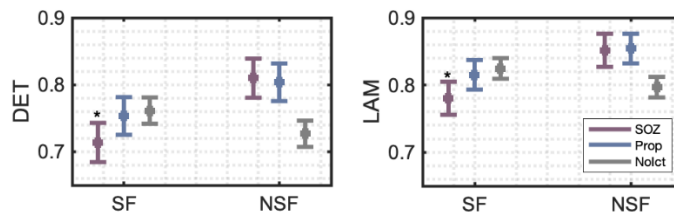


Figure 4-9 Comparing RQA measures averaged over three different channel groups (seizure onset channels (SOZ), the channels to which the seizure propagated within the first 10s of ictal activity (Prop) and the channels with no ictal activity during the seizure (NoIct)) between SF and NSF patients. The lines show the 95% confidence intervals over seizures.

4.4 Discussion

One common simplification in many mathematical models of epileptic activity is the assumption of the periodic behavior of the neural population in the course of the seizure [107,212,279,280]. Attempts at detecting these patterns of recurrent states [1–3] have reported conflicting results. Using different approaches in the time domain, frequency domain, and phase space, we studied these patterns and found a consistent pattern for the dynamic of the global state transition rate: a significant decrease in the global state transition rate for ictal epochs compared to pre- and post-ictal periods for SF patients.

The differences in the results of the previous studies [1–3] could stem from the variations in their methodology, database or the validity of their underlying assumption on the existence of these recurrence states. Their methodology varied in both their employed approach to calculating the functional connectivity measures and their adopted clustering algorithm for state detection. In this study, we implemented their approach for calculating functional connectivity matrices but adopted the same clustering algorithm across all to restrict the source of variability to one item. In other words, we investigated if the functional connectivity calculation was the source of the observed variability among the previous studies. Accordingly, the application of their different functional connectivity measures on the same database allowed us to rule out the effect of their choice of functional connectivity measure as the source of the discrepancy in their reported results. More explicitly, we utilized correlation, coherence and phase-locking as suggested by previous studies [1–3] and elaborated our analysis using another analytical method (a bivariate variation of RPs) that had not been applied before for this purpose to the best of our knowledge. In our first approach, we used correlation which is among the simplest and commonly used methods for functional

connectivity calculation. Correlation shows the dependence between recordings; however, it cannot provide any information on the association of the recordings in the frequency domain and different frequency bands. In the second approach, we constructed functional connectivity matrices based on coherence. Coherence calculates the relation between signals in the frequency domain and depends on both phase and amplitude consistency between two signals [281]. In our third approach, we used an alternate measure, Phase-Locking Value (PLV), that considers only the relative phase to quantify the interactions between signals [282]. This measure is robust to amplitude variations and extracts information only based on the relative phase [232,233]. Finally, our approach using JRPs quantifies the interaction between signals in the phase space which is a useful asset for nonlinear and complex systems like the brain [241]. As discussed, while these four approaches covered different aspects of interactions between recordings, all pointed in the same direction which was a significant decrease in state transition rates during the ictal period compared to the pre- and post-ictal periods.

Interpretations of state transition in the current study and other research endeavors are mainly based on clustering techniques. Discrepant results in prior studies could have been due to unmet assumptions of applied clustering methods. In our clustering algorithm, we found the optimal resolution parameter for each ictal, pre- and post-ictal periods of each seizure separately (Appendix A. Fig. A1) and employed the algorithm iteratively until consistent communities were detected. Application of the different clustering algorithms used in prior studies along with the same functional connectivity measure could also have explained prior discrepant findings.

While applied time and frequency domain analyses can identify global states based on the overall pattern of functional connectivity matrices, one of their limitations is the lack of spatial resolution in state identification. Because different regions of the brain might not simultaneously enter the same state, the study of local states could improve our understanding of the dynamic of seizures. With the applied state space method (RPs), we captured spatial information regarding the changes in the dynamic of the local states. There were considerable fluctuations in the obtained variables from the patterns of RPs diagonal and vertical structures. From the calculated diagonal and vertical structures of our RPs, we inferred about the local state transition rates and the number of unique states. More explicitly, the lower values of RQA measures for diagonal structures imply a lower amount of time spent on revisiting the same state and lower values of vertical structures address a shorter time interval that one state persists which respectively lead to a higher number of unique

states and higher local state transition rates. For SF patients, we could infer a higher number of unique local states and higher local state transition rates during ictal periods compared to both pre- and post-ictal periods.

Hence, while our findings for SF patients pointed towards lower global state transition rates for ictal epochs compared to pre- and post-ictal epochs, the local state transition rates (especially for SOZ and Prop groups) for these patients showed higher values. These findings are not necessarily mutually exclusive. Each global state represents a unique pattern of network connections and lower global state transition implies the persistence of the same pattern of synchrony/desynchrony among neural populations. The local states reveal if the trajectory of each channel persists or revisits the same location in the state space. Therefore, higher values of local state transition rates for SOZ and Prop channels display their instability. One possible explanation for this observation could be the reported isolation of SOZ for SF patients shortly after seizure initiation [1] which may not allow the highly unstable SOZ channels to drive the network into a dynamic with high state transition rates. For NSF patients, the SOZ is not isolated [1]; this mutual interaction between the network and the SOZ in NSF patients might be the reason that SOZ channels did not experience high state transition rates. Such a disparity between different scales of the analysis has also been reported in other aspects of ictal activities [283].

Although our findings for both local and global states suggested more noticeable changes in the calculated measures for SF patients compared to NSF patients, a direct comparison between SF and NSF patients revealed that this difference was only significant for local states. In particular, the state transition of the SOZ group was significantly different between SF and NSF patients while the Prop and NoIct groups displayed no significant differences. These findings pointed towards an inherent difference in the state transition dynamics of the SOZ channels between SF and NSF patients which could be explained by the inaccurate localization of SOZ in patients with unfavorable surgery outcome [284]. An interesting avenue for future works would be using a larger database to explore whether the analysis of ictal local state transitions could be a useful marker to predict surgical outcome.

4.5 Conclusion

The global states provided us with information on the overall changes in the state of the brain and offered an understanding of the state transition dynamics in different regions. We further extended

our analysis to the study of local states. Our findings pointed to distinct dynamics for state transitions at different scales; while during ictal activity, the brain globally persists in a state for a longer time, locally, it undergoes a higher rate of state transition in some regions like SOZ. Finding state transitions locally in different regions enhances our understanding of the ictal mechanism, and its application in implementing therapeutic measures can be the focus of future studies. Moreover, we discovered different patterns for local state transitions between SF and NSF patients which can have practical application in predicting surgical outcome.

Acknowledgments

This research was supported by CIHR project grant (390044); Canada Research Chair Program (DKN); NSERC Discovery Grant RGPIN-2014-06089 (PP).

CHAPTER 5 ARTICLE 2: INTRACRANIAL EEG SEIZURE ONSET AND TERMINATION PATTERNS AND THEIR ASSOCIATION

Leila Abrishami Shokooh^{1,2,*}, Dènahin Hinnoutondji Toffa³, Philippe Pouliot¹, Frédéric Lesage^{1,4}, Dang Khoa Nguyen^{2,3}

¹ École Polytechnique de Montréal, Université de Montréal, C.P. 6079, succ. Centre-Ville, Montreal, H3C 3A7, Canada

² Centre de Recherche du Centre Hospitalier de l'Université de Montreal (CHUM), Montreal, QC, Canada

³ Neurology Division, Centre Hospitalier de l'Université de Montréal (CHUM), 1000 Saint-Denis, Montreal, H2X 0C1, Canada

⁴ Research Centre, Montreal Heart Institute, Montreal, Canada

* Correspondence to Leila Abrishami Shokooh, École Polytechnique, Université de Montréal, C.P. 6079 succ. Centre-Ville, Montreal, H3C 3A7; e-mail: Leila.abrishami-shokooh@polymtl.ca

This article has been published in the journal of Epilepsy Research, August 2021.

Abstract

Objective: The study of seizure onset and termination patterns has the potential to enhance our understanding of the underlying mechanisms of seizure generation and cessation. It is largely unclear whether seizures with distinct onset patterns originate from varying network interactions and terminate through different termination pathways.

Methods: We investigated the morphology and location of 103 intracranial EEG seizure onset and termination patterns from 20 patients with drug-resistant focal epilepsy. We determined if seizure onset patterns were associated with specific termination patterns. Finally, we looked at network interactions prior to the generation of distinct seizure onset patterns by calculating directed functional connectivity matrices.

Results: We identified nine seizure onset and six seizure termination patterns. The most common onset pattern was Low-Voltage Fast Activity (36%), and the most frequent termination pattern was Burst Suppression (44%). All seizures with fast (>13Hz) termination patterns had a fast (>13Hz) onset pattern type. Almost any onset pattern could terminate with the Burst Suppression and rhythmic Spike/PolySpike and Wave (rSW/rPSW) termination patterns. Seizures with a fast activity onset had higher inflow to the seizure onset zone from other regions in the gamma and high gamma frequency ranges prior to their generation compared to seizures with a slow onset.

Significance: Our observations suggest that different mechanisms underlie the generation of different seizure onset patterns although seizure onset patterns can share a common termination pattern. Possible mechanisms underlying these patterns are discussed.

Keywords: focal epilepsy, network analysis, directed functional connectivity, seizure onset patterns, seizure termination patterns, ECoG

5.1 Introduction

Epilepsy is characterized by recurrent spontaneous seizures. With 50 million people affected worldwide [17], it is one of the most common chronic neurological disorders. Despite progress - both in our understanding of the pathophysiology and the treatment of epilepsy - further work is necessary as epileptic seizures in close to a third of patients remain uncontrolled. A more in-depth understanding of the neurophysiological mechanisms underlying seizure initiation, propagation, and termination is imperative for attaining improved therapeutic measures.

Because of their potential importance in understanding ictogenesis, seizure onset patterns have drawn considerable attention [59,60,285]. For instance, the association between seizure onset patterns and the underlying pathological substrates [59] as well as the relevance of seizure onset patterns in predicting the outcome of the resection surgery [66–68] have been widely investigated. To our knowledge, however, these studies have never looked if seizure onset patterns are associated with specific seizure termination patterns. On the other end, contrary to seizure onset patterns, seizure termination patterns have received little attention [225,226]; this is unfortunate since investigating the intrinsic mechanisms that terminate seizures could potentially lead to new therapeutic approaches [286–289]. Moreover, exploring the associations between seizure onset and termination patterns could offer some insights into the question of whether different termination patterns associate with different onset patterns?

While some onset patterns have been associated with the activity of specific brain regions [161] and synaptic mechanisms [175,202], epilepsy is commonly considered as a network disease [124,125,130] and it remains to be fully comprehended whether different network topological features precede the formation of seizures of varying onset patterns. According to the network view, it is the interaction between different regions - not just the seizure generating region- that initiates seizures [124,128,130,166]. Many studies have revealed complex interactions between the

seizure onset zone (SOZ) and other regions (NonSOZ) during ictogenesis [128,133,290,291]. Based on these observations, different mechanisms have been suggested for the generation of epileptic activity. Some studies have invoked a major role for the SOZ in affecting and invading the surrounding regions [124,164,166,168]; whereas, other studies have viewed the failure of the surrounding regions to contain the abnormal activity [147,291] as a driving force for the generation of ictal activity. Nonetheless, the etiology of interactions between the SOZ and NonSOZ across different seizure onset patterns has yet to be elucidated.

In this study, we aimed at investigating the association between seizure onset and termination patterns and illuminating the network interactions leading to the generation of seizures with different onset patterns. To this end, we first classified seizure onset and termination patterns on a set of 103 seizures recorded from 20 patients with drug-resistant focal epilepsy undergoing intracranial EEG investigations and explored potential associations between the onset and termination patterns. We then investigated potential differences among epileptic networks generating different seizure onset patterns by exploring the interaction between SOZ and NonSOZ during the transition from interictal to different identified onset patterns using a measure of directed functional connectivity.

5.2 Methodology

5.2.1 Patients

The iEEG data for this study came from 20 patients with drug-resistant focal epilepsy who were candidates for resective surgery. All patients had previously undergone a presurgical evaluation using video-scalp EEG, magnetic resonance imaging (MRI), ictal single-photon emission computed tomography (SPECT), positron emission tomography (PET), and magnetoencephalography (MEG). But as these non-invasive methods were insufficient to confidently localize the epileptogenic zone and/or because functional mapping with cortical electrical stimulation was necessary, an invasive EEG evaluation was conducted using a combination of strip, grid, and depth electrodes positioned in areas of suspected epileptogenicity. Patients with good outcome postoperatively (Engel class I-II; minimum follow-up 3 years) and minimum of 3 recorded clinical seizures were chosen; patients who had recordings with faulty

electrodes were excluded. Recordings were performed using a 128-channel recording system (Harmonie, Stellate, Montreal, Canada) with a sampling frequency of 2000Hz.

5.2.2 Pre-processing

Bad electrodes were identified by visual inspection of the recordings and removed. The remaining recordings were band-pass filtered for each frequency band of interest (delta, 1–4 Hz; theta, 4–8 Hz; alpha, 8–13 Hz; beta, 13–30 Hz; gamma, 30–90 Hz; high gamma, 90–250 Hz) using a zero-phase shift, fourth-order Butterworth filter. Since frequencies lower than 1 Hz are more prone to the slow drift noise contamination, this range of very low frequencies was not considered.

5.2.3 Seizures

The time of seizure initiation and termination as well as the onset and termination patterns were identified and labeled by a board-certified epileptologist (DHT) and reviewed by a senior epileptologist (DKN). The first unambiguous EEG change from background activity developing into ictal activity was considered as the seizure onset [59]. To identify seizure onset and termination patterns, the iEEG recordings in a 5-sec window respectively after seizure onset and before seizure termination were considered. Then, the onset and termination patterns were inspected by visual inspection of the recordings and considering their amplitude and frequency characteristics. The SOZ was defined as the channels with the earliest unequivocal ictal iEEG discharges and all other channels were defined as NonSOZ.

We explored the spatiotemporal pattern of seizure termination by comparing channels with ictal activity upon seizure termination (*termination zone*) with SOZ channels. To this end, we identified the channels with ictal activity at seizure termination and classified them as *In*, *Out*, *In-Out* or *Diffuse* using the following criteria:

In: the ictal activity upon seizure termination was limited to SOZ channels.

Out: the ictal activity upon seizure termination was outside the SOZ channels (i.e., in NonSOZ channels).

In-Out: the ictal activity upon seizure termination was observed in both SOZ and NonSOZ channels but not in all channels.

Diffuse: the ictal activity was observed in all channels at seizure termination.

5.2.4 Analysis

To investigate the potential differences among epileptic networks generating different seizure onset patterns, we studied the network interactions prior to the generation of these different onset patterns. To this end, we calculated the directed functional connectivity matrices as described in the following section during the preictal periods.

5.2.4.1 Functional connectivity measure

To establish a connectivity measure, we first calculated the Phase Slope Index (PSI) to estimate the flux direction. PSI measures the directionality of coupling between electrophysiological recordings based on their spectral properties [247]. Specifically, PSI estimates the slope of the phase difference between the driver and recipient versus the frequency; since different waves travel with the same speed, the phase difference between the driver and receiver increases with frequency which leads to a positive slope of the phase spectrum. PSI could more robustly estimate the directionality of coupling and is more insensitive to mixtures of independent sources compared to more classical measures like Granger Causality which could yield highly significant false detections [247]. We calculated PSI using the formula introduced in [247] (Eq.5-1) for all frequency bands of interest and between all channel pairs during 1-minute preictal period for each seizure. Our choice of 1-minute preictal period was selected based on the studies suggesting changes in the functional network features in about a minute before seizure onset [292].

$$\hat{\psi}_{ij} = \Im(\sum_{f \in F} C_{ij}^*(f) C_{ij}(f + \delta f)), \quad (5-1)$$

where $C_{ij}(f) = S_{ij}(f)/\sqrt{S_{ii}(f)S_{jj}(f)}$ denotes the complex coherency and S is the cross-spectral matrix. δf represents the frequency resolution and $\Im(\cdot)$ keeps the imaginary part. The range of frequencies for finding the slope of the phase spectrum is defined as f . A positive PSI between signals A and B shows that signal A exerts an overall greater influence on signal B. Therefore, the mean PSI of a region would be positive if the signals from that region provide more information than what they receive, and it would be negative if they receive more than what they provide.

5.2.4.2 Surrogate Analysis

To establish statistical significance thresholds for PSI interaction metrics, we compared the calculated PSI from the original time series to the values from 100 generated surrogate time series and estimated their statistical significance. The surrogate time series were generated by taking a

Fourier transform of the original broadband time-series, randomizing the Fourier phases, and then performing an inverse Fourier transform to construct the surrogate data set. Finally, the frequency bands were extracted, and PSI was recalculated using (Eq.5-1). Nonsignificant PSIs ($p\text{-value} > 0.05$) were set to zero [293] and the significant positive and negative PSIs were respectively set to +1 and -1.

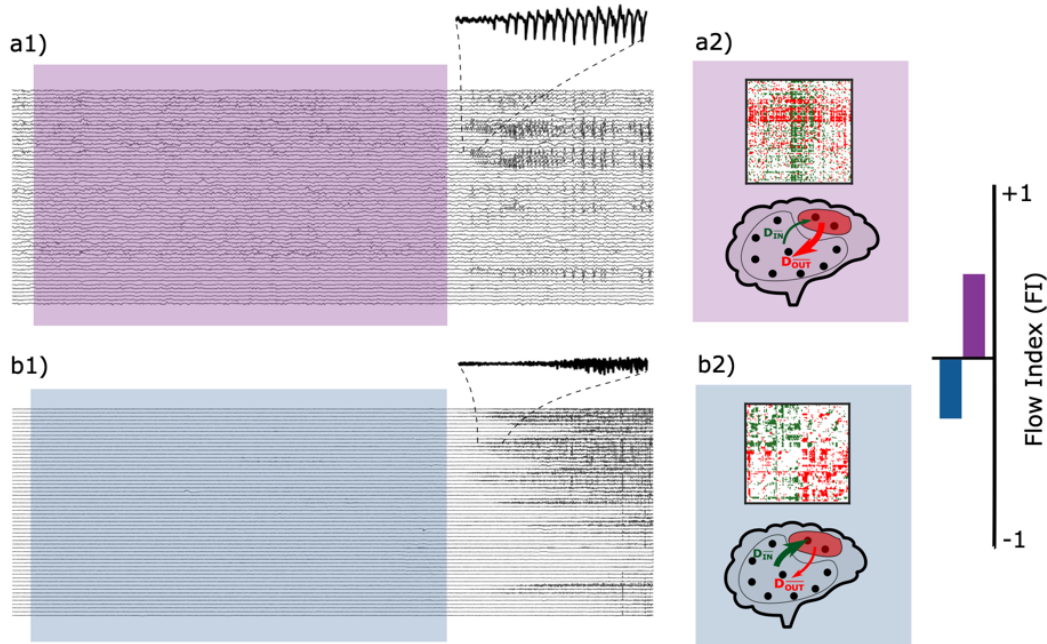


Figure 5-1 Calculating Flow Index (FI) for seizures with a1) slow and b1) fast onset patterns. The PSI matrices in gamma frequency band during the preictal periods (highlighted in a1 and b1) of recordings with slow and fast onsets are respectively displayed in top (a2) and (b2). In bottom (a2) and (b2) the averaged inflow and outflow to seizure onset zones are presented for the corresponding functional connectivity matrices. The Flow Index (FI) for these two networks are calculated based on Eq.5-1 and shown on the left side of the figure.

5.2.4.3 Flow Index (FI)

Each channel is represented as a node in the calculated functional connectivity matrices and the link between each pair of nodes is calculated using PSI as described in the previous section. For each node, we summed all the ingoing links (D_{IN}) and all the outgoing links (D_{OUT}). To specify whether the SOZ region was the driver or receiver prior to seizure onset, we averaged D_{IN} and D_{OUT} measures over SOZ channels ($D_{IN}^{\text{SOZ}}, D_{OUT}^{\text{SOZ}}$) for each seizure and calculated a Flow Index (FI) as below (Fig. 5-1(a2), Fig. 5-1(b2)).

$$FI = \frac{D_{OUT} - D_{IN}}{D_{OUT} + D_{IN}} \quad (5-2)$$

FI varies between -1 and 1. A leading region is expected to have more outgoing links than ingoing links. Therefore, positive FI means that the SOZ region serves as a driver and negative FI means that the SOZ is driven by the surrounding regions (NonSOZ).

Table 5-1 Summary of the patients' clinical characteristics. IFG = inferior frontal gyrus; ITG = inferior temporal gyrus; STG = superior temporal gyrus, IPL = inferior parietal lobule, SMA = supplementary motor area, Ins = insular, OF = orbitofrontal, FUS = focal unaware seizure, FAS = focal aware seizure, ES = electrical seizure.

Patient ID	Sex	Electrode types	Location of interictal activity	Location of seizure onset	Seizure type	MRI	Engel class	# of seizures	# of channels	Average seizure duration (Sec)
S1	M	Grid/strips and depths	R precuneus > R lat T	R precuneus	ES + FUS + 2nd	Negative	I	11	97	30.06
S2	F	Grid/strips and depths	R post-CG > L mesial T > R mesial T	R post-CG, pre-CG, pINS >> L mesial T	FUS + ES	Negative	I	6	104	20.96
S3	F	Grid/Strips and depths	L (ant ins, IFG, ant STG)	L (ant ins, ant STG)	FUS	Negative	I	10	61	51.72
S4	F	Grid/strips and depths	R IFG > R orbito-F > R ant lat T > R MFG	R IFG > R orbito-F > R ant lat T	FUS + ES	Negative	I	5	82	21.84
S5	M	Grid/Strips/Depths	R IFG, R OF, R med FG/SMA	Non localizing	FUS + ES	Negative	I	6	91	42.34
S6	M	Grid/strips and depths	L Pop-pINS	L Pop-INS	FUS + ES	Negative	I	4	90	112.63
S7	F	Grid/strips	L post-central and precentral gyrus	Left pre-central and post-central gyrus	FIAS, FAS, ES	Negative	I	4	73	63.66
S8	M	Grid/ strips and depths	L Fp, or L SFG, or L mT, or L mid-Ins, or L IFG	L mT, or L Fp, or L F op	FIAS, FAS, ES	Negative	I	4	110	95.54
S9	M	Strips and depths	[R OF + R IFG +/- R ant Ins], or [R Fp +/- R OF], or R mT, or R ant Ins	R OF +/- post ITG	FIAS	Dysembryo plastic neuroepithelial tumor	I	5	106	190.61
S10	M	Grid/strips and depth	R Ant Lat T, R lingual gyrus, R mT, R F op, R MTG, R ITG	R Ant Lat T, R ITG	FIAS	Negative	I	4	105	86.25
S11	F	Grids/ strips and depths	IPL, heterotopia nodule, cuneus, Post Lat T	IPL, heterotopia nodule, cuneus	FAS + + +, FIAS	Heterotopia (both periventricular H., and band H.), FCD	I	3	113	35.84
S12	F	Grid/strips and depths	L ins + m-T (+ + +)	L ins + m-T (+ + +)	FAS + FUS	Negative	II	5	102	74.82

S13	F	Grid/ strips and depths	L Ant Ins, L F op, post OF, L sub-T	L Ant Ins + L IFG	FIAS	Negative	II	4	105	113.16
			R Ant T, R Ant Ins, R						5	101
S14	M	Grid/ strips and depths	MFG, R IFG, R OF, R Fp	R Ant T, R Ant Ins	FAS, FIAS, Absences	Negative	II			
S15	M	Grid/ strips and depth	R Fp, R OF, R MFG, R Ant cingulum, R IFG	R Fp, ROF	FAS, FIAS	Negative	II	5	114	20.75
				L Ant Lat T + L					3	113
S16	M	Grid/ strips and depths	LmT, L OF, L Ant Ins, L MTG, L SFG, L parieto-occipital junction, L IPL	L SFG + L MFG + L IFG + L IPL + L parieto-occipital junction	FIAS + FBTCs	Negative	II			
S17	M	Grid, strips and depth	L Ant Ins, L middle Ins, L mT, L IFG, L OF? L Ant cingulum	L [OF + IFG + Ant Ins]	ES, FAS, FIAS, FBTCs	FCD	II	5	111	64.18
S18	F	Grid/ strips and depths	L mT, L ITG, L MTG, L STG, heterotopia nodule	L temporo-parietal junction and heterotopia nodule	FAS, FIAS	Periventricular heterotopia	II	3	99	102.93
S19	M	Strips and depths	L mT, L Ant Ins, L MTG, R mT, R ant Ins	Dozens L mT +++ (only one R mT)	ES, FAS	Mild R temporal atrophy	II	5	106	37.22
S20	F	Grid/ strips and depths	L mT, L Ins, L T-occipital junction, L mesial occipital, R mT	R mT, R mesial occipital, R lat T, L mT	FAS, FIAS	Mild R hippocampus atrophy	II	6	116	67.83

5.2.4.4 Statistical methods

One-way ANOVA was performed to compare FI between different pattern groups and post-hoc analysis using the Tukey-Kramer test was performed to control for the family-wise error rate of 5% (FWER = 5%). The relationship between seizure onset and termination patterns was investigated using the Cross-Tabulation method and chi-square test (if the p-value<0.05, the patterns are associated).

5.3 Results

In this study, IEEG recordings of 103 seizures from 20 patients (aged between 18 and 49 years old) were analyzed. Their clinical information, as well as EEG recording findings, are presented in Table 5-1. As reported in Table 5-1, in this study, different sensor types (i.e., grids, strips and depth electrodes) have been used and the association between these different implantation approaches and the onset patterns as well as the calculated functional connectivity measures are discussed in Appendix B (Figs. B1-B3).

5.3.1 Seizure onset and termination patterns

We identified nine different seizure onset patterns. 65% of patients (13 patients) had the same onset pattern across their recorded seizures and 35% of them (7 patients) had two onset patterns. The various categories and terminology used for these onset patterns were loosely based on the works of [59,60] (Fig. 5-2(a)-5-2(i)):

- 1) Low Voltage Fast Activity (LVFA): the initial amplitude of this rhythmic activity is lower than $30\mu\text{V}$ and the frequency is greater than 13Hz (Fig. 5-2(a)).
- 2) LVFA superimposed on a slow wave: the onset begins with LVFA superimposed on a single slow wave (Fig. 5-2(b)).
- 3) High Amplitude Fast Activity (HAFA): the frequency and amplitude are respectively greater than 13Hz and $30\mu\text{V}$ (Fig. 5-2(c)).
- 4) Low Frequency High Amplitude (LFHA): slow rhythmic sharp spikes (0.5–2 Hz) with high amplitude ($>30\text{mV}$) (Fig. 5-2(d)).
- 5) Rhythmic Spike/PolySpike and Wave (rSW/rPSW): slow spike-and-wave/polyspike-and-wave complexes with a frequency of 2-4 Hz (Fig. 5-2(e)).
- 6) rSW followed by LVFA: rSW complexes followed by LVFA (Fig. 5-2(f)).
- 7) Delta rhythmic activity: rhythmic activity in the frequency range of delta band ($<4\text{Hz}$) with high amplitude ($>30\text{mV}$) (Fig. 5-2(g)).
- 8) Rhythmic θ/α : rhythmic high amplitude ($>30\text{mV}$) activity in the frequency range of θ/α activity (4-13Hz) (Fig. 5-2(h)).
- 9) Delta brush: rhythmic activity with high frequency (20-30Hz) superimposed on rhythmic delta activity ($<4\text{Hz}$) (Fig. 5-2(i)).

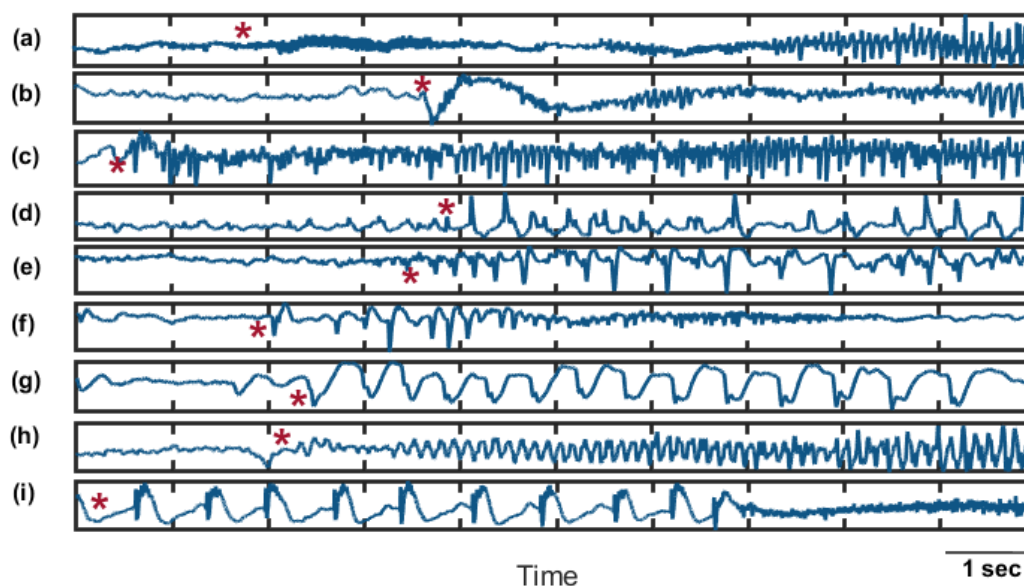


Figure 5-2 Nine seizure onset patterns: a) Low Voltage Fast Activity (LVFA) recorded with an electrode located within the SOZ (Left superior temporal gyrus) of a patient with Engel-I surgery outcome, b) LVFA on a wave recorded with an electrode located within the SOZ (right inferior frontal gyrus) of a patient with Engel-I surgery outcome, c) High Amplitude Fast Activity (HAFA) recorded with an electrode located within the SOZ (insular) of a patient with Engel-I surgery outcome, d) Low Frequency High Amplitude (LFHA) recorded with an electrode located within the SOZ (left temporo-parietal junction) of a patient with Engel-II surgery outcome, e) rhythmic Spike/PolySpike and Wave (rSW/rPSW) recorded with an electrode located within the SOZ (left anterior insular) of a patient with Engel-II surgery outcome, f) rSW followed by LVFA recorded with an electrode located within the SOZ (left pre-central gyrus) of a patient with Engel-I surgery outcome, g) delta rhythmic activity recorded with an electrode located within the SOZ (Left insular) of a patient with Engel-II surgery outcome, h) rhythmic θ/α recorded with an electrode located within the SOZ (right orbitofrontal) of a patient with Engel-I surgery outcome, i) delta brush recorded with an electrode located within the SOZ (left mesial temporal) of a patient with Engel-I surgery outcome. The stars depict seizure onset time.

We detected six different seizure termination patterns, as suggested by the terminology presented in the literature [59,294] (Fig. 5-3(a)-5-3(g)). Our results indicate that 60% of patients (12 patients) had one termination pattern across their ictal recordings and 35% (7 patients) had two patterns while for only 5% (1 patients) we observed three termination patterns:

- 1) Rhythmic Spike/PolySpike and Wave (rSW/rPSW): slow spike-and-wave or polyspike and wave complexes with a frequency between 2-4 Hz (Fig. 5-3(a)),
- 2) High Amplitude Fast Activity (HAFA): high frequency ($>13\text{Hz}$) rhythmic activity with high amplitude ($>30\text{mV}$) (Fig. 5-3(b)),

- 3) rhythmic θ/α : rhythmic activity in the frequency range of θ/α activity (4-13Hz) with high amplitude ($>30\text{mV}$) (Fig. 5-3(c)),
- 4) Rhythmic spikes: sharp fast spikes of high frequency ($>13\text{Hz}$) (Fig. 5-3(d)),
- 5) Burst Suppression (BS): rhythmic spikes alternating with brief periods of voltage suppression/attenuation (Fig. 5-3(e)),
- 6) Delta brush: rhythmic activity with high frequency (20-30Hz) superimposed on rhythmic delta activity ($<4\text{Hz}$) (Fig. 5-3(f)).

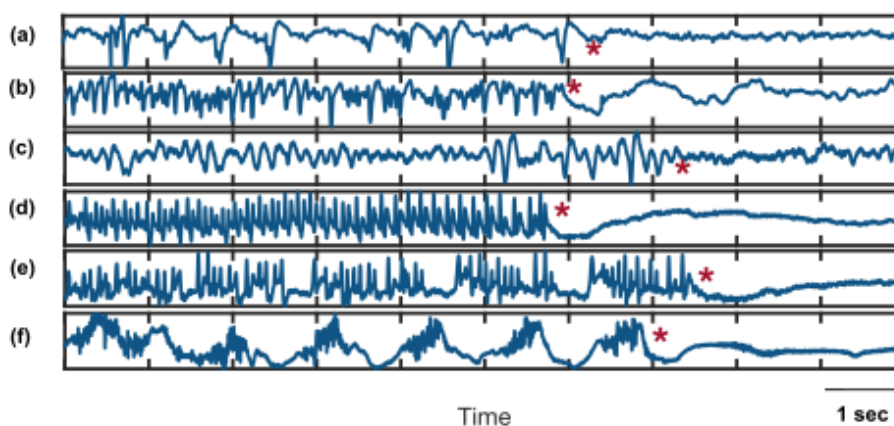


Figure 5-3 Six seizure termination patterns: a) rhythmic Spike and Wave (rSW/rPSW), b) High Amplitude Fast Activity (HAFA), c) rhythmic θ/α , d) rhythmic spikes, e) Burst Suppression (BS), f) delta brush. The stars depict seizure termination time.

5.3.2 Pattern distributions and their associations

We observed fast activity ($>13\text{Hz}$) for 56% of the onset patterns, of which 19% was with high and 36% with low amplitude. After the fast activity onset patterns, the next prevalent pattern was rSW/rPSW (18%) (Fig. 5-4(a)).

As shown in Fig. 5-4(b), 44% of seizures terminated with BS termination pattern, and 39% of seizures had rSW/rPSW patterns before their termination.

The cross-tabulation analysis showed a significant association between seizure onset and termination patterns (Chi-square=80.43 $p=0.0023$). As presented in Fig. 5-5, all the seizures (14 seizures) with fast activity termination patterns ($>13\text{Hz}$) -rhythmic spikes and HAFA- had a type of fast activity (LVFA, LVFA on a wave, HAFA) at seizure onset as well. The rSW/rPSW

termination pattern was observed with all onset patterns except for the rhythmic delta onset pattern. Except for the delta brush onset pattern, the BS termination pattern was observed with all onset patterns.

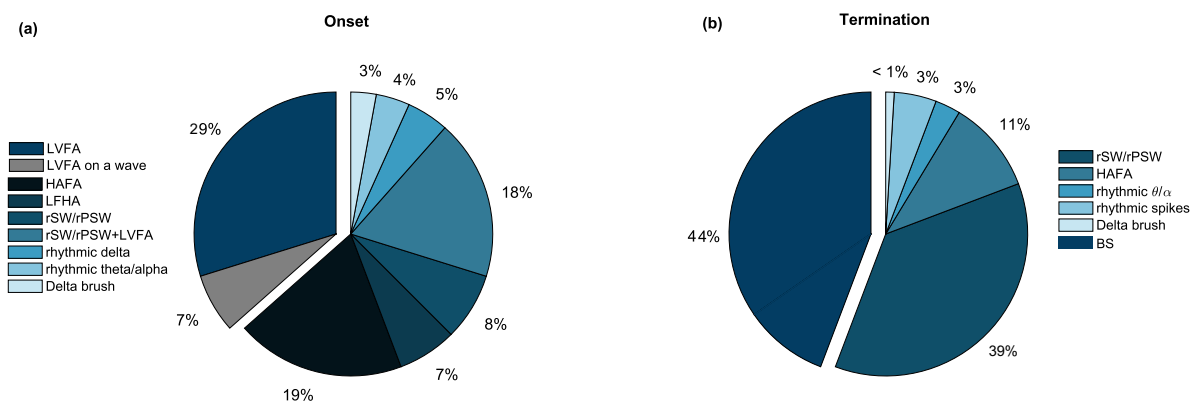


Figure 5-4 Pie chart representing the prevalence of nine seizure onset and seven seizure termination patterns. The sliced region in (a) shows the percentage of all onset patterns starting with Low Voltage Fast Activity (LVFA) and the sliced region in (b) represents the percentages of all termination patterns with Burst Suppression (BS) pattern.

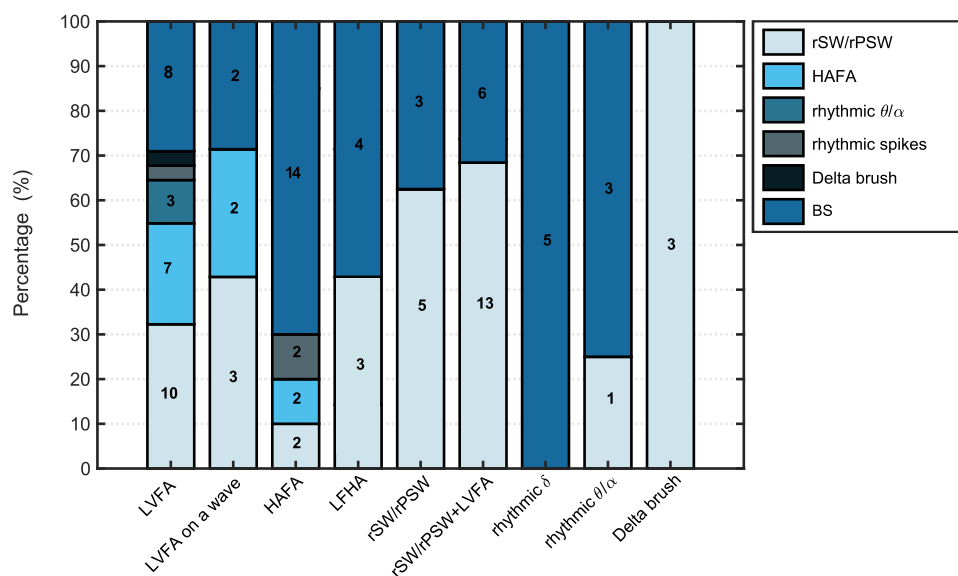


Figure 5-5 Histogram depicting the percentage of each seizure termination patterns for each seizure onset pattern. Numbers indicate the number of seizures per subgroup.

The histograms in Fig. 5-6 display the repartition of termination zones (*In*, *Out*, *In-Out*, *Diffuse*) according to seizure onset and termination patterns. As shown in Fig. 5-6(a), the LVFA (delineated

by dash lines) are more prevalent when the termination region is less distributed. More specifically, the percentage of seizures with LVFA for ‘In’, ‘Out’, ‘In-Out’, and ‘Diffuse’ classes are in descending order with respectively 62, 44, 31, and 23 percent.

The rSW/rPSW and BS termination patterns were observed for all termination regions, but the fast activity termination patterns (>13Hz) were more common among seizures terminating within the same region as the SOZ (78% of seizures with fast termination pattern were classified as ‘In’ (Fig. 5-6(b)).

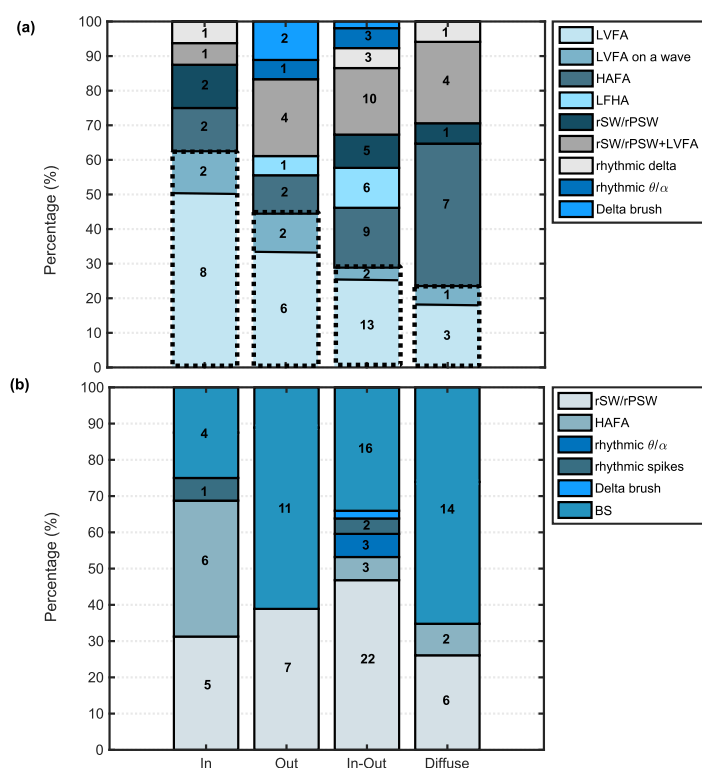


Figure 5-6 Histogram showing the percentage of each (a) seizure onset and (b) seizure termination patterns for all termination region categories (In, Out, In-Out, Diffuse). Numbers indicate the number of seizures per subgroup.

5.3.3 The Flow Index and seizure patterns

We reclassified the seizure onset patterns into two groups [59]: The fast onset group (corresponding to LVFA and LVFA on a wave and HAFa onset patterns) and the slow onset group (corresponding to rSW/rPSW, delta rhythmic activity, LFHA, rhythmic θ/α onset patterns) (Fig. 5-1). For seizures in each group, we calculated the flow index, FI, prior to seizure onset (1-min preictal period). We

observed higher averaged FIs for the slow onset group compared to the fast group; however, this difference was only significant within gamma ($p<0.001$) and high gamma ($p<0.05$) frequency bands. Further, within these frequency bands, FIs for the fast onset group were mainly negative as opposed to the slow onset group (Fig. 5-7).

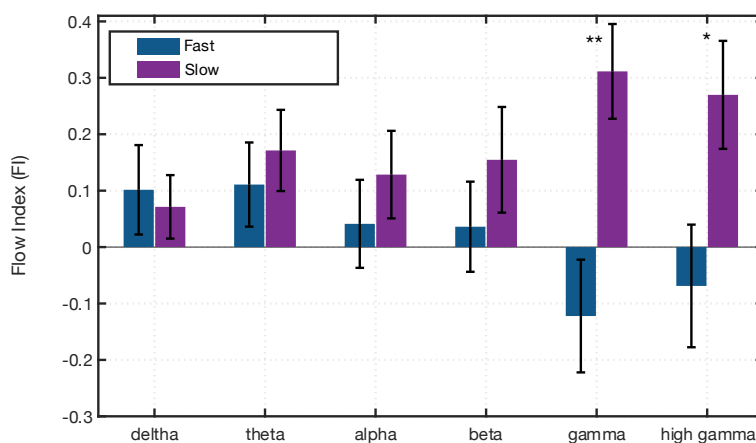


Figure 5-7 Calculated Flow Index (FI) of the recordings prior to two seizure onset groups: fast and slow. Fast group includes seizures with LVFA, LVFA on a wave and HAFA onset patterns and slow group includes the rSW/rPSW, delta rhythmic activity, LFHA, rhythmic θ/α onset patterns. The lines show 95% confidence intervals. Single star denotes significant results with p -value <0.05 and double star shows significant results with p -value <0.001 .

5.4 Discussion

After identifying nine seizure onset and six seizure termination patterns based on the suggested repertoire of human ictal activity [59,60,285], we detected an association between some onset and termination patterns; however, our results indicated that seizures with almost any onset pattern could terminate through common termination patterns. These findings suggest that common termination mechanisms could end seizures regardless of the mechanisms that generated them. More precisely, we noticed that all seizures with fast ($>13\text{Hz}$) termination patterns (either with HAFA or rhythmic spikes) had a fast ($>13\text{Hz}$) onset pattern type (LVFA, LVFA on a wave or HAFA); nonetheless seizures with almost any onset pattern could terminate through the Burst Suppression (BS) and rhythmic Spike/PolySpike and Wave (rSW/rPSW) termination patterns (Fig. 5-5). Distinct neuronal and synaptic mechanisms have been reported to be predominantly involved in the generation of these different patterns of ictal activity [175,202]. For instance, using in vitro

optogenetic experimental settings, it has been reported that seizures with LVF onset are generated due to the involvement of hyperpolarizing inhibitory events while the generation of seizures with hypersynchronous onset depends on impairment of inhibition and enhanced excitation [175,202]. BS termination pattern has been suggested to be the result of simultaneous increased inhibition and excitation [295,296] and involvement of the thalamocortical circuit [297] and the leading role of thalamic outputs in driving higher thalamocortical synchronization is reported in the generation of rSW/rPSW seizure termination pattern [289].

On the spatial scale, we found that low voltage fast ($>13\text{Hz}$) onset patterns (LVFA, LVFA on a wave) as well as the fast ($>13\text{Hz}$) termination patterns (HAFA, rhythmic spikes) were more prevalent among seizures terminating within their onset region (*In*) compared to seizures terminating in more distributed regions (*In-Out*, *Diffuse*) (Fig. 5-6). While our results demonstrates consistency with studies reporting a critical role for fast onset oscillations to hamper the propagation of ictal activity [214], it suggests self-sufficiency of the regions involved in the generation of fast onset patterns to terminate the ictal activity. In contrast, the BS termination pattern (the most prevalent one) was more frequently observed when the termination region was further distributed than the onset zone (Fig. 5-6) which would suggest the involvement of a larger region compared to the onset zone. These findings are in agreement with studies reporting the emergence of burst suppression pattern when more diffuse cortical areas are recruited as a result of receiving projections from subcortical structures (e.g., [295,298]).

By extending our investigation of seizure onset patterns and calculating a directed frequency-dependent measure, PSI, our findings further indicate the existence of different driver regions prior to the generation of seizures with distinct onset patterns. More specifically, our results show a significantly higher inflow to the SOZ from NonSOZ channels in the gamma ($p<0.001$) and higher gamma ($p<0.05$) frequency bands prior to seizures in the fast onset group compared to seizures from the slow onset group. Since different frequencies of neural oscillations are associated with different neural mechanisms [48,299], we preferred a frequency domain method with its information content restricted to specific frequency bands. High-frequency activities (gamma, high gamma) have been suggested to represent the inhibitory postsynaptic potentials (IPSPs) and would be generated due to the synchronous activity of interneurons [300]. This proposal is supported by experimental and theoretical works showing GABA mediated inhibition to be a key ingredient of higher frequency activities [48,299,301–303]. Therefore, by exhibiting the inflow to the SOZ of

seizures with fast onset patterns in high-frequency ranges, our findings underscore a stronger involvement of inhibitory input to the SOZ from NonSOZ in generation of fast activity onset patterns compared to the slow onset patterns. These results are in concordance with studies reproducing these patterns in experimental models of epilepsy using differently impairing excitation and inhibition mechanisms [175,202]. Accurately, using an acute model of temporal lobe ictogenesis, previous studies reported a correlation between the fast activity at the onset of focal seizures and the sustained inhibitory activity of GABAergic interneurons [209].

One limitation of our study is that the etiologic spectrum of our patients might not be representative of all underlying etiology of patients with drug-resistant epilepsy. This limitation could partly be explained by the fact that certain epileptogenic lesions (e.g., hippocampal sclerosis, focal cortical dysplasia type 2, cavernoma, certain benign tumors) can benefit from direct surgery (without a prior intracranial EEG study) due to advances in noninvasive investigative techniques. Additionally, because of our inclusion criteria, we only studied patients with successful surgical outcome which might have further restricted our database.

5.5 Conclusion

By analyzing different seizure onset and termination patterns, we showed the distribution of these patterns and investigated their association. Although some termination patterns were identified to occur exclusively in seizures with specific onset patterns, we found that seizures of almost all onset patterns could terminate through common termination patterns: notably, the BS and rSW/rPSW termination patterns. We further explored the recordings during their transition from interictal to various onset patterns using a directed functional connectivity measure and detected a higher inflow to the SOZ from NonSOZ in high frequency ranges for seizures with fast onset activity compared to seizures with slow onset patterns.

Acknowledgements

This research was supported by CIHR project grant (390044); Canada Research Chair Program (DKN).

Conflict of interest

None of the authors has any conflict of interest to disclose.

CHAPTER 6 ARTICLE 3: COMPUTATIONAL MODELING OF SEIZURE ONSET PATTERNS TO UNDERPIN THEIR UNDERLYING MECHANISMS

Leila Abrishami Shokooh^{1,2,*}, Frédéric Lesage^{1,3}, Dang Khoa Nguyen^{2,4}

¹ École Polytechnique de Montréal, Université de Montréal, C.P. 6079, succ. Centre-Ville, Montreal, H3C 3A7, Canada

² Centre de Recherche du Centre Hospitalier de l'Université de Montreal (CHUM), Montreal, QC, Canada

³ Research Centre, Montreal Heart Institute, Montreal, Canada

⁴ Neurology Division, Centre Hospitalier de l'Université de Montréal (CHUM), 1000 Saint-Denis, Montreal, H2X 0C1, Canada

* Correspondence to Leila Abrishami Shokooh, École Polytechnique, Université de Montréal, C.P. 6079 succ. Centre-Ville, Montreal, H3C 3A7; e-mail: Leila.abrishami-shokooh@polymtl.ca

This article has been submitted to the Journal of Neural Engineering, July 2021.

Abstract

In the study of epilepsy, it is of crucial importance to understand the transition from interictal into ictal activities (ictogenesis). Different mechanisms have been suggested for the generation of ictal activity; yet, it remains unclear whether different physiological mechanisms underly different seizure onset patterns. Herein, by implementing a computational model that takes into account some of the most relevant physiological events (e.g., depolarization block, collapse, and recovery of inhibitory activities) and different scenarios of imbalanced excitatory-inhibitory activities, we explored if seizures with different onset patterns stem from different underlying mechanisms. Our model revealed that depending on the excitation level, seizures could be generated due to both enhancement and collapse of inhibition for specific range of parameters. Successfully reproducing some of the commonly observed seizure onset patterns, our findings indicated that different onset patterns can arise from different underlying mechanisms.

Significance Statement

Various seizure onset patterns have been reported; however, it yet remains unknown whether seizures with distinct onset patterns originate from different underlying mechanisms. The common belief on seizure generation focuses on the imbalance between synaptic excitation and inhibition which has led to the identification of distinct and, in some cases, even contradictory mechanisms for seizure initiation. In this study, by incorporating some of these various physiological mechanisms in a unified framework, we reproduced some commonly observed seizure onset

patterns. Our results suggest the existence of different mechanisms responsible for the generation of seizures with distinct onset patterns which can enhance our understanding of seizure generation mechanisms with significant implications on developing therapeutic measures in seizure control.

6.1 Introduction

Epilepsy, second only to stroke, is one of the most common chronic neurological disorders. It affects 50 million people worldwide [17] and is characterized by recurrent spontaneous seizures, i.e., sudden transient behavioral disturbances due to abnormal excessive neural discharges [15]. About 30% of patients have drug-resistant epilepsy [304–306] which could be due to the diverse network and cellular mechanisms responsible for seizure generation [34].

Variable electrophysiological features have been reported for seizures in intracranial EEG studies which has resulted in the definition of specific patterns for seizure onset [59,60]. Some onset patterns have been associated with the activity of specific brain regions [61,63,161] and synaptic mechanisms [175,202]. For instance, using an in vitro optogenetic experimental setting, it has been reported that seizures with Low Voltage Fast Activity (LVFA) onset are generated due to the involvement of hyperpolarizing inhibitory events while the generation of seizures with hypersynchronous onset depends on enhanced excitation [175,202]. These findings raise the question as to whether distinct onset patterns of ictal activity arise from fundamentally different mechanisms.

The mechanisms underlying seizure generation involve the interaction of many complex cellular and synaptic components [227,228] which could govern the emergence of distinct iEEG ictal patterns [62,221,307]. Studying the imbalance between synaptic excitation and inhibition has been the main focus of the research on ictogenesis [71,170,173–177]. It was commonly believed that abnormally enhanced glutamatergic excitation and collapse of GABAergic inhibition were pro-epileptic and the main driver for seizure generation, whereas the increased GABAergic activity was viewed to protect against seizure generation [4–7]. However, this notion might require reconsideration in light of more recent clinical and experimental data that have offered evidence for the critical role of the GABAergic network in focal seizures. More specifically, some studies have reported enhancement of inhibitory activity before and at the very onset of ictal activity [8,10,11,13,14], casting doubt on the suggested role for the collapse of inhibition in seizure generation. In summary, distinct and even contradictory mechanisms have been suggested to

underly seizure initiation. Incorporating these distinct mechanisms in a unified framework would enable us to compare the impact of these different mechanisms in seizure generation and would aid in providing an insight into whether different underlying mechanisms could lead to seizures with different onset patterns.

In the study of epilepsy, the computational approach has been widely utilized in order to provide a mechanistic insight into mechanisms responsible for seizure generation [75,76]. In general, there are two main approaches in constructing mathematical models of ictal activity: biophysically realistic models and phenomenological models. Biophysically realistic modeling approaches rely on detailed cellular and synaptic mechanisms which lead to highly parameterized and complicated models [78–82]. On the other hand, phenomenological models describe the dynamic without reference to mechanisms and are generally more tractable and computationally less expensive [107,110]. These models, while being straightforward in implementation, do not have a physiological equivalent in their elements. Therefore, using phenomenological models, findings are disconnected from physiological phenomena, rendering interpretation more limited when designing therapeutic measures. More recently a hybrid approach has been introduced that combines both biophysically realistic and phenomenological models and is aimed at capturing the benefits of these two approaches through the incorporation of the relevant biophysical features into a simple framework [111].

To investigate the underlying mechanisms for generation of some of the most common patterns of ictal activity, we adopted the hybrid modeling approach. By constructing a neural mass model and, updating, expanding, and exploring a well-established framework [112,308], we generated different patterns of seizure generation. More specifically, we considered different scenarios of disturbed balance between excitatory and inhibitory activities and identified a range of parameters producing distinct onset patterns providing interpretation in terms of underlying physiological mechanisms. The model successfully reproduced a number of commonly observed onset patterns including Low Voltage Fast Activity (LVFA), spindles of alpha/beta, rhythmic Spike and Wave (rSW/rPSW), burst suppression, High Amplitude Fast Activity (HAFA) and rhythmic spikes/sharp waves. The results, collectively, point toward more complicated scenarios for seizure generation than simple excessive excitation and insufficient inhibition and suggest that different seizure onset patterns can arise from different cellular and synaptic mechanisms.

6.2 Materials and Methods

Intracranial electroencephalogram

In a previous work [309], approved by the Centre Hospitalier de l'Université de Montréal (CHUM) Ethics Committee, we reviewed 103 iEEG ictal recordings using intracranial EEG electrodes (128-channel recording system, Harmonie, Stellate, Montreal, Canada, 2000Hz sampling rate) from 20 patients with drug-resistant focal epilepsy who were candidates for resective surgery and, identified nine common seizure onset patterns [59,60]. In the current study, we used some of those seizure onset classes to validate and classify our model simulations.

Computational model

In this study we used a well-established coupled neuronal population model, the Jansen model [251], and expanded it with some relevant biophysical features. We incorporated the slow and fast inhibitory mechanisms as suggested by Wendling et al. [112] to respectively account for the dendrite and soma targeting inhibitory interneurons. As presented in Fig.6-1a, the model consists of four components: the pyramidal cells (PYR), the excitatory interneurons (E), the slow dendrite targeting inhibitory interneurons (I_D) and the fast soma targeting inhibitory interneurons (I_S). The postsynaptic activity of the pyramidal cells (the main excitatory component) is considered as the model output to simulate the ictal iEEG recordings.

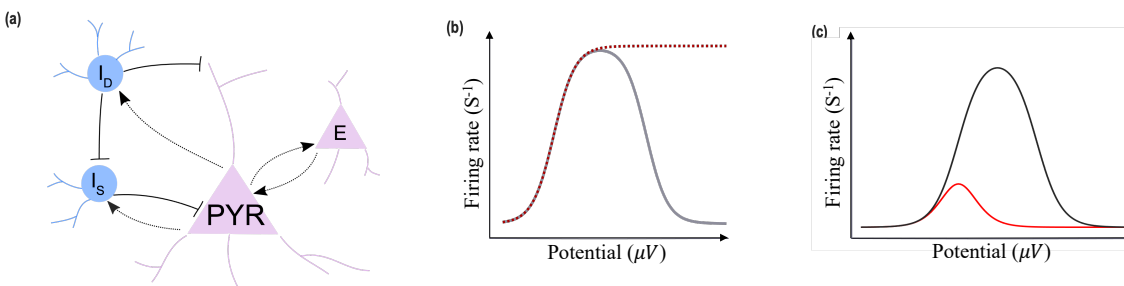


Figure 6-1 Excitatory inhibitory neuronal population model and the activation functions. (a) The neuronal population model which is composed of excitatory and inhibitory components: pyramidal cells (PYR), excitatory interneurons (E), dendrite targeting inhibitory interneurons (I_D) and soma targeting inhibitory interneurons (I_S). (b) The nonlinear activation function of a neural population that relates the average postsynaptic potential to an average firing rate for that population. The dotted black curve represents the commonly used sigmoid function and the solid black curve shows the activation function we used which considers depolarization block. (c) Decreasing the depolarization block threshold for the inhibitory populations. In this figure, the red activation function has a lower depolarization block threshold ($\theta = 0$) compared to the black activation function ($\theta = 4$).

In this approach the average postsynaptic potential of each neural population is modeled by two main parts: 1) an activation function that describes a nonlinear relationship between the neural population's average postsynaptic potentials and its output firing rate and 2) a linear transfer function, $h(t) = \frac{Wt}{\tau_w} e^{-\frac{t}{\tau_w}}$, that transforms the input firing rate into average postsynaptic potential.

In this equation, W and τ_w respectively represent the average synaptic gain and average synaptic time delays for each neural population. The model can be expressed as a system of coupled second-order differential equations as presented in Eq.6-1 [112] and Appendix C provides more details regarding formulating these equations and their association with Fig. 6-1a.

$$\begin{cases} \ddot{y}_1(t) = AaF_e[y_2(t), y_3(t), y_4(t)] - 2a\dot{y}_1(t) - a^2y_1(t) \\ \ddot{y}_2(t) = Aa\{P(t) + C_2F_e[C_1y_1(t), 0, 0]\} - 2a\dot{y}_2(t) - a^2y_2(t) \\ \ddot{y}_3(t) = BbC_4F_s[C_3y_1(t), 0, 0] - 2b\dot{y}_3(t) - b^2y_3(t) \\ \ddot{y}_4(t) = GgC_7F_d[C_5y_1(t), C_6y_5(t), 0] - 2g\dot{y}_4(t) - g^2y_4(t) \\ \ddot{y}_5(t) = BbF_s[C_3y_1(t), 0, 0] - 2b\dot{y}_5(t) - b^2y_5(t) \end{cases} \quad (6-1)$$

$$F_j(E, I_D, I_S) = \frac{2e_0}{1+e^{-\frac{(E-(v_j+I_D+I_S))}{r_j}}} * \frac{1}{1+e^{-\frac{(E-(v_j+I_D+I_S)-\theta_j)}{r_j}}} \quad (6-2)$$

where A , B and G represent the synaptic gains of respectively the excitatory, dendrite targeting inhibitory interneurons and soma targeting inhibitory interneurons. $P(t)$ describes inputs from other regions which are modeled as Gaussian white noise similar to the original model [251]. Parameters C_1 to C_7 are the connectivity constants which represent the average number of synaptic contacts (Table 6-1). In Eq.6-2, F_j where $j \in \{e, s, d\}$, represents the activation function for the excitatory population when $j = e$ and for dendrite and soma targeting inhibitory interneurons when respectively $j = d$ and $j = s$. The variable θ_j represents the depolarization block threshold for dendrite targeting and soma targeting inhibitory interneurons respectively when $j = d$ and $j = s$.

Usually, the activation function is assumed to follow a sigmoid-shaped function; however, more recent studies suggest a bell-shaped activation function which considers depolarization block [310–

312]. An activity-driven depolarization block is suggested to be a rate-limiting mechanism to protect cells from excessive firing and can be due to synaptic resources or energy depletion during high levels of activity [311]. Accordingly, in this study, we replaced the commonly used sigmoid function of the original model with the firing rate function in Eq.6-2 to account for the effect of depolarization block in our model (Fig.6-1b) [312].

A second mechanism that was incorporated in the model was the collapse and recovery of the inhibitory activity. Some studies have reported seizure initiation due to the failure of inhibition with an important role for the depolarization block of inhibitory cells [7,313–316]. On the other hand, there is experimental evidence for the enhancement of inhibition before and at the very onset of seizure, contradicting the widely accepted paradigm on inhibitory failure mechanisms [8–14]. To explore both scenarios, we further expanded the model by considering variable depolarization block threshold for the activation function of the inhibitory populations (i.e., θ_s , θ_d in Eq.6-2) (Fig.6-1c).

Table 6-1 The model parameters used in Eq.6-1 and Eq.6-2.

Parameter	Value
τ_e	0.01 s
τ_d	0.02 s
τ_s	0.002 s
C	135
C_1, \dots, C_7	$C_1 = C, C_2 = 0.8C$ $C_3 = C_4 = 0.25C$ $C_5 = 0.3C, C_6 = 0.1C$ $C_7 = 0.8C$
e_0	$2.5 S^{-1}$
v_0, r_0	6 mV, 1.7 mV
v_{0i}, r_i	3 mV, 0.6 mV
θ_e	15
θ_s, θ_d	0 or 4 (Table 6-2)

In all simulations, the depolarization block threshold of the excitatory populations was set to 15 (i.e., $\theta_e=15$) which was chosen to adjust the excitatory activation function to have the same slope at half activation as the sigmoid function used by Jansen et al. [251] in their original model (Table 6-1). Inhibitory neurons due to their limited size become activated for smaller inputs and reach their depolarization block with a faster dynamic compared to the large pyramidal cells [310]. In order to consider these differences between the excitatory and inhibitory populations in our model,

we modified parameters r_i and v_i as presented in Table 6-1 and chose θ_d and θ_s value to be 4 so that it would have the same slope at half activation as a sigmoid function with parameters r_i and v_i . However, wherever we intended to explore the effect of the collapse of an inhibitory population, we reduced the depolarization block threshold of that inhibitory population to zero (i.e., θ_d, θ_s). Fig.6-1c depicts the activation function of the inhibitory populations for both depolarization block threshold values equal to 0 and 4 with respectively the red and black curves.

To account for different scenarios of disturbed balance between excitation and inhibition, we used a stochastic approach. In short, the model parameters for excitatory and inhibit synaptic gains (A , B and G) were divided into one-unit intervals and randomly sampled within each interval. Then, for each interval of the parameters, the most probable pattern of activity was identified. In the next step, starting from the range of A , B and G parameters, which generated background activity, we examined if the collapse and recovery of the inhibitory activity, which respectively were modeled through decreasing and increasing the parameters θ_d and θ_s , could result in the emergence of different seizure onset patterns. For the parameter A , we considered a range of values that varied from very low excitation levels to values inducing depolarization block in the excitatory population and explored the effect of different inhibitory modulations in transforming the background activity into ictal patterns; we did not explore “A” values beyond this level.

6.3 Results

We first validated our model by producing some of the commonly observed patterns of ictal activity. Using Eq.6-1 and Eq.6-2 for fixed values of θ_e , θ_d and θ_s and only by varying the synaptic gains A , B , and G , we could generate six ictal patterns observed in iEEG recordings as described below (Fig.6-2):

- 1) Low Voltage Fast Activity (LVFA): the initial amplitude is lower than $30\mu\text{V}$ with the frequency range of γ activity (Fig. 6-2(b)),
- 2) Rhythmic spike/sharp waves: rhythmic spikes with the duration of 20ms to 70ms or sharp waves (duration of 70-200ms); because of the discernable similarity between these two patterns, we merged these two patterns in a single group to simplify our classification (Fig. 6-2(c)),
- 3) Rhythmic Spike and Wave (rSW): spike and slow wave complexes with the frequency ranging between 2 and 4 Hz (Fig. 6-2(d)),

- 4) High Amplitude Fast Activity (HAFA): the frequency is greater than 13 Hz and amplitude higher 30 μV (Fig. 6-2(e)),
- 5) Rhythmic α/β : rhythmic activity in the frequency range of α/β activity (Fig. 6-2(f)),
- 6) Burst suppression: burst of rhythmic spikes interrupted with brief periods of voltage suppression/attenuation (Fig. 6-3(g)).

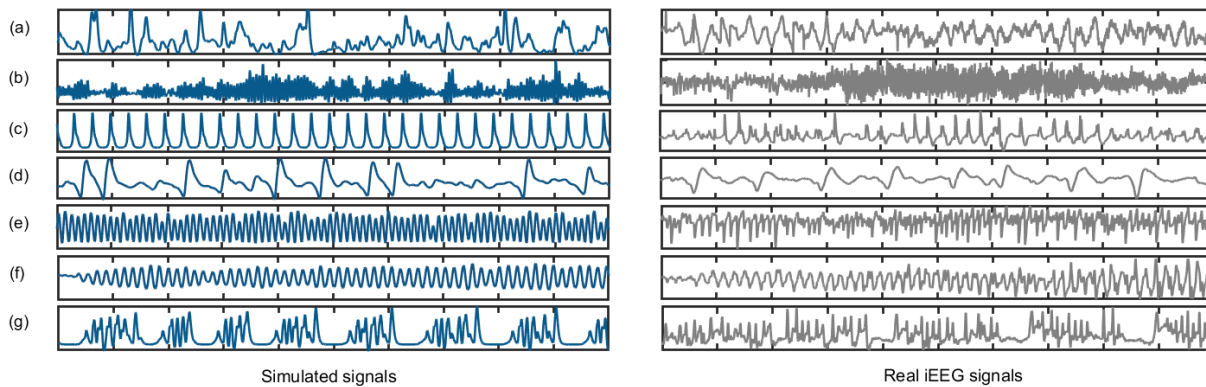


Figure 6-2 Model simulations vs. real iEEG ictal recordings. The signals in blue are the simulated signals produced by our computational model and the signals in grey are the real depth iEEG recordings for (a) background, (b) Low Voltage Fast Activity (LVFA), (c) rhythmic slow spikes/sharp waves, (d) rhythmic Spike and Wave (rSW), (e) High Amplitude Fast Activity (HAFA), (f) rhythmic α/β and (g) burst suppression ictal activities.

To identify the range of parameters producing each activity pattern, we first divided the range of synaptic gains A , B and G into one-unit intervals. Then, taking the Monte Carlo approach, we drew 100 random values for A , B and G within each interval and ran the simulations for both low and high values of depolarization block threshold of inhibitory populations (θ_d , θ_s). In the next step, based on the time and frequency domain features of each simulated signal we classified them into six distinct activity patterns that the model could generate as displayed in Fig.6-2. We finally identified the range of parameters A , B and G that generated each pattern of activity for both low and high values of θ_d and θ_s (Fig.6-3)

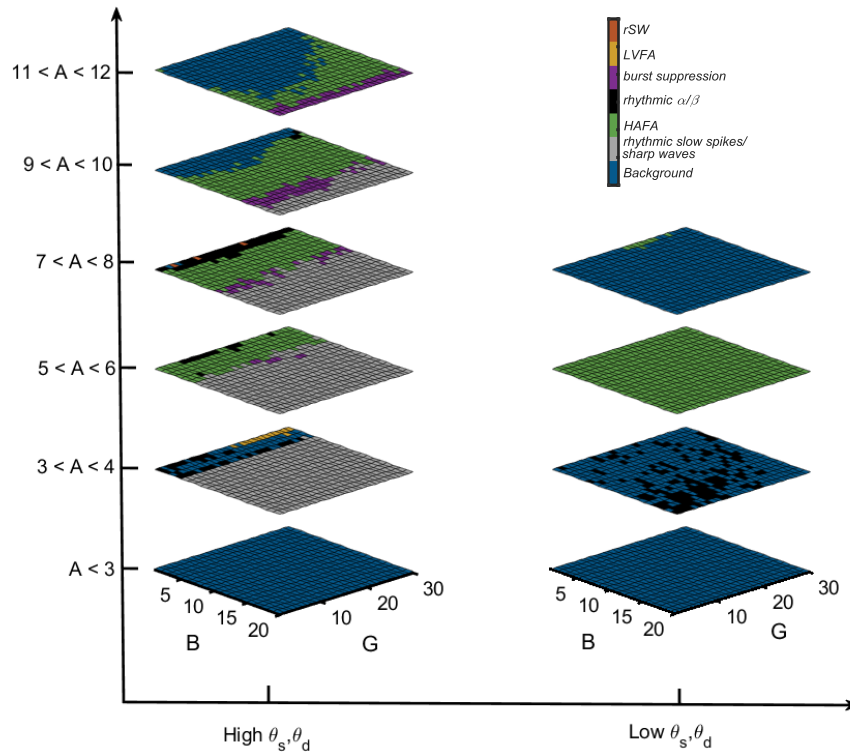


Figure 6-3 The results from the Monte Carlo simulation. The colors represent the most probable pattern of ictal activity for each one-unit interval of the parameters A , B , and G with $\theta_d = \theta_s = 4$ for the left column and $\theta_d = \theta_s = 0$ for the right column.

The result of our Monte Carlo simulations is presented in Fig.6-3 and shows that the background activity (shown in blue) was generated for both low and high excitation levels (i.e., A values). For the mid-range excitation values, non-background patterns of activity emerge (i.e., ictal activities). However, comparing the left and right columns we can see that for high values of θ_d and θ_s , due to higher inhibitory effect, the values of A that generate ictal activities (i.e., non-background activity) are less restricted compared to A values that produced ictal patterns when low values of θ_d and θ_s are in place.

To explore conditions in which the background activity can turn into an ictal pattern, we started from the background activity (i.e., the blue region in Fig.6-3) with both low and high A values (i.e., low and high levels of excitation) and tested as to whether collapse or recovery of the inhibitory activities (modeled by altering θ_d and θ_s) could result in seizure initiation and generation of different seizure onset patterns.

Seizure generation with low preictal excitation

For values of A lower than 3, both low and high values of θ_d and θ_s resulted in background activity –only for $2 < A < 3$ and high θ_d and θ_s for a very narrow range of parameter B was there a low probability of rhythmic slow spikes pattern which was not studied since in our stochastic analysis we only considered the most probable pattern of activity in each interval of the parameters which was the background activity. Therefore, when $A < 3$, by modifying the values of θ_d and θ_s we do not expect to observe a transition from background to ictal activity (i.e., seizure onset).

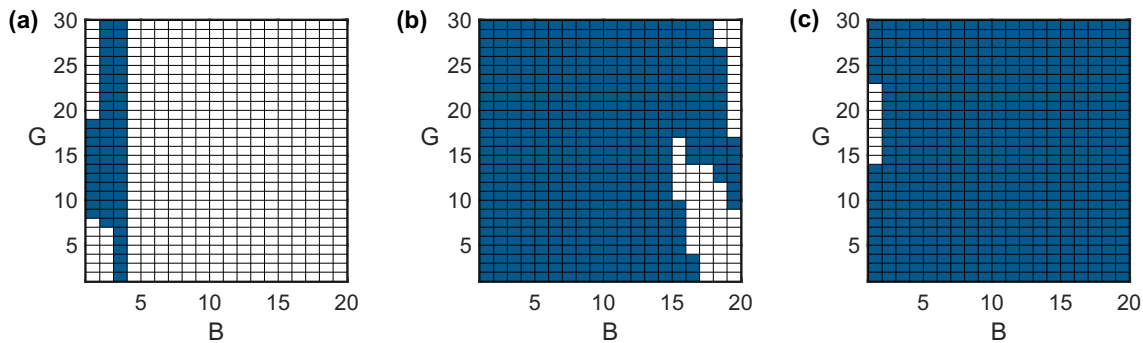


Figure 6-4 The ranges of parameters B and G generating background activity. (a) For $A=3.5$ and $\theta_d = \theta_s = 4$, (b) for $A=3.5$ and $\theta_d = \theta_s = 0$ (c) for $A=7.5$ and $\theta_d = \theta_s = 0$. The region in blue represents background activity while the region in white corresponds to the range of parameters that did not result in a background activity.

For A values between 3 and 4, the background could be generated for both low and high values of θ_d and θ_s . Thus, starting from these two parameter ranges of background activity and by modulating θ_d and θ_s , we studied the effect of depolarization block of inhibitory populations in seizure generation. To this end, we fixed A to the average value of this interval (3.5) and applying a Monte Carlo approach, found the ranges of B and G that generated background activities (Fig.6-4a, Fig.6-4b). In the next step, for the background activity with high θ_d and θ_s (blue region in Fig.6-4a), we separately decreased θ_d and θ_s value to 0 and, adopting the Monte Carlo approach, investigated if background activity switched to ictal patterns (i.e., seizures initiated). Similarly, for the background activity with low θ_d and θ_s (Fig.6-4b), we increased θ_d and θ_s to 4 and explored the possibility of seizure initiation.

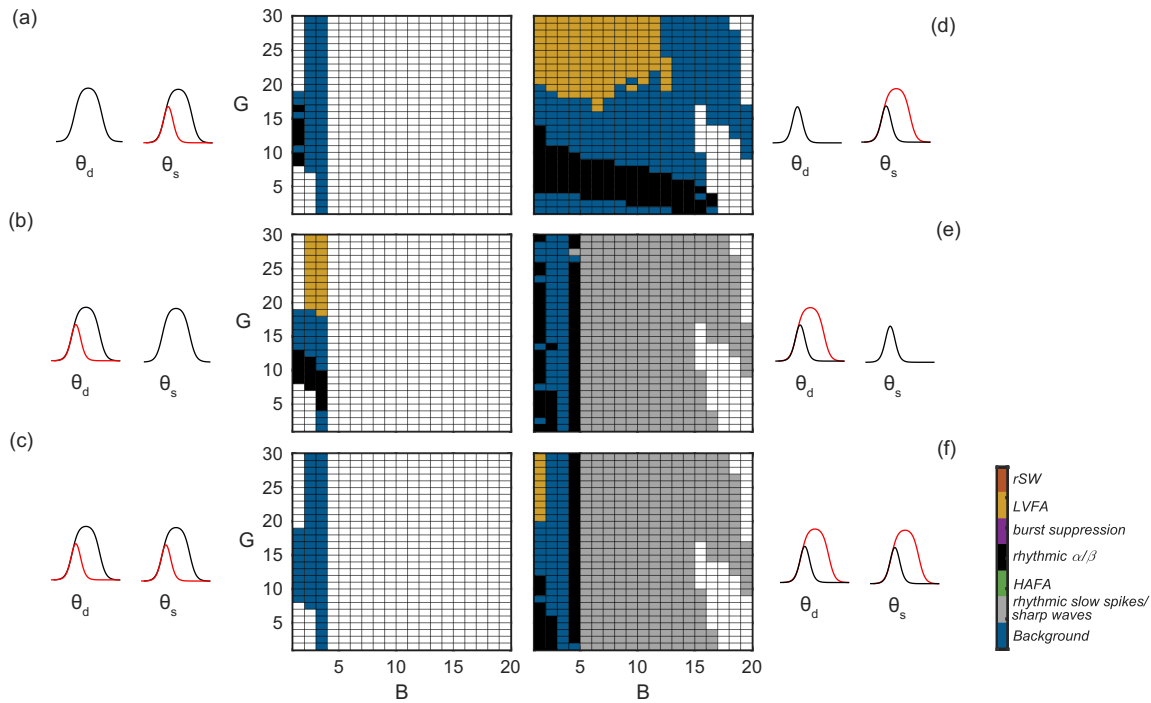


Figure 6-5 Seizure generation with low preictal excitation. The seizure onset patterns in the left and right columns are respectively generated starting from the background activities represented in Fig.6-4a and Fig. 6-4b. The underlying mechanism that generated the patterns in the left column is the collapse of (a) soma targeting inhibitory interneurons ($\theta_s: 4 \rightarrow 0$), (b) dendrite targeting inhibitory interneurons ($\theta_d: 4 \rightarrow 0$), (c) both dendrite and soma targeting inhibitory interneurons ($\theta_d: 4 \rightarrow 0, \theta_s: 4 \rightarrow 0$) and the mechanism responsible for the generating the onset patterns in the right column is the recovery of (d) soma targeting inhibitory interneurons ($\theta_s: 0 \rightarrow 4$), (e) dendrite targeting inhibitory interneurons ($\theta_d: 0 \rightarrow 4$), (f) both dendrite and soma targeting inhibitory interneurons ($\theta_d: 0 \rightarrow 4, \theta_s: 0 \rightarrow 4$). The region in white shows the range of parameters for which there was no background activity to start from and explore the transition to ictal patterns.

The left column in Fig.6-5 shows the result of the Monte Carlo simulations for the most probable seizure onset patterns for the first scenario (starting from background activity in Fig.6-4a). Here, the LVFA seizure onset pattern was generated when only the slow dendrite targeting inhibitory interneurons undergo depolarization block (decreased θ_d) which results in disinhibition of fast soma targeting inhibitory activity as well as increased excitation and the subsequent seizure generation. The results for the second scenario are depicted in the right column of Fig.6-5b where again the LVFA seizure onset is generated mainly by only enhancing the activity of fast soma targeting inhibitory interneuron (increasing θ_s while keeping $\theta_d = 0$). These results are suggestive of the involvement of the fast soma targeting inhibitory interneurons in the generation of LVFA

seizure onset pattern when there exist low levels of excitation. These findings are in accordance with the previous modeling and experimental studies reporting this seizure onset pattern when there is high inhibition and low excitation [11,202]. An example of the LVFA seizure onset pattern generated using our model is presented in Fig.6-6a. For the simulation of this pattern, the parameters B and G were selected from the ranges specified for this pattern in Fig.6-5d (Table 6-2).

Starting from the background activity with low θ_d and θ_s , enhancing θ_d either with or without enhancing θ_s , could generate rhythmic spikes/sharp waves onset pattern which shows the importance of slow dendrite targeting inhibitory interneurons for the generation of this onset pattern. Finally, as presented in Fig.6-5, for a restricted range of parameters B and G , rhythmic α/β onset patterns are generated (shown in black). Fig.6-6b presents the onset pattern rhythmic α/β for B and G selected from the ranges specified for this pattern in Fig.6-5b (Table 6-2).

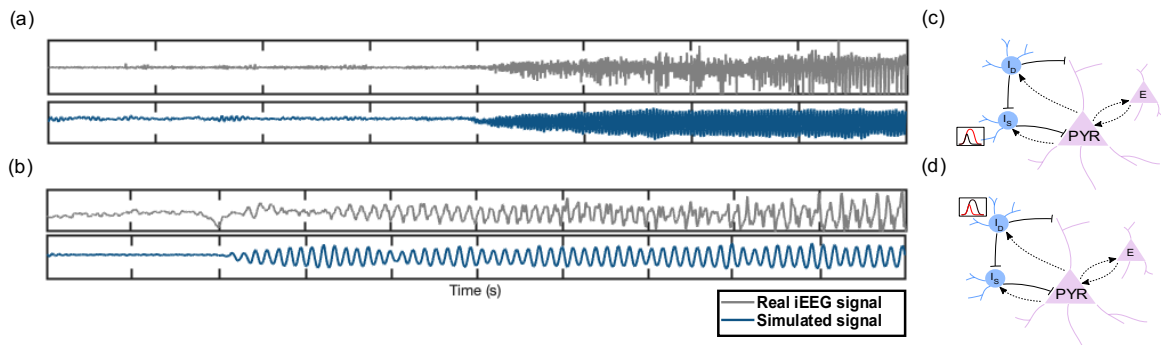


Figure 6-6 Low Voltage Fast Activity (LVFA) and rhythmic α seizure onset patterns. (a) LVFA seizure onset pattern with low excitation level (i.e., $A=3.5$). The parameters for the generation of this pattern are chosen from the ranges displayed in Fig. 6-5d and are presented in Table 6-2. (b) Rhythmic α seizure onset pattern with low excitation level (i.e., $A=3.5$) and parameters B and G from Fig. 6-5b. (c) The mechanism responsible for the generation of this onset pattern in (a) which is increasing the depolarization block threshold for some targeting interneurons (I_s). (d) The mechanism responsible for the generation of this onset pattern in (b) which is decreasing the depolarization block threshold for dendrite targeting interneurons (I_D).

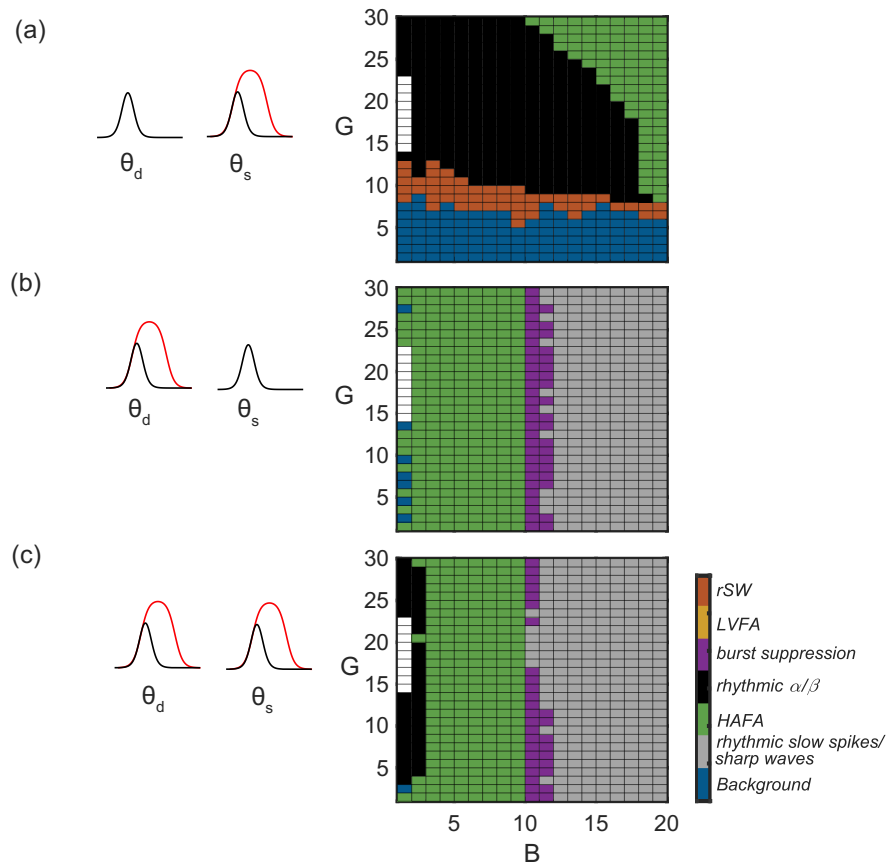


Figure 6-7 Seizure generation with high preictal excitation. These seizure onset patterns are generated starting from the background activity represented in Fig. 6-4c. The underlying mechanism generating these patterns is the recovery of (a) soma targeting inhibitory interneurons ($\theta_s: 0 \rightarrow 4$), (b) dendrite targeting inhibitory interneurons ($\theta_d: 0 \rightarrow 4$), (c) both dendrite and soma targeting inhibitory interneurons ($\theta_d: 0 \rightarrow 4, \theta_s: 0 \rightarrow 4$). The region in white shows the range of parameters for which there was no background activity to start from and explore the transition to ictal patterns.

Seizure generation with high preictal excitation

The other scenario that we considered for seizure generation is the transition from background activity to ictal activity when the excitation level was high (i.e., high values of A). The background activity for low θ_d and θ_s occurred when $7 < A < 8$ while for high θ_d and θ_s this range of parameter ‘ A ’ resulted in ictal patterns (Fig.6-3). Therefore, starting from this background activity with low θ_d and θ_s , we expected to observe transition to ictal patterns by increasing θ_d and θ_s (recovery of the inhibition). To this end, we fixed A to the average value of this range (7.5) and, taking the Monte Carlo approach, identified the range of parameters B and G that generated the background

activity (Fig.6-4c). For this range of parameters (blue region in Fig. 6-4c), we then increased θ_d and θ_s values separately. As presented in Fig.6-7, increasing only θ_d or both θ_d and θ_s results in seizure generation with mainly three distinct onset patterns: HAFA, burst suppression, and rhythmic spikes/sharp waves (Fig.6-7b&6-7c). However, when we only increased θ_s (and not θ_d), the seizure onset patterns and the range of parameters generating them were substantially different (Fig.6-7a). In this scenario, we observed rSW and rhythmic α/β and for a restricted range of parameters HAFA onset patterns. As the dendrite targeting interneurons also inhibits the soma targeting interneurons, high values of θ_d result in suppression of the activity of the soma targeting interneurons, and consequently, changes in parameter G introduce lower variations in the activity patterns we observe (Fig.6-7b&6-7c) while low θ_d disinhibits the soma targeting interneurons and allows the parameter G to have a more noticeable effect in the patterns that are generated (Fig.6-7a).

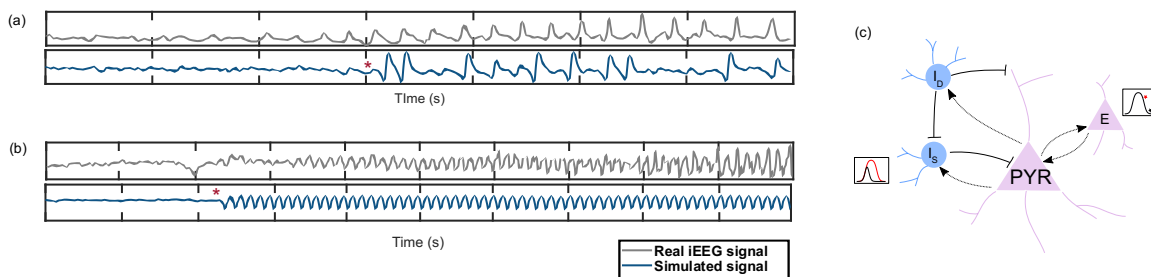


Figure 6-8 Rhythmic spike and wave (rSW) and rhythmic α seizure onset patterns. (a) RSW and (b) rhythmic α seizure onset patterns generated with the parameters B and G chosen from Fig. 6-7a (Table 6-2). (c) The mechanism that resulted in the generation of these two patterns in our model which is the recovery of the soma targeting interneurons and the consequent removal of the depolarization block of the excitatory population.

An example of the simulation of rSW seizure onset pattern is presented in Fig.6-8a. Here, the parameters B and G were selected from the ranges specified in Fig.6-7a for rSW onset pattern (Table 6-2). In this example, enhancing the depolarization block threshold of the soma targeting inhibitory population (θ_s) results in recovery of the inhibitory activity which consequently removes the depolarization block of the excitatory population (Fig.6-8c) and generates rSW seizure onset pattern. Fig.6-8b shows an example of rhythmic α/β seizure onset pattern. In this example, similar to Fig.6-8a, the recovery of the soma targeting inhibitory interneurons (θ_s) enhances the activity of

this population which in turn removes the depolarization block of the excitatory population (Fig.6-8c). However, here the parameters B and G were selected from the ranges that generate α/β onset patterns (Fig. 6-7a, Table 6-2). In Fig.6-9 as an example, a 3-dimensional representation of the dynamic change in the activation function of the inhibitory population is depicted. Increasing the threshold for depolarization block of the inhibitory population enhances the inhibition (Fig.6-9a) which in turn draws the excitatory population out of depolarization block (Fig.6-9b).

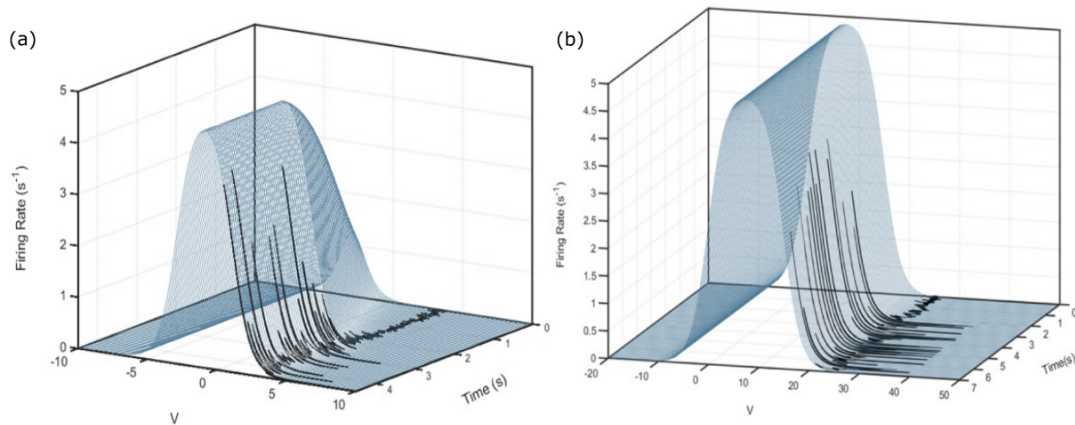


Figure 6-9 An example for the 3-dimensional representation of the excitatory and inhibitory activation functions. (a) The dynamic change of the inhibitory activation function due to an increased threshold for the depolarization block of this population results in enhanced inhibitory activation. (b) The excitatory population is being drawn out of depolarization block due to its inhibitory input shown in (a).

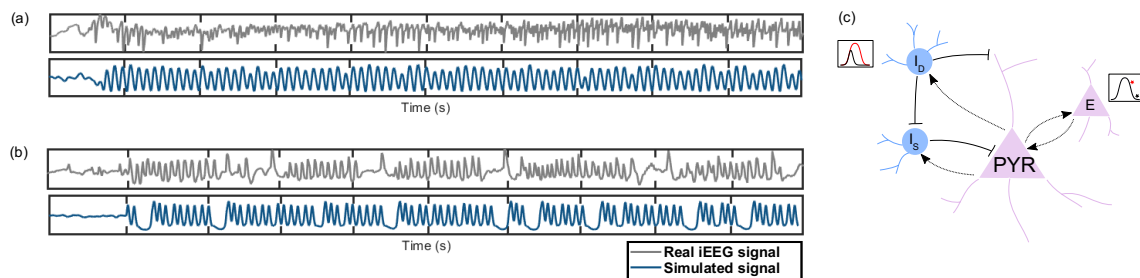


Figure 6-10 High Amplitude Fast Activity (HAFAs) and burst suppression seizure onset patterns. (a) HAFAs and (b) burst suppression seizure onset patterns generated with the parameters chosen from Fig. 6-7b (Table 6-2). The DC shift from the background to ictal activity is removed in this simulated signal. (c) The mechanism responsible for the generation of the onset patterns is shown in (a) and (b). The recovery of dendrite targeting inhibitory interneurons draws the excitatory population out of the depolarization block and initiates seizures.

By the recovery of the inhibitory activity of dendrite targeting interneurons (θ_d), Fig.6-10a and Fig. 6-10b respectively represent an example for HAFA and burst suppression seizure onset patterns with the parameter B and G selected from the ranges suggested in Fig.6-7b (Table 6-2).

And finally, by recovery of the inhibitory activities for both dendrite and soma targeting interneurons (θ_d and θ_s), Fig.6-11 depicts an example for rhythmic slow spike seizure onset pattern with the parameter B and G selected from the ranges suggested in Fig.6-7c (Table 6-2).

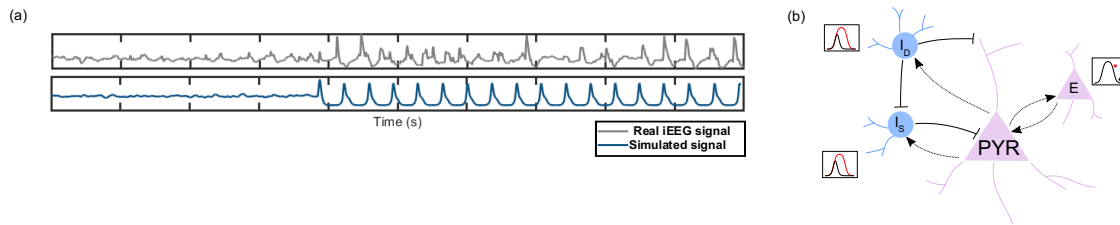


Figure 6-11 Rhythmic slow spikes seizure onset pattern. (a) Rhythmic slow spikes seizure onset pattern which is generated with the parameters chosen from Fig. 6-7c. The DC shift from the background to ictal activity is removed in this simulated signal. (b) The mechanism resulting in the generation of the onset patterns shown in (a) which is the recovery of both dendrite and soma targeting inhibitory interneurons and the consequent removal of the depolarization block of the excitatory population.

In summary, using our model, LVFA seizure onset pattern could be reproduced mainly by low excitation and high soma targeting inhibitory activity while rSW, HAFA, and burst suppression seizure onset patterns could only be produced when there was high excitation level (high A). For the latter due to the high excitatory activity, the excitatory population was experiencing depolarization block and the enhancement of the inhibitory activity removed the depolarization block of the excitatory population and seizures initiated. Two onset patterns - rhythmic α/β and rhythmic spikes/sharp waves - could be generated from the background activity with both high and low excitation levels. When excitation was high, rSW and rhythmic α/β patterns could be generated only when fast soma targeting inhibitory interneurons had recovered. However, the generation of burst suppression and rhythmic spikes/sharp waves onset patterns in this range of parameter ' A ' were more related to the recovery of slow dendrite targeting inhibitory interneurons.

Table 6-2 The values used for the simulated patterns. LVFA=Low Voltage Fast Activity, rSW=rhythmic Spike and Wave, HAFA=High Amplitude Fast Activity.

	Onset pattern	A	B	G	θ_d	θ_s
Fig. 6-6a	LVFA	3.5	7.5	28	0	0→4
Fig. 6-6b	rhythmic α	3.5	1	7	4→0	4
Fig. 6-8a	rSW	7.5	1	9	0	0→4
Fig. 6-8b	rhythmic α	7.5	5	15	0	0→4
Fig. 6-10a	HAFA	7.5	5	10	0→4	0
Fig. 6-10b	burst suppression	7.5	9.2	6	0→4	0
Fig. 6-11a	rhythmic slow spikes	7.5	19	20	0→4	0→4

6.4 Discussion

We found two main scenarios for the transition from background to ictal activity. Incorporating the effect of depolarization block in our model, the background activity could occur at two different excitation levels: low and high. Under special circumstances, the background activity with both these excitation levels could transition into ictal activity (i.e., seizure generation). Depending on the excitation level, our results showed that different inhibitory modulatory mechanisms - which will be further discussed below- could transform the background into ictal activity. These findings could provide an explanation for the experimental observations that report different behavior of the excitatory populations when they are in different excitability states (e.g., [317]). The optogenetic stimulation of excitatory populations has been reported to induced seizure-like activity when the membrane potential is close to the resting level (i.e., transition from background activity to ictal events) while the photostimulation of the same excitatory neural populations during an ongoing seizure-like-event terminate ictal discharges (i.e., return to the background activity) [317]. On a larger scale as well, the emergence of the background activity due to high excitation has been observed when the application of deep brain stimulation suppresses ongoing seizures (e.g., [318]). Depolarization block mechanism can offer an explanation for this dual effect of neural stimulation in seizure generation and termination and in general, could suggest pathways for seizure generation and termination mechanism. As presented in the schematic Fig.6-12, this bell-shaped activation function suggests that increasing the excitation level (e.g., by the application of electrical stimulation), depending on the current state of the excitatory population, can result in seizure initiation (Fig. 6-12, Onset I) or termination (Fig. 6-12, Termination I). Similarly, based on the

current state of the excitatory population, decreasing the excitation level (e.g., by enhancing inhibitory activity) can convert the background activity into ictal patterns (i.e., initiate seizures) (Fig. 6-12, Onset II) or terminate seizures (Fig. 6-12, Termination II).

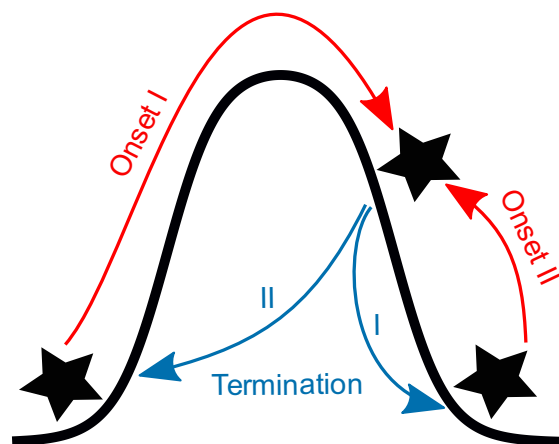


Figure 6-12 A schematic figure depicting our suggested seizure onset and termination pathways considering the depolarization block mechanism. Depending on the initial excitability state, enhancing the excitation level could result in both seizure generation (Onset I) and termination (Termination I), similarly, decreasing the excitation level could result in both seizure generation (Onset II) and termination (Termination II).

Our model showed that in the presence of different excitation levels and specific range of synaptic gain parameters both the enhancement and collapse of inhibitory activity could result in the generation of seizures. These findings could unify the seemingly contradictory mechanisms suggested by previous experimental studies for the involvement of inhibitory activity in seizure generation [4–11,13,14]. While the collapse of inhibition has been widely reported as a main mechanism underlying seizure generation [4–7], some experimental studies have addressed the enhanced inhibitory activity before and at the very onset of ictal activities [8–14]. In the current study, we found that depending on the current excitation level, both scenarios could result in the generation of seizures. More specifically, with low levels of excitation both the collapse and enhancement of inhibition could initiate seizures with different onset patterns while with high levels of excitation, only the enhancement of inhibitory activity could remove the depolarization block of the excitatory population and initiate seizures. Therefore, based on our modeling approach, depending on the excitation level and the range of synaptic gains, both collapse and enhancement of inhibitory activities could transform the background activity into ictal patterns (i.e., initiate seizures).

Our results point towards different underlying mechanisms for the generation of seizures with different onset patterns. For instance, seizures with LVFA onset pattern could be generated when there was low level of excitation in the model and enhanced somatic inhibition either due to the recovery of this inhibitory population or because of being disinhibited due to the collapse of dendrite targeting interneurons. These findings are in agreement with experimental studies suggesting enhanced inhibitory activity and low excitation at the onset of seizures with this onset pattern [10,11,62,202]. In the well-known framework [112] based on which we constructed our model, the impaired dendrite inhibition is reported responsible for the generation of LVFA onset pattern. Similar to our framework, in their model, the collapse of dendrite targeting interneurons which was considered as the direct mechanism generating this onset pattern, results in disinhibition of the soma targeting interneurons which could be an indirect mechanism responsible for the generation of this seizure onset pattern [112]. The repetitive spiking seizure onset pattern which is mainly attributed to seizures with high amplitude periodic spikes [67,319,320] as well as the bursting events, are reported to occur when the excitation is high [295,321] which agrees with our model findings. Our results showed that HAFA, rSW and burst suppression seizure onset patterns could be reproduced due to the recovery of the inhibitory activity only when the excitation level was high, and the excitatory population was experiencing depolarization block. The recovery of the inhibition removed the depolarization block of the excitatory population and initiated seizures.

Taken together, in order to explore the underlying mechanisms for the generation of seizures with different onset patterns, we constructed an excitatory-inhibitory neural population model and considered depolarization block mechanism and modulated the modeled slow and fast inhibitory activities. By including the depolarization block mechanism, our results showed that the background activity is possible for both low and high excitation levels (i.e., A values). Starting from these two background activities, we examined different scenarios in which a background state could transition into ictal patterns and explored whether seizures could be generated by modulating the inhibitory activities. Our results showed that for specific range of parameters both the enhancement and collapse of inhibitory activity could result in seizure initiation. By reproducing some of the most commonly observed seizure onset patterns, our findings suggest that the mechanisms responsible for seizure generation are different in seizures with distinct onset patterns. Understanding these different seizure generation mechanisms could aid us towards better seizure control measures. While, in this study, we mainly considered the modulation of the activation

function of the inhibitory populations (the collapse and recovery of the inhibition), an interesting expansion of this model could be incorporating the modulatory effect of the inhibitory population on the activation function of the excitatory population which could happen for instance due to shunting inhibition and GABAergic depolarization.

CHAPTER 7 GENERAL DISCUSSION

In this thesis, we first investigated the dynamic of state transitions during seizures to obtain a better understanding of how the epileptic brain modulates its state. We then expanded our investigation to the study of interictal into ictal state transition or seizure initiation by describing and classifying different seizure onset patterns. By studying the association between different seizure onset and termination patterns, we further investigated if seizures with distinct onset patterns terminate through different termination pathways. We then expanded our investigation of seizure onset patterns and explored whether different network topological features precede the generation of seizures with varying onset patterns by inspecting the epileptic network interactions prior to the emergence of different onset patterns. Our findings revealed different preictal network interactions for seizures with distinct onset patterns which led to the main idea for our last project: exploring the mechanisms underlying seizures with distinct onset patterns. To this end, we implemented a computational model that considers some of the most relevant physiological events such as impaired excitatory-inhibitory balance, collapse, and recovery of inhibition as well as depolarization block, and by reproducing some of the most common seizure onset patterns, we explored the mechanisms underlying various seizure onset patterns.

Our first project, described in chapter 4, focused on the study of state transition during seizures. Previously, due to the formation of strong network connections during ictal events, seizures have been considered as a hypersynchronous state of the brain. However, more recent studies have suggested different levels of synchrony for different neuronal ensembles within the epileptic focus and explored the evolution of these epileptic network states [107,124]. To explore the ictal state transition, we used intracerebral recordings from 17 patients with drug-resistant focal epilepsy to identify ictal states on two different scales: local and global. Global states, based on the patterns of functional connectivity matrices, highlight the overall state of the epileptic network; however, they lack spatial resolution in their search for different brain states. Because different brain regions might not simultaneously enter the same state, we also identified local states to gain an understanding regarding the state transition dynamics in different regions. To verify that our findings were not specific to our choice of methodology, we applied four different linear and nonlinear functional connectivity measures in the time domain, frequency domain, and phase space. Our findings showed that the brain globally remains longer in a state during ictal activity while it locally experiences a higher state transition rate in some regions such as the SOZ, mainly

for seizure-free patients. A direct comparison between seizure-free and non-seizure patients revealed different patterns only for local state transitions which can have practical application in predicting surgical outcome. The low global state transition rate displays the persistence of the same pattern for the epileptic network during ictal activity and the high local state transition rate for the SOZ and propagation channels points towards the unstable dynamic of these channels. These distinct dynamics of ictal state transitions at local and global scales could be due to the reported isolation of the SOZ for seizure-free patients [1] which may not allow the highly unstable SOZ channels to drive the network into a dynamic with high state transition rates. But, for non-seizure-free patients, the SOZ was not isolated [1] and the mutual interaction between the network and the SOZ in this patient group might be the reason that SOZ channels did not experience high state transition rates.

In our second project, which is discussed in chapter 5 of this thesis, we turned our focus on the transition from the interictal state into the ictal state (i.e., seizure generation). Because of the potential importance of seizure onset patterns in understanding ictogenesis [59,60,285], we took particular care to the study of various seizure onset patterns. Furthermore, to obtain some insights into the termination pathways through which seizures with different onset patterns end, we investigated the association between seizure onset and termination patterns. Our results showed that seizures with almost any onset pattern could terminate through common termination patterns which suggests that common termination mechanisms could terminate seizures regardless of the mechanisms that generated them. We also compared the extent of the channels upon which seizures terminated relative to SOZ channels and found that seizures with low voltage fast onset patterns as well as the fast termination patterns were more common among seizures terminating within their onset region compared to seizures terminating in more distributed areas. These results are in accordance with the studies arguing for the critical role of fast onset oscillations in hampering the propagation of ictal activity [214] and suggesting self-sufficiency of the brain regions involved in the generation of fast onset patterns to terminate the ictal activity. Contrary to these patterns, the Burst Suppression (BS) termination pattern was more frequently observed when the termination region was further distributed than the onset zone, suggesting the involvement of a larger region compared to the onset zone. These findings are in harmony with studies reporting the emergence of BS pattern when more distributed brain regions are involved caused by subcortical projections (e.g., [295,298]).

We extended our investigation of seizure onset patterns and studied the epileptic network preceding the formation of different onset patterns. Epilepsy is commonly considered a network disease [124,125,130] and according to this viewpoint, the network interactions and, not just the seizure generating region, is responsible for seizure generation [124,128,130,166]. Many studies have revealed complex interactions between the SOZ and other regions (NonSOZ) during ictogenesis [128,133,290,291]. Some studies have reported a critical role for the SOZ in recruiting and driving the surrounding regions [124,164,166,168]; others have suggested the failure of NonSOZ to contain the abnormal activity [147,291] to be responsible for seizure generation. Furthermore, it remains unclear if the epileptic network interactions between the SOZ and NonSOZ are different across seizures with different onset patterns. To address this question, we calculated a directed functional connectivity measure, PSI, and explored network interactions prior to the generation of different onset patterns. We found different driver regions before the generation of seizures with different onset patterns. More precisely, we found a higher inflow to the SOZ from NonSOZ channels in high frequency bands before the generation of *Fast* onset group seizures compared to seizures from the *Slow* onset group. The high frequency activities have been associated with the inhibitory postsynaptic potentials (IPSPs) and the synchronous activity of inhibitory interneurons [300], consistent with the experimental and theoretical studies reporting GABAergic inhibition as a critical element for the generation of high frequency activities [48,299,301–303]. Accordingly, our observation of the net inflow to the SOZ for seizures with *Fast* onset patterns in high frequency bands, points towards the involvement of inhibitory input to the SOZ from NonSOZ for the generation of these onset patterns. These findings suggested the existence of different network interactions prior to the generation of different seizure onset patterns and encouraged us to further investigate the underlying mechanisms for the generation of seizures with various onset patterns in neuronal population scale which shaped the final project of this thesis.

Seizure generation could be caused by the involvement of many complex cellular and synaptic components [227,228], which in turn, could give rise to distinct iEEG ictal patterns [62,221,307]. The impaired balance between excitatory and inhibitory activities has been the main focus of the ictogenesis researches [34,71,170–177]. The abnormally increased glutamatergic excitation and decreased GABAergic inhibition have been widely known as pro-epileptic and the main mechanism responsible for seizure generation, while the enhanced GABAergic activity has been commonly believed to protect against the generation of ictal events [4–7]. However, more recent

clinical and experimental studies cast doubt on this widely accepted paradigm by suggesting a critical role for the GABAergic network in the generation of focal seizures and reporting enhanced inhibition before and at the very onset of seizures [8–14]. In summary, distinct and even contradictory mechanisms have been suggested to underly seizure generation.

In the final project of this thesis (*Chapter 6*), by incorporating different and even contradictory mechanisms such as collapse and recovery of inhibitory activity as well as depolarization block, in a unified framework, we investigated whether distinct mechanisms underly the generation of seizures with different onset patterns. The implementation of depolarization block in our model resulted in two main scenarios for the transition from the background into ictal activity. More specifically, the background activity could occur at both low and high excitation levels and under special circumstances, the background activity with both these excitation levels could transition into ictal activity. Further, our model showed that depending on the current excitation level, different modulation of the inhibitory activity could result in the generation of seizures. When the excitation was low, both the collapse and enhancement of the inhibitory activity could generate seizures with different onset patterns whereas, with high excitation, only the enhancement of inhibition by removing the depolarization block of the excitatory population could initiate seizures. Therefore, based on our modeling approach, depending on the current excitability state and parameter ranges, both the enhancement and collapse of inhibitory activity could result in the generation of seizures which could unify the seemingly contradictory mechanisms reported by previous experimental studies for the role of inhibition in generating ictal activities [4–11,13,14].

Our results suggest that seizures with different onset patterns could originate from different underlying mechanisms. For instance, seizures with LVFA onset pattern could be generated with lowered excitation levels and enhanced somatic inhibition. These findings agree with the reports of some experimental studies on enhanced inhibition and low excitation at the onset of seizures with this onset pattern [10,11,62,202]. In some experimental studies, the repetitive spiking seizure onset pattern (i.e., seizures with high amplitude periodic spikes) [67,319,320] and BS have been observed with high excitation levels [295,321], consistent with our model findings. Our model showed that HAFA, rSW, and BS seizure onset patterns could be reproduced at high excitability states and due to the recovery of the inhibitory activity which subsequently removed the depolarization block of the excitatory population.

To sum up, using our modeling approach, by considering some of the relevant neurophysiological events, we could reproduce some of the most commonly observed seizure onset patterns and, further discussed the existence of different mechanisms underlying the generation of seizures with various onset patterns (Fig. 8-1).

CHAPTER 8 CONCLUSION AND RECOMMENDATIONS

The brain constantly modulates its state and to capture the pattern of these state changes in an epileptic brain, we applied various functional connectivity measures and calculated ictal global and local state transitions. We found distinct dynamics for the ictal state transitions at different scales: the brain globally remains in a state for a longer time while locally, it shows a higher rate of state transition in some regions such as the SOZ. Different regions of the brain might not undergo the same state at the same time and by studying local states we could capture the spatial information of the epileptic brain state transition. In addition, our results indicated an inherent difference of SOZ channels between seizure-free (SF) and non-seizure-free (NSF) patients which can be explained by inaccurate localization of SOZ in patients with unfavorable surgery outcome. An interesting direction for future studies can be taking advantage of a larger database to explore whether the analysis of ictal local state transitions could be a useful predictor for surgical outcome. We then turned our attention to the interictal to ictal state transition (i.e., seizure initiation). More specifically, we studied and classified the patterns that emerge during this transition and, further, explored their associated termination patterns. Some termination patterns were exclusively associated with specific onset patterns. However, we found that seizures with almost all onset patterns could terminate through common termination patterns: the BS and rSW/rPSW termination patterns. We further expanded our analysis and, using a directed functional connectivity measure, investigated the network interactions during the transition from interictal into various ictal onset patterns. Our results indicated a higher inflow to the SOZ from NonSOZ in high frequency ranges for seizures with *Fast* onset activity compared to seizures with *Slow* onset patterns. These findings suggest that seizures with various onset patterns originate from different underlying mechanisms and led us to investigate this hypothesis in a neuronal population scale by constructing an excitatory-inhibitory neural population model. In this computational framework, we considered the depolarization block mechanism and simulated the collapse and recovery of inhibitory activities. By incorporating the depolarization block mechanism in our model, the background activity could occur for both low and high excitation levels. We then started from these two background activities and investigated different scenarios of the transition from the background state into seizure onset patterns by modulating the inhibitory activities. Our findings suggested that, for specific ranges of parameters, both the recovery and collapse of inhibition could result in seizure generation. We further reproduced some of the most commonly observed seizure onset patterns and showed that

there could be different mechanisms responsible for the generation of seizures with distinct onset patterns. A visual summary of our main research questions and findings is depicted in (Fig. 8-1).

One possible extension to our modeling exercise could be investigating the effect of different drugs in suppressing or terminating seizures with different patterns by implementing their mode of action in our computational model. It would also be interesting to study the effect of different GABAergic modulations in the propagation of ictal activity in a modeled network. In other words, apart from the temporal patterns of ictal activity, we can study its spatial patterns to better understand, for instance, why some seizures tend to remain focal while some others propagate and entrain other regions.

In this study, we only modulated the activation function of the inhibitory populations by modeling the collapse and recovery of the inhibitory activity. The model could be further expanded by incorporating the modulatory effect of the inhibitory population on the activation function of the excitatory population which could occur due to mechanisms such as shunting inhibition and GABAergic depolarization.

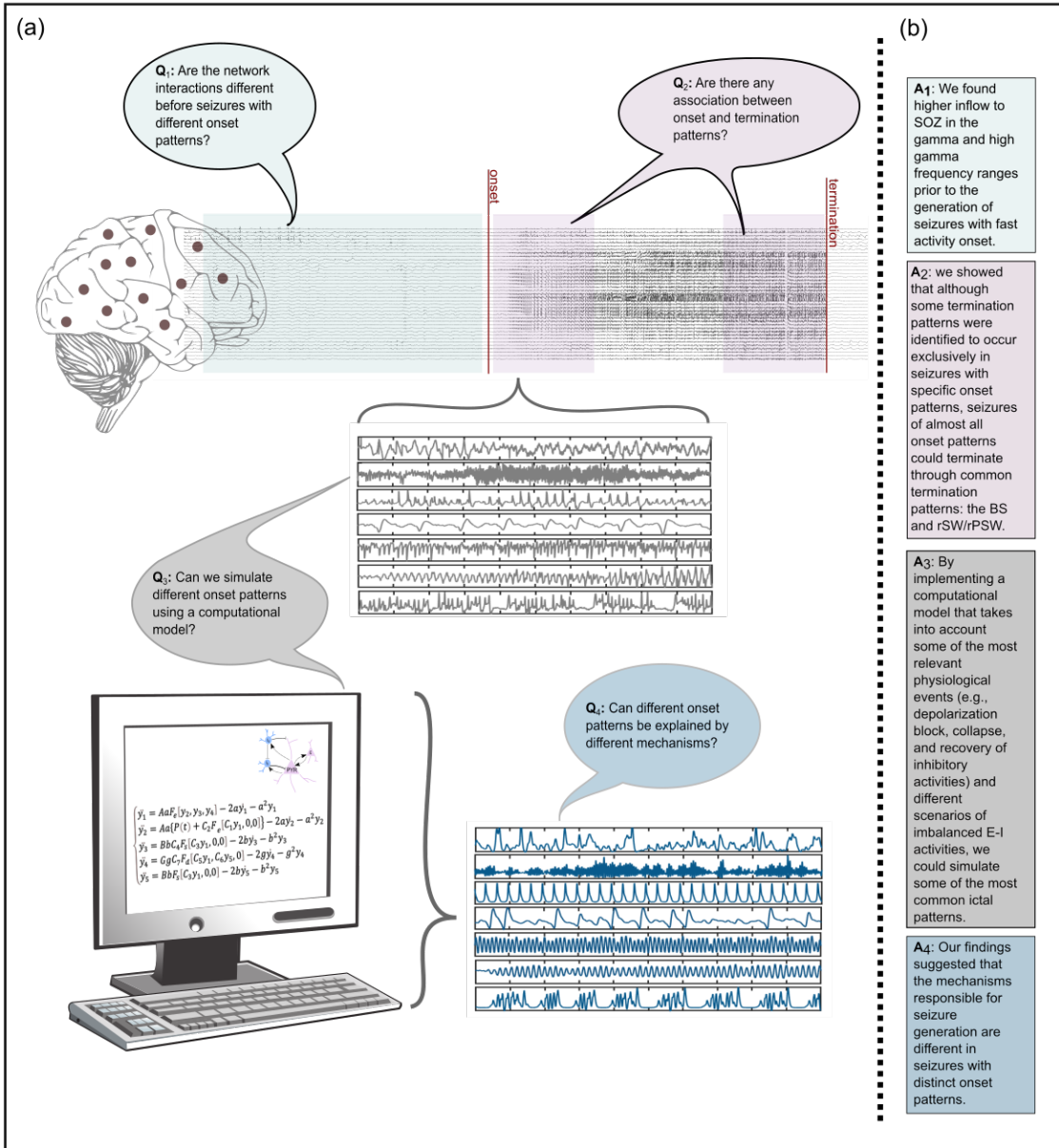


Figure 8-1 A visual summary of the main findings of this thesis. (a) Our main research questions displayed as Q₁ to Q₄. (b) Our findings presented as A₁ to A₄ which respectively answer questions Q₁ to Q₄.

REFERENCES

- [1] S.P. Burns, S. Santaniello, R.B. Yaffe, C.C. Jouny, N.E. Crone, G.K. Bergey, W.S. Anderson, S. V. Sarma, Network dynamics of the brain and influence of the epileptic seizure onset zone, *Proc. Natl. Acad. Sci.* 111 (2014) E5321–E5330. <https://doi.org/10.1073/pnas.1401752111>.
- [2] A.N. Khambhati, K.A. Davis, B.S. Oommen, S.H. Chen, T.H. Lucas, B. Litt, D.S. Bassett, Dynamic Network Drivers of Seizure Generation, Propagation and Termination in Human Neocortical Epilepsy, *PLOS Comput. Biol.* 11 (2015) e1004608. <https://doi.org/10.1371/journal.pcbi.1004608>.
- [3] H. Liu, P. Zhang, Phase synchronization dynamics of neural network during seizures, *Comput. Math. Methods Med.* 2018 (2018). <https://doi.org/10.1155/2018/1354915>.
- [4] A.J. Trevelyan, D. Sussillo, B.O. Watson, R. Yuste, Modular propagation of epileptiform activity: Evidence for an inhibitory veto in neocortex, *J. Neurosci.* 26 (2006) 12447–12455. <https://doi.org/10.1523/JNEUROSCI.2787-06.2006>.
- [5] R.R. Parrish, N.K. Codadu, C. Mackenzie-Gray Scott, A.J. Trevelyan, Feedforward inhibition ahead of ictal wavefronts is provided by both parvalbumin- and somatostatin-expressing interneurons, *J. Physiol.* 597 (2019) 2297–2314. <https://doi.org/10.1113/JP277749>.
- [6] Y. Ben-Ari, K. Krnjevic, W. Reinhardt, Hippocampal seizures and failure of inhibition, *Can. J. Physiol. Pharmacol.* 57 (1979) 1462–1466. <https://doi.org/10.1139/y79-218>.
- [7] M. Cammarota, G. Losi, A. Chiavegato, M. Zonta, G. Carmignoto, Fast spiking interneuron control of seizure propagation in a cortical slice model of focal epilepsy, *J. Physiol. Neurosci. C 2013 Authors. J. Physiol. C.* 591 (2013) 807–822. <https://doi.org/10.1113/jphysiol.2012.238154>.
- [8] L.-R. Shao, C.W. Habela, C.E. Stafstrom, Pediatric Epilepsy Mechanisms: Expanding the Paradigm of Excitation/Inhibition Imbalance, *Children.* 6 (2019) 23. <https://doi.org/10.3390/children6020023>.
- [9] E.O. Mann, I. Mody, The multifaceted role of inhibition in epilepsy: Seizure-genesis through excessive GABAergic inhibition in autosomal dominant nocturnal frontal lobe

- epilepsy, *Curr. Opin. Neurol.* 21 (2008) 155–160.
<https://doi.org/10.1097/WCO.0b013e3282f52f5f>.
- [10] B. Elahian, N.E. Lado, E. Mankin, S. Vangala, A. Misra, K. Moxon, I. Fried, A. Sharan, M. Yeasin, R. Staba, A. Bragin, M. Avoli, M.R. Sperling, J. Engel, S.A. Weiss, Low-voltage fast seizures in humans begin with increased interneuron firing, *Ann. Neurol.* 84 (2018) 588–600. <https://doi.org/10.1002/ana.25325>.
- [11] M. De Curtis, M. Avoli, GABAergic networks jump-start focal seizures, *Epilepsia.* 57 (2016) 679–687. <https://doi.org/10.1111/epi.13370>.
- [12] T.C. Kang, S.K. Park, I.K. Hwang, S.J. An, S.Y. Choi, O.S. Kwon, N.I. Baek, H.Y. Lee, M.H. Won, The altered expression of GABA shunt enzymes in the gerbil hippocampus before and after seizure generation, *Neurochem. Int.* 42 (2003) 239–249.
[https://doi.org/10.1016/S0197-0186\(02\)00079-7](https://doi.org/10.1016/S0197-0186(02)00079-7).
- [13] Y. Ben-Ari, Seizures beget seizures: The quest for GABA as a key player, *Crit. Rev. Neurobiol.* 18 (2006) 135–144. <https://doi.org/10.1615/CritRevNeurobiol.v18.i1-2.140>.
- [14] M. Chang, J.A. Dian, S. Dufour, L. Wang, H. Moradi Chameh, M. Ramani, L. Zhang, P.L. Carlen, T. Womelsdorf, T.A. Valiante, Brief activation of GABAergic interneurons initiates the transition to ictal events through post-inhibitory rebound excitation, *Neurobiol. Dis.* 109 (2018) 102–116. <https://doi.org/10.1016/j.nbd.2017.10.007>.
- [15] O. Devinsky, A. Vezzani, T.J. O'Brien, N. Jette, I.E. Scheffer, M. De Curtis, P. Perucca, Epilepsy, *Nat. Rev. Dis. Prim.* 4 (2018). <https://doi.org/10.1038/nrdp.2018.24>.
- [16] J.S. Duncan, J.W. Sander, S.M. Sisodiya, M.C. Walker, Adult epilepsy, *Lancet.* 367 (2006) 1087–1100. <https://doi.org/10.1088/1751-8113/44/8/085201>.
- [17] P.N. Banerjee, D. Filippi, W. Allen Hauser, The descriptive epidemiology of epilepsy-A review, *Epilepsy Res.* 85 (2009) 31–45. <https://doi.org/10.1016/j.epilepsyres.2009.03.003>.
- [18] S.L. Moshé, E. Perucca, P. Ryvlin, T. Tomson, L. Neuroscience, Epilepsy: New advances, *Lancet.* 385 (2015) 884–898. [https://doi.org/10.1016/S0140-6736\(14\)60456-6](https://doi.org/10.1016/S0140-6736(14)60456-6).
- [19] J. Engel, T.A. Pedley, J. Aicardi, Epilepsy: A Comprehensive Textbook, Lippincott-Raven. 300 (2008) 442. <https://doi.org/10.1001/jama.300.4.443-a>.

- [20] G.G. Somjen, Ion regulation in the brain: Implications for pathophysiology, *Neuroscientist*. 8 (2002) 254–267. <https://doi.org/10.1177/1073858402008003011>.
- [21] O.K. Steinlein, Ion channels and epilepsy, *Am. J. Med. Genet. - Semin. Med. Genet.* 106 (2001) 146–159. <https://doi.org/10.1002/ajmg.1582>.
- [22] M.J. Ackerman, D.E. Clapham, Ion Channels — Basic Science and Clinical Disease, *N. Engl. J. Med.* 336 (1997) 1575–1586. <https://doi.org/10.1056/nejm199705293362207>.
- [23] W.A. Catterall, Voltage-gated calcium channels, *Cold Spring Harb. Perspect. Biol.* 3 (2011) 1–23. <https://doi.org/10.1101/cshperspect.a003947>.
- [24] T.J. Jentsch, V. Stein, F. Weinreich, A.A. Zdebik, Molecular structure and physiological function of chloride channels, *Physiol. Rev.* 82 (2002) 503–568. <https://doi.org/10.1152/physrev.00029.2001>.
- [25] D.C. Gadsby, Ion channels versus ion pumps: The principal difference, in principle, *Nat. Rev. Mol. Cell Biol.* 10 (2009) 344–352. <https://doi.org/10.1038/nrm2668>.
- [26] C. Vaillend, S.E. Mason, M.F. Cuttle, B.E. Alger, Mechanisms of neuronal hyperexcitability caused by partial inhibition of Na⁺-K⁺-ATPases in the rat CA1 hippocampal region, *J. Neurophysiol.* 88 (2002) 2963–2978. <https://doi.org/10.1152/jn.00244.2002>.
- [27] T. Grisar, D. Guillaume, A. V. Delgado-Escuet, Contribution of Na⁺,K⁺-ATPase to focal epilepsy: a brief review, *Epilepsy Res.* 12 (1992) 141–149. [https://doi.org/10.1016/0920-1211\(92\)90034-Q](https://doi.org/10.1016/0920-1211(92)90034-Q).
- [28] M.M. Haglund, W.L. Stahl, D.D. Kunkel, P.A. Schwartzkroin, Developmental and regional differences in the localization of Na,K-ATPase activity in the rabbit hippocampus, *Brain Res.* 343 (1985) 198–203. [https://doi.org/10.1016/0006-8993\(85\)91180-1](https://doi.org/10.1016/0006-8993(85)91180-1).
- [29] A. Fukuda, D.A. Prince, Postnatal development of electrogenic sodium pump activity in rat hippocampal pyramidal neurons, *Dev. Brain Res.* 65 (1992) 101–114. [https://doi.org/10.1016/0165-3806\(92\)90013-M](https://doi.org/10.1016/0165-3806(92)90013-M).
- [30] O.C. González, G.P. Krishnan, I. Timofeev, M. Bazhenov, Ionic and synaptic mechanisms of seizure generation and epileptogenesis, *Neurobiol. Dis.* 130 (2019) 104485.

- <https://doi.org/10.1016/j.nbd.2019.104485>.
- [31] H.F. Bradford, Glutamate, GABA and epilepsy, *Prog. Neurobiol.* 47 (1995) 477–511. [https://doi.org/10.1016/0301-0082\(95\)00030-5](https://doi.org/10.1016/0301-0082(95)00030-5).
- [32] P. Jedlicka, T. Deller, B.S. Gutkin, K.H. Backus, Activity-dependent intracellular chloride accumulation and diffusion controls GABA A receptor-mediated synaptic transmission, *Hippocampus.* 21 (2011) 885–898. <https://doi.org/10.1002/hipo.20804>.
- [33] G. Huberfeld, L. Wittner, S. Clemenceau, M. Baulac, K. Kaila, R. Miles, C. Rivera, Perturbed chloride homeostasis and GABAergic signaling in human temporal lobe epilepsy, *J. Neurosci.* 27 (2007) 9866–9873. <https://doi.org/10.1523/JNEUROSCI.2761-07.2007>.
- [34] H.E. Scharfman, N. Kline, P.D. Helen E. Scharfman, H.E. Scharfman, The Neurobiology of Epilepsy, *Curr. Neurol. Neurosci. Rep.* 7 (2007) 348–354. <https://doi.org/10.1007/s11910-007-0053-z>.
- [35] S. Gigout, J. Louvel, H. Kawasaki, M. D’Antuono, V. Armand, I. Kurcewicz, A. Olivier, J. Laschet, B. Turak, B. Devaux, R. Pumain, M. Avoli, Effects of gap junction blockers on human neocortical synchronization, *Neurobiol. Dis.* 22 (2006) 496–508. <https://doi.org/10.1016/j.nbd.2005.12.011>.
- [36] R.D. Traub, H. Michelson-Law, A.E.J. Bibbig, E.H. Buhl, M.A. Whittington, Gap junctions, fast oscillations and the initiation of seizures, *Adv. Exp. Med. Biol.* 548 (2004) 110–122. https://doi.org/10.1007/978-1-4757-6376-8_9.
- [37] M. Avoli, M. de Curtis, GABAergic synchronization in the limbic system and its role in the generation of epileptiform activity, *Prog. Neurobiol.* 95 (2011) 104–132. <https://doi.org/10.1016/j.pneurobio.2011.07.003>.
- [38] R. Khazipov, GABAergic synchronization in epilepsy, *Cold Spring Harb. Perspect. Med.* 6 (2016) a022764. <https://doi.org/10.1101/cshperspect.a022764>.
- [39] S.R. Cobb, E.H. Buhl, K. Halasy, O. Paulsen, P. Somogyi, Synchronization of neuronal activity in hippocampus by individual GABAergic interneurons, *Nature.* 378 (1995) 75–78. <https://doi.org/10.1038/378075a0>.

- [40] T.P. Sutula, F.E. Dudek, Unmasking recurrent excitation generated by mossy fiber sprouting in the epileptic dentate gyrus: an emergent property of a complex system, *Prog. Brain Res.* 163 (2007) 541–563. [https://doi.org/10.1016/S0079-6123\(07\)63029-5](https://doi.org/10.1016/S0079-6123(07)63029-5).
- [41] K. Blinowska, P. Durka, Electroencephalography (EEG), in: *Wiley Encycl. Biomed. Eng.*, John Wiley & Sons, Inc., Hoboken, NJ, USA, 2006. <https://doi.org/10.1002/9780471740360.ebs0418>.
- [42] S. Noachtar, J. Rémi, The role of EEG in epilepsy: A critical review, *Epilepsy Behav.* 15 (2009) 22–33. <https://doi.org/10.1016/j.yebeh.2009.02.035>.
- [43] J. Engel, A practical guide for routine EEG studies in epilepsy, *J. Clin. Neurophysiol.* 1 (1984) 109–142. <https://doi.org/10.1097/00004691-198404000-00001>.
- [44] M. Sundaram, R.M. Sadler, G.B. Young, N. Pillay, EEG in epilepsy: Current perspectives, *Can. J. Neurol. Sci.* 26 (1999) 255–262. <https://doi.org/10.1017/S0317167100000342>.
- [45] D. Zumsteg, H.G. Wieser, Presurgical evaluation: Current role of invasive EEG, *Epilepsia.* 41 (2000) 55–60. <https://doi.org/10.1111/j.1528-1157.2000.tb01535.x>.
- [46] A.K. Engel, C.K.E. Moll, I. Fried, G.A. Ojemann, Invasive recordings from the human brain: Clinical insights and beyond, *Nat. Rev. Neurosci.* 6 (2005) 35–47. <https://doi.org/10.1038/nrn1585>.
- [47] K.J. Friston, Functional and effective connectivity in neuroimaging: A synthesis, *Hum. Brain Mapp.* 2 (1994) 56–78. <https://doi.org/10.1002/hbm.460020107>.
- [48] G. Buzsáki, X.J. Wang, Mechanisms of gamma oscillations, *Annu. Rev. Neurosci.* 35 (2012) 203–225. <https://doi.org/10.1146/annurev-neuro-062111-150444>.
- [49] F. Varela, J.P. Lachaux, E. Rodriguez, J. Martinerie, The brainweb: Phase synchronization and large-scale integration, *Nat. Rev. Neurosci.* 2 (2001) 229–239. <https://doi.org/10.1038/35067550>.
- [50] M. Siegel, T.H. Donner, A.K. Engel, Spectral fingerprints of large-scale neuronal interactions, *Nat. Rev. Neurosci.* 13 (2012) 121–134. <https://doi.org/10.1038/nrn3137>.
- [51] P. Fries, Rhythms for Cognition: Communication through Coherence, *Neuron.* 88 (2015) 220–235. <https://doi.org/10.1016/j.neuron.2015.09.034>.

- [52] P. Fries, A mechanism for cognitive dynamics: Neuronal communication through neuronal coherence, *Trends Cogn. Sci.* 9 (2005) 474–480.
<https://doi.org/10.1016/j.tics.2005.08.011>.
- [53] T. Womelsdorf, J.M. Schoffelen, R. Oostenveld, W. Singer, R. Desimone, A.K. Engel, P. Fries, Modulation of neuronal interactions through neuronal synchronization, *Science* (80-.). 316 (2007) 1609–1612. <https://doi.org/10.1126/science.1139597>.
- [54] D. Vatansever, D.K. Menon, A.E. Manktelow, B.J. Sahakian, E.A. Stamatakis, Default mode dynamics for global functional integration, *J. Neurosci.* 35 (2015) 15254–15262.
<https://doi.org/10.1523/JNEUROSCI.2135-15.2015>.
- [55] U. Braun, A. Schäfer, H. Walter, S. Erk, N. Romanczuk-Seiferth, L. Haddad, J.I. Schweiger, O. Grimm, A. Heinz, H. Tost, A. Meyer-Lindenberg, D.S. Bassett, Dynamic reconfiguration of frontal brain networks during executive cognition in humans, *Proc. Natl. Acad. Sci. U. S. A.* 112 (2015) 11678–11683.
<https://doi.org/10.1073/pnas.1422487112>.
- [56] J.M. Shine, P.G. Bissett, P.T. Bell, O. Koyejo, J.H. Balsters, K.J. Gorgolewski, C.A. Moodie, R.A. Poldrack, The Dynamics of Functional Brain Networks: Integrated Network States during Cognitive Task Performance, *Neuron.* 92 (2016) 544–554.
<https://doi.org/10.1016/j.neuron.2016.09.018>.
- [57] J.R. Cohen, M. D’Esposito, The segregation and integration of distinct brain networks and their relationship to cognition, *J. Neurosci.* 36 (2016) 12083–12094.
<https://doi.org/10.1523/JNEUROSCI.2965-15.2016>.
- [58] A.M. Bastos, J.M. Schoffelen, A tutorial review of functional connectivity analysis methods and their interpretational pitfalls, *Front. Syst. Neurosci.* 9 (2016) 1–23.
<https://doi.org/10.3389/fnsys.2015.00175>.
- [59] P. Perucca, F. Dubeau, J. Gotman, Intracranial electroencephalographic seizure-onset patterns: Effect of underlying pathology, *Brain.* 137 (2014) 183–196.
<https://doi.org/10.1093/brain/awt299>.
- [60] S. Lagarde, S. Buzori, A. Trebuchon, R. Carron, D. Scavarda, M. Milh, A. McGonigal, F. Bartolomei, The repertoire of seizure onset patterns in human focal epilepsies:

- Determinants and prognostic values, *Epilepsia*. 60 (2019) 85–95.
<https://doi.org/10.1111/epi.14604>.
- [61] S.A. Lee, D.D. Spencer, S.S. Spencer, Intracranial EEG seizure-onset patterns in neocortical epilepsy, *Epilepsia*. 41 (2000) 297–307. <https://doi.org/10.1111/j.1528-1157.2000.tb00159.x>.
- [62] P. Salami, M. Lévesque, J. Gotman, M. Avoli, Distinct EEG seizure patterns reflect different seizure generation mechanisms, *J Neuro-Physiol*. 113 (2015) 2840–2844.
<https://doi.org/10.1152/jn.00031.2015.-Low-voltage>.
- [63] S.S. Spencer, P. Guimaraes, A. Katz, J. Kim, D. Spencer, Morphological Patterns of Seizures Recorded Intracranially, *Epilepsia*. 33 (1992) 537–545.
<https://doi.org/10.1111/j.1528-1157.1992.tb01706.x>.
- [64] A.L. Velasco, C.L. Wilson, T.L. Babb, J. Engel, Functional and anatomic correlates of two frequently observed temporal lobe seizure-onset patterns, *Neural Plast*. 7 (2000) 49–63.
<https://doi.org/10.1155/np.2000.49>.
- [65] S.S. Spencer, J. Kim, D.D. Spencer, Ictal spikes: a marker of specific hippocampal cell loss, *Electroencephalogr. Clin. Neurophysiol*. 83 (1992) 104–111.
[https://doi.org/10.1016/0013-4694\(92\)90023-B](https://doi.org/10.1016/0013-4694(92)90023-B).
- [66] E. Faught, R.I. Kuzniecky, D.C. Hurst, Ictal EEG wave forms from epidural electrodes predictive of seizure control after temporal lobectomy, *Electroencephalogr. Clin. Neurophysiol*. 83 (1992) 229–235. [https://doi.org/10.1016/0013-4694\(92\)90116-Y](https://doi.org/10.1016/0013-4694(92)90116-Y).
- [67] N.M. Wetjen, W.R. Marsh, F.B. Meyer, G.D. Cascino, E. So, J.W. Britton, S.M. Stead, G.A. Worrell, Intracranial electroencephalography seizure onset patterns and surgical outcomes in nonlesional extratemporal epilepsy: Clinical article, *J. Neurosurg*. 110 (2009) 1147–1152. <https://doi.org/10.3171/2008.8.JNS17643>.
- [68] I. Doležalová, M. Brázdil, M. Hermanová, I. Horáková, I. Rektor, R. Kuba, Intracranial EEG seizure onset patterns in unilateral temporal lobe epilepsy and their relationship to other variables, *Clin. Neurophysiol*. 124 (2013) 1079–1088.
<https://doi.org/10.1016/j.clinph.2012.12.046>.
- [69] K. Glomb, J. Cabral, A. Cattani, A. Mazzoni, A. Raj, B. Franceschiello, Computational

- Models in Electroencephalography, *Brain Topogr.* (2021). <https://doi.org/10.1007/s10548-021-00828-2>.
- [70] B. Molaee-Ardekani, P. Benquet, F. Bartolomei, F. Wendling, Computational modeling of high-frequency oscillations at the onset of neocortical partial seizures: From “altered structure” to “dysfunction,” *Neuroimage*. 52 (2010) 1109–1122. <https://doi.org/10.1016/j.neuroimage.2009.12.049>.
- [71] J.Y. Liou, E.H. Smith, L.M. Bateman, S.L. Bruce, G.M. McKhann, R.R. Goodman, R.G. Emerson, C.A. Schevon, L.F. Abbott, A model for focal seizure onset, propagation, evolution, and progression, *Elife*. 9 (2020) 1–27. <https://doi.org/10.7554/eLife.50927>.
- [72] E.H. Smith, E.M. Merricks, J.Y. Liou, C. Casadei, L. Melloni, T. Thesen, D.J. Friedman, W.K. Doyle, R.G. Emerson, R.R. Goodman, G.M. McKhann, S.A. Sheth, J.D. Rolston, C.A. Schevon, Dual mechanisms of ictal high frequency oscillations in human rhythmic onset seizures, *Sci. Rep.* 10 (2020) 1–14. <https://doi.org/10.1038/s41598-020-76138-7>.
- [73] P.L. Nunez, S.J. Williamson, Neocortical Dynamics and Human EEG Rhythms, *Phys. Today*. 49 (1996) 57–57. <https://doi.org/10.1063/1.2807585>.
- [74] K.M. Franks, T.M. Bartol, T.J. Sejnowski, A Monte Carlo model reveals independent signaling at central glutamatergic synapses, *Biophys. J.* 83 (2002) 2333–2348. [https://doi.org/10.1016/S0006-3495\(02\)75248-X](https://doi.org/10.1016/S0006-3495(02)75248-X).
- [75] F. Wendling, P. Benquet, F. Bartolomei, V. Jirsa, Computational models of epileptiform activity, *J. Neurosci. Methods*. 260 (2016) 233–251. <https://doi.org/10.1016/j.jneumeth.2015.03.027>.
- [76] W.W. Lytton, Computer modelling of epilepsy, *Nat. Rev. Neurosci.* 9 (2008) 626–637. <https://doi.org/10.1038/nrn2416>.
- [77] P. Mitra, H. Bokil, *Observed Brain Dynamics*, Oxford Univ. Press. (2007). <https://global.oup.com/academic/product/observed-brain-dynamics-9780195178081?cc=ca&lang=en&>.
- [78] R.D. Traub, D. Contreras, M.A. Whittington, Combined experimental/simulation studies of cellular and network mechanisms of epileptogenesis in vitro and in vivo, *J. Clin. Neurophysiol.* 22 (2005) 330–342.

<https://doi.org/10.1097/01.WNP.0000179967.76990.25>.

- [79] R.D. Traub, D. Contreras, M.O. Cunningham, H. Murray, F.E.N.N. LeBeau, A. Roopun, A. Bibbig, W.B. Wilent, M.J. Higley, M.A. Whittington, Single-Column Thalamocortical Network Model Exhibiting Gamma Oscillations, Sleep Spindles, and Epileptogenic Bursts, *J. Neurophysiol.* 93 (2005) 2194–2232. <https://doi.org/10.1152/jn.00983.2004>.
- [80] A. Destexhe, T. Bal, D.A. McCormick, T.J. Sejnowski, Ionic mechanisms underlying synchronized oscillations and propagating waves in a model of ferret thalamic slices, *J. Neurophysiol.* 76 (1996) 2049–2070. <https://doi.org/10.1152/jn.1996.76.3.2049>.
- [81] R.D. Traub, A. Draguhn, M.A. Whittington, T. Baldeweg, A. Bibbig, E.H. Buhl, D. Schmitz, Axonal gap junctions between principal neurons: A novel source of network oscillations, and perhaps epileptogenesis, *Rev. Neurosci.* 13 (2002) 1–30. <https://doi.org/10.1515/REVNEURO.2002.13.1.1>.
- [82] R.D. Traub, A. Bibbig, F.E.N. LeBeau, E.H. Buhl, M.A. Whittington, Cellular mechanisms of neuronal population oscillations in the hippocampus in vitro, *Annu. Rev. Neurosci.* 27 (2004) 247–278. <https://doi.org/10.1146/annurev.neuro.27.070203.144303>.
- [83] H. Kager, W.J. Wadman, G.G. Somjen, Simulated seizures and spreading depression in a neuron model incorporating interstitial space and ion concentrations, *J. Neurophysiol.* 84 (2000) 495–512. <https://doi.org/10.1152/jn.2000.84.1.495>.
- [84] G. Ullah, J.R.C. Jr., E. Barreto, S.J. Schiff, The influence of sodium and potassium dynamics on excitability, seizures, and the stability of persistent states: II. Network and glial dynamics, *J. Comput. Neurosci.* 2009 262. 26 (2008) 171–183. <https://doi.org/10.1007/S10827-008-0130-6>.
- [85] M. Bazhenov, I. Timofeev, F. Fröhlich, T.J. Sejnowski, Cellular and network mechanisms of electrographic seizures, *Drug Discov. Today Dis. Model.* 5 (2008) 45–57. <https://doi.org/10.1016/j.ddmod.2008.07.005>.
- [86] V. Santhakumar, I. Aradi, I. Soltesz, Role of Mossy Fiber Sprouting and Mossy Cell Loss in Hyperexcitability: A Network Model of the Dentate Gyrus Incorporating Cell Types and Axonal Topography, *J. Neurophysiol.* 93 (2005) 437–453. <https://doi.org/10.1152/jn.00777.2004>.

- [87] G.G. Somjen, H. Kager, W.J. Wadman, Computer simulations of neuron-glia interactions mediated by ion flux, *J. Comput. Neurosci.* 2008 252. 25 (2008) 349–365.
<https://doi.org/10.1007/S10827-008-0083-9>.
- [88] F. Fröhlich, T.J. Sejnowski, M. Bazhenov, Network Bistability Mediates Spontaneous Transitions between Normal and Pathological Brain States, *J. Neurosci.* 30 (2010) 10734–10743. <https://doi.org/10.1523/JNEUROSCI.1239-10.2010>.
- [89] O.C. González, Z. Shiri, G.P. Krishnan, T.L. Myers, S. Williams, M. Avoli, M. Bazhenov, Role of KCC2-dependent potassium efflux in 4-Aminopyridine-induced Epileptiform synchronization, *Neurobiol. Dis.* 109 (2018) 137–147.
<https://doi.org/10.1016/J.NBD.2017.10.011>.
- [90] W. Van Drongelen, H.C. Lee, M. Hereld, Z. Chen, F.P. Elsen, R.L. Stevens, Emergent epileptiform activity in neural networks with weak excitatory synapses, *IEEE Trans. Neural Syst. Rehabil. Eng.* 13 (2005) 236–241.
<https://doi.org/10.1109/TNSRE.2005.847387>.
- [91] W. Van Drongelen, H.C. Lee, R.L. Stevens, M. Hereld, Propagation of seizure-like activity in a model of neocortex, *J. Clin. Neurophysiol.* 24 (2007) 182–188.
<https://doi.org/10.1097/WNP.0b013e318039b4de>.
- [92] A. Destexhe, Spike-and-wave oscillations based on the properties of GABA(B) receptors, *J. Neurosci.* 18 (1998) 9099–9111. <https://doi.org/10.1523/jneurosci.18-21-09099.1998>.
- [93] A. Destexhe, T.J. Sejnowski, G protein activation kinetics and spillover of γ -aminobutyric acid may account for differences between inhibitory responses in the hippocampus and thalamus, *Proc. Natl. Acad. Sci. U. S. A.* 92 (1995) 9515–9519.
<https://doi.org/10.1073/pnas.92.21.9515>.
- [94] T. Bal, D. Debay, A. Destexhe, Cortical Feedback Controls the Frequency and Synchrony of Oscillations in the Visual Thalamus, *J. Neurosci.* 20 (2000) 7478–7488.
<https://doi.org/10.1523/JNEUROSCI.20-19-07478.2000>.
- [95] R.D. Traub, M.A. Whittington, E.H. Buhl, F.E.N. LeBeau, A. Bibbig, S. Boyd, H. Cross, T. Baldeweg, A possible role for gap junctions in generation of very fast EEG oscillations preceding the onset of, and perhaps initiating, seizures, *Epilepsia.* 42 (2001) 153–170.

<https://doi.org/10.1046/j.1528-1157.2001.26900.x>.

- [96] R.D. Traub, I. Pais, A. Bibbig, F.E.N. LeBeau, E.H. Buhl, S.G. Hormuzdi, H. Monyer, M.A. Whittington, Contrasting roles of axonal (pyramidal cell) and dendritic (interneuron) electrical coupling in the generation of neuronal network oscillations, *Proc. Natl. Acad. Sci. U. S. A.* 100 (2003) 1370–1374. <https://doi.org/10.1073/pnas.0337529100>.
- [97] R.D. Traub, R.K. Wong, Cellular mechanism of neuronal synchronization in epilepsy., *Science.* 216 (1982) 745–7. <https://doi.org/10.1126/science.7079735>.
- [98] W. Gerstner, W.M. Kistler, *Spiking Neuron Models*, Cambridge Univ. Press. (2002). <https://doi.org/10.1017/cbo9780511815706>.
- [99] W. Gerstner, W.M. Kistler, R. Naud, L. Paninski, *Neuronal dynamics: From single neurons to networks and models of cognition*, Cambridge Univ. Press. (2014) 1–577. <https://doi.org/10.1017/CBO9781107447615>.
- [100] A.N. Burkitt, A review of the integrate-and-fire neuron model: I. Homogeneous synaptic input, *Biol. Cybern.* 95 (2006) 1–19. <https://doi.org/10.1007/s00422-006-0068-6>.
- [101] Z. Wang, L. Guo, M. Adjouadi, A generalized leaky integrate-and-fire neuron model with fast implementation method, *Int. J. Neural Syst.* 24 (2014). <https://doi.org/10.1142/S0129065714400048>.
- [102] M. Ursino, G.E. La Cara, Travelling waves and EEG patterns during epileptic seizure: Analysis with an integrate-and-fire neural network, *J. Theor. Biol.* 242 (2006) 171–187. <https://doi.org/10.1016/J.JTBI.2006.02.012>.
- [103] P.R. Protachevicz, F.S. Borges, E.L. Lameu, P. Ji, K.C. Iarosz, A.H. Kihara, I.L. Caldas, J.D.J. Szezech, M.S. Baptista, E.E.N. Macau, C.G. Antonopoulos, A.M. Batista, J. Kurths, Bistable Firing Pattern in a Neural Network Model, *Front. Comput. Neurosci.* 0 (2019) 19. <https://doi.org/10.3389/FNCOM.2019.00019>.
- [104] D. Hall, L. Kuhlmann, Mechanisms of Seizure Propagation in 2-Dimensional Centre-Surround Recurrent Networks, *PLoS One.* 8 (2013) 71369. <https://doi.org/10.1371/journal.pone.0071369>.
- [105] E. McMullin, What do Physical Models Tell us?, in: *Stud. Log. Found. Math.*, NORTH-

HOLLAND PUBLISHING COMPANY, 1968: pp. 385–396.

[https://doi.org/10.1016/S0049-237X\(08\)71206-0](https://doi.org/10.1016/S0049-237X(08)71206-0).

- [106] A. Bokulich, How scientific models can explain, *Synthese*. 180 (2011) 33–45.
<https://doi.org/10.1007/s11229-009-9565-1>.
- [107] V.K. Jirsa, W.C. Stacey, P.P. Quilichini, A.I. Ivanov, C. Bernard, On the nature of seizure dynamics, *Brain*. 137 (2014) 2210–2230. <https://doi.org/10.1093/brain/awu133>.
- [108] K. El Houssaini, A.I. Ivanov, C. Bernard, V.K. Jirsa, Seizures, refractory status epilepticus, and depolarization block as endogenous brain activities, *Phys. Rev. E - Stat. Nonlinear, Soft Matter Phys.* 91 (2015) 010701.
<https://doi.org/10.1103/PhysRevE.91.010701>.
- [109] K. El Houssaini, C. Bernard, V.K. Jirsa, The epileptor model: A systematic mathematical analysis linked to the dynamics of seizures, refractory status epilepticus, and depolarization block, *ENeuro*. 7 (2020). <https://doi.org/10.1523/ENEURO.0485-18.2019>.
- [110] M.L. Saggio, V. Jirsa, Phenomenological Mesoscopic Models for Seizure Activity, *ArXiv Prepr.* (2020) 1–21. <http://arxiv.org/abs/2007.02783>.
- [111] Q.A. Nguyen, P. Moolchand, I. Soltesz, Connecting Pathological Cellular Mechanisms to Large-Scale Seizure Structures, *Trends Neurosci.* 43 (2020) 547–549.
<https://doi.org/10.1016/j.tins.2020.04.006>.
- [112] F. Wendling, F. Bartolomei, J.J. Bellanger, P. Chauvel, Epileptic fast activity can be explained by a model of impaired GABAergic dendritic inhibition, *Eur. J. Neurosci.* 15 (2002) 1499–1508. <https://doi.org/10.1046/j.1460-9568.2002.01985.x>.
- [113] F. Wendling, A. Hernandez, J.J. Bellanger, P. Chauvel, F. Bartolomei, Interictal to ictal transition in human temporal lobe epilepsy: Insights from a computational model of intracerebral EEG, *J. Clin. Neurophysiol.* 22 (2005) 343–356.
<https://doi.org/10.1097/01.wnp.0000184051.37267.f0>.
- [114] F. Wendling, J.J. Bellanger, F. Bartolomei, P. Chauvel, Relevance of nonlinear lumped-parameter models in the analysis of depth-EEG epileptic signals, *Biol. Cybern.* 83 (2000) 367–378. <https://doi.org/10.1007/s004220000160>.

- [115] P. Suffczynski, S. Kalitzin, F.H. Lopes Da Silva, Dynamics of non-convulsive epileptic phenomena modeled by a bistable neuronal network, *Neuroscience*. 126 (2004) 467–484. <https://doi.org/10.1016/j.neuroscience.2004.03.014>.
- [116] E. Bullmore, O. Sporns, Complex brain networks: Graph theoretical analysis of structural and functional systems, *Nat. Rev. Neurosci.* 10 (2009) 186–198. <https://doi.org/10.1038/nrn2575>.
- [117] C.J. Stam, Modern network science of neurological disorders, *Nat. Rev. Neurosci.* 15 (2014) 683–695. <https://doi.org/10.1038/nrn3801>.
- [118] D.S. Bassett, E. Bullmore, Small-World Brain Networks, *Neurosci.* 12 (2006) 512–523. <https://doi.org/10.1177/1073858406293182>.
- [119] U. Braun, S.F. Muldoon, D.S. Bassett, On Human Brain Networks in Health and Disease, in: *ELS*, John Wiley & Sons, Ltd, 2015: pp. 1–9. <https://doi.org/10.1002/9780470015902.a0025783>.
- [120] E.T. Bullmore, D.S. Bassett, Brain graphs: Graphical models of the human brain connectome, *Annu. Rev. Clin. Psychol.* 7 (2011) 113–140. <https://doi.org/10.1146/annurev-clinpsy-040510-143934>.
- [121] L. Deuker, E.T. Bullmore, M. Smith, S. Christensen, P.J. Nathan, B. Rockstroh, D.S. Bassett, Reproducibility of graph metrics of human brain functional networks, *Neuroimage*. 47 (2009) 1460–1468. <https://doi.org/10.1016/j.neuroimage.2009.05.035>.
- [122] P. van Mierlo, M. Papadopoulou, E. Carrette, P. Boon, S. Vandenberghe, K. Vonck, D. Marinazzo, Functional brain connectivity from EEG in epilepsy: Seizure prediction and epileptogenic focus localization, *Prog. Neurobiol.* 121 (2014) 19–35. <https://doi.org/10.1016/j.pneurobio.2014.06.004>.
- [123] E. Van Diessen, S.J.H. Diederer, K.P.J. Braun, F.E. Jansen, C.J. Stam, Functional and structural brain networks in epilepsy: What have we learned?, *Epilepsia*, 2013. <https://doi.org/10.1111/epi.12350>.
- [124] M.A. Kramer, S.S. Cash, Epilepsy as a Disorder of Cortical Network Organization, *Neurosci.* 18 (2012) 360–372. <https://doi.org/10.1177/1073858411422754>.

- [125] F. Bartolomei, S. Lagarde, F. Wendling, A. McGonigal, V. Jirsa, M. Guye, C. Bénar, Defining epileptogenic networks: Contribution of SEEG and signal analysis, *Epilepsia*. 58 (2017) 1131–1147. <https://doi.org/10.1111/epi.13791>.
- [126] S.S. Spencer, Neural networks in human epilepsy: Evidence of and implications for treatment, *Epilepsia*. 43 (2002) 219–227. <https://doi.org/10.1046/j.1528-1157.2002.26901.x>.
- [127] F. Wendling, P. Chauvel, A. Biraben, F. Bartolomei, From intracerebral EEG signals to brain connectivity: Identification of epileptogenic networks in partial epilepsy, *Front. Syst. Neurosci.* 4 (2010) 154. <https://doi.org/10.3389/fnsys.2010.00154>.
- [128] H. Laufs, Functional imaging of seizures and epilepsy: Evolution from zones to networks, *Curr. Opin. Neurol.* 25 (2012) 194–200. <https://doi.org/10.1097/WCO.0b013e3283515db9>.
- [129] M. Guye, F. Bartolomei, J.P. Ranjeva, Imaging structural and functional connectivity: Towards a unified definition of human brain organization?, *Curr. Opin. Neurol.* 21 (2008) 393–403. <https://doi.org/10.1097/wco.0b013e3283065cfb>.
- [130] H. Stefan, F.H.L. da Silva, Epileptic neuronal networks: Methods of identification and clinical relevance, *Front. Neurol.* 4 MAR (2013) 8. <https://doi.org/10.3389/fneur.2013.00008>.
- [131] F. Bartolomei, M. Guye, F. Wendling, Abnormal binding and disruption in large scale networks involved in human partial seizures, *EPJ Nonlinear Biomed. Phys.* 1 (2013) 1–16. <https://doi.org/10.1140/epjnbp11>.
- [132] A. Elshahabi, S. Klamer, A.K. Sahib, H. Lerche, C. Braun, N.K. Focke, Magnetoencephalography reveals a widespread increase in network connectivity in idiopathic/genetic generalized epilepsy, *PLoS One*. 10 (2015) 1–16. <https://doi.org/10.1371/journal.pone.0138119>.
- [133] D.J. Englot, P.E. Konrad, V.L. Morgan, Regional and global connectivity disturbances in focal epilepsy, related neurocognitive sequelae, and potential mechanistic underpinnings, *Epilepsia*. 57 (2016) 1546–1557. <https://doi.org/10.1111/epi.13510>.
- [134] Y. Li Hegner, J. Marquetand, A. Elshahabi, S. Klamer, H. Lerche, C. Braun, N.K. Focke, Increased Functional MEG Connectivity as a Hallmark of MRI-Negative Focal and

- Generalized Epilepsy, *Brain Topogr.* 31 (2018) 863–874. <https://doi.org/10.1007/s10548-018-0649-4>.
- [135] A. Coito, M. Genetti, F. Pittau, G.R. Iannotti, C.M. Michel, G. Plomp, S. Vulliemoz, Altered directed functional connectivity in temporal lobe epilepsy in the absence of interictal spikes: A high density EEG study, *Epilepsia.* 57 (2016) 402–411. <https://doi.org/10.1111/epi.13308>.
- [136] W. Staljanssens, G. Strobbe, R. Van Hohen, G. Birot, M. Gschwind, M. Seeck, S. Vandenberghe, S. Vulliemoz, P. van Mierlo, Seizure Onset Zone Localization from Ictal High-Density EEG in Refractory Focal Epilepsy, *Brain Topogr.* 30 (2017) 257–271. <https://doi.org/10.1007/s10548-016-0537-8>.
- [137] R.J. Morgan, I. Soltesz, Nonrandom connectivity of the epileptic dentate gyrus predicts a major role for neuronal hubs in seizures, *Proc. Natl. Acad. Sci.* 105 (2008) 6179–6184. <https://doi.org/10.1073/pnas.0801372105>.
- [138] G.J. Ortega, R.G. Sola, J. Pastor, Complex network analysis of human ECoG data, *Neurosci. Lett.* 447 (2008) 129–133. <https://doi.org/10.1016/j.neulet.2008.09.080>.
- [139] C. Wilke, G. Worrell, B. He, Graph analysis of epileptogenic networks in human partial epilepsy, *Epilepsia.* 52 (2011) 84–93. <https://doi.org/10.1111/j.1528-1167.2010.02785.x>.
- [140] M. Brázdil, J. Halánek, P. Jurák, P. Daniel, R. Kuba, J. Chrastina, Z. Novák, I. Rektor, Interictal high-frequency oscillations indicate seizure onset zone in patients with focal cortical dysplasia, *Epilepsy Res.* 90 (2010) 28–32. <https://doi.org/10.1016/j.eplepsyres.2010.03.003>.
- [141] M. Zijlmans, J. Jacobs, R. Zelmann, F. Dubeau, J. Gotman, High-frequency oscillations mirror disease activity in patients with epilepsy, *Neurology.* 72 (2009) 979–986. <https://doi.org/10.1212/01.wnl.0000344402.20334.81>.
- [142] F. Hutchings, C.E. Han, S.S. Keller, B. Weber, P.N. Taylor, M. Kaiser, Predicting Surgery Targets in Temporal Lobe Epilepsy through Structural Connectome Based Simulations, *PLoS Comput. Biol.* 11 (2015) e1004642. <https://doi.org/10.1371/journal.pcbi.1004642>.
- [143] M. Goodfellow, C. Rummel, E. Abela, M.P. Richardson, K. Schindler, J.R. Terry, Estimation of brain network ictogenicity predicts outcome from epilepsy surgery, *Sci. Rep.*

- 6 (2016). <https://doi.org/10.1038/srep29215>.
- [144] T. Proix, F. Bartolomei, M. Guye, V.K. Jirsa, Individual brain structure and modelling predict seizure propagation, *Brain*. 140 (2017) 641–654.
<https://doi.org/10.1093/brain/awx004>.
- [145] N. Sinha, J. Dauwels, M. Kaiser, S.S. Cash, M.B. Westover, Y. Wang, P.N. Taylor, Predicting neurosurgical outcomes in focal epilepsy patients using computational modelling, *Brain*. 140 (2017) 319–332. <https://doi.org/10.1093/brain/aww299>.
- [146] A. Steimer, M. Müller, K. Schindler, Predictive modeling of EEG time series for evaluating surgery targets in epilepsy patients, *Hum. Brain Mapp.* 38 (2017) 2509–2531.
<https://doi.org/10.1002/hbm.23537>.
- [147] D.R. Nair, A. Mohamed, R. Burgess, H. Lüders, A critical review of the different conceptual hypotheses framing human focal epilepsy, *Epileptic Disord.* 6 (2004) 77–83.
<https://europepmc.org/article/med/15246951>.
- [148] H. Fujiwara, H.M. Greiner, K.H. Lee, K.D. Holland-Bouley, J.H. Seo, T. Arthur, F.T. Mangano, J.L. Leach, D.F. Rose, Resection of ictal high-frequency oscillations leads to favorable surgical outcome in pediatric epilepsy, *Epilepsia*. 53 (2012) 1607–1617.
<https://doi.org/10.1111/j.1528-1167.2012.03629.x>.
- [149] J. Jacobs, M. Zijlmans, R. Zelmann, C.É. Chatillon, J. Hall, A. Olivier, F. Dubeau, J. Gotman, High-frequency electroencephalographic oscillations correlate with outcome of epilepsy surgery, *Ann. Neurol.* 67 (2010) 209–220. <https://doi.org/10.1002/ana.21847>.
- [150] J. Jacobs, R. Staba, E. Asano, H. Otsubo, J.Y. Wu, M. Zijlmans, I. Mohamed, P. Kahane, F. Dubeau, V. Navarro, J. Gotman, High-frequency oscillations (HFOs) in clinical epilepsy, *Prog. Neurobiol.* 98 (2012) 302–315.
<https://doi.org/10.1016/j.pneurobio.2012.03.001>.
- [151] P.N. Modur, S. Zhang, T.W. Vitaz, Ictal high-frequency oscillations in neocortical epilepsy: Implications for seizure localization and surgical resection, *Epilepsia*. 52 (2011) 1792–1801. <https://doi.org/10.1111/j.1528-1167.2011.03165.x>.
- [152] H. Nariai, T. Nagasawa, C. Juhász, S. Sood, H.T. Chugani, E. Asano, Y. Nariai, T. Nagasawa, Y. Juhász, Z. Sood, T. Chugani, Y. Asano, Statistical mapping of ictal high-

- frequency oscillations in epileptic spasms, *Epilepsia*. 52 (2011) 63–74.
<https://doi.org/10.1111/j.1528-1167.2010.02786.x>.
- [153] A. Ochi, H. Otsubo, E.J. Donner, I. Elliott, R. Iwata, T. Funaki, Y. Akizuki, T. Akiyama, K. Imai, T. Rutka, O. Carter, S. Iii, J.T. Rutka, O.C. Snead, Dynamic changes of ictal high-frequency oscillations in neocortical epilepsy: Using multiple band frequency analysis, *Epilepsia*. 48 (2007) 286–296. <https://doi.org/10.1111/j.1528-1167.2007.00923.x>.
- [154] M. Zijlmans, P. Jiruska, R. Zelmann, F.S.S. Leijten, J.G.R. Jefferys, J. Gotman, High-frequency oscillations as a new biomarker in epilepsy, *Ann. Neurol*. 71 (2012) 169–178.
<https://doi.org/10.1002/ana.22548>.
- [155] D.J. Englot, L.B. Hinkley, N.S. Kort, B.S. Imber, D. Mizuiri, S.M. Honma, A.M. Findlay, C. Garrett, P.L. Cheung, M. Mantle, P.E. Tarapore, R.C. Knowlton, E.F. Chang, H.E. Kirsch, S.S. Nagarajan, Global and regional functional connectivity maps of neural oscillations in focal epilepsy, *Brain*. 138 (2015) 2249–2262.
<https://doi.org/10.1093/brain/awv130>.
- [156] B.C. Bernhardt, S. Hong, A. Bernasconi, N. Bernasconi, Imaging structural and functional brain networks in temporal lobe epilepsy, *Front. Hum. Neurosci*. 7 (2013).
<https://doi.org/10.3389/fnhum.2013.00624>.
- [157] A. Coito, G. Plomp, M. elanie Genetti, E. Abela, R. Wiest, M. Seeck, C.M. Michel, S. Vulliemoz, Dynamic directed interictal connectivity in left and right temporal lobe epilepsy, *Epilepsia*. 56 (2015) 207–217. <https://doi.org/10.1111/epi.12904>.
- [158] P. Besson, K. Bandt, T. Proix, S. Lagarde, V.K. Jirsa, J.-P. Ranjeva, F. Bartolomei, M. Guye, Anatomic consistencies across epilepsies: a stereotactic-EEG informed high-resolution structural connectivity study, *Brain*. 140 (2017) 2639–2652.
<https://doi.org/10.1093/brain/awx229>.
- [159] F. Wendling, F. Bartolomei, J.J.J. Bellanger, P. Chauvel, Interpretation of interdependencies in epileptic signals using a macroscopic physiological model of the EEG, *Clin. Neurophysiol*. 112 (2001) 1201–1218. [https://doi.org/10.1016/S1388-2457\(01\)00547-8](https://doi.org/10.1016/S1388-2457(01)00547-8).
- [160] F. Wendling, F. Bartolomei, J.J. Bellanger, J. Bourien, P. Chauvel, Epileptic fast

- intracerebral EEG activity: Evidence for spatial decorrelation at seizure onset, *Brain*. 126 (2003) 1449–1459. <https://doi.org/10.1093/brain/awg144>.
- [161] F. Bartolomei, F. Wendling, J. Régis, M. Gavaret, M. Guye, P. Chauvel, Pre-ictal synchronicity in limbic networks of mesial temporal lobe epilepsy, *Epilepsy Res.* 61 (2004) 89–104. <https://doi.org/10.1016/j.eplepsyres.2004.06.006>.
- [162] S.C.C. Ponten, F. Bartolomei, C.J.J. Stam, Small-world networks and epilepsy: Graph theoretical analysis of intracerebrally recorded mesial temporal lobe seizures, *Clin. Neurophysiol.* 118 (2007) 918–927. <https://www.sciencedirect.com/science/article/pii/S1388245706018438>.
- [163] M. Arthuis, L. Valton, J. Rgis, P. Chauvel, F. Wendling, L. Naccache, C. Bernard, F. Bartolomei, Impaired consciousness during temporal lobe seizures is related to increased long-distance corticocortical synchronization, *Brain*. 132 (2009) 2091–2101. <https://doi.org/10.1093/brain/awp086>.
- [164] M.A. Kramer, U.T. Eden, E.D. Kolaczyk, R. Zepeda, E.N. Eskandar, S.S. Cash, Coalescence and Fragmentation of Cortical Networks during Focal Seizures, *J. Neurosci.* 30 (2010) 10076–10085. <https://doi.org/10.1523/jneurosci.6309-09.2010>.
- [165] K. Schindler, H. Leung, C.E. Elger, K. Lehnertz, Assessing seizure dynamics by analysing the correlation structure of multichannel intracranial EEG, *Brain*. 130 (2007) 65–77. <https://doi.org/10.1093/brain/awl304>.
- [166] K.A. Schindler, S. Bialonski, M.-T.T. Horstmann, C.E. Elger, K. Lehnertz, Evolving functional network properties and synchronizability during human epileptic seizures, *Chaos*. 18 (2008) 033119. <https://doi.org/10.1063/1.2966112>.
- [167] K.K. Jerger, S.L. Weinstein, T. Sauer, S.J. Schiff, Multivariate linear discrimination of seizures, *Clin. Neurophysiol.* 116 (2005) 545–551. www.elsevier.com/locate/clinph.
- [168] P. Jiruska, M. de Curtis, J.G.R. Jefferys, C.A. Schevon, S.J. Schiff, K. Schindler, Synchronization and desynchronization in epilepsy: controversies and hypotheses, *J. Physiol.* 591 (2013) 787–797. <https://doi.org/10.1113/jphysiol.2012.239590>.
- [169] C. Rummel, M. Goodfellow, H. Gast, M. Hauf, F. Amor, A. Stibal, L. Mariani, R. Wiest, K. Schindler, A Systems-Level Approach to Human Epileptic Seizures, *Neuroinformatics*.

- 11 (2013) 159–173. <https://doi.org/10.1007/s12021-012-9161-2>.
- [170] K. Kaila, E. Ruusuvuori, P. Seja, J. Voipio, M. Puskarjov, GABA actions and ionic plasticity in epilepsy, *Curr. Opin. Neurobiol.* 26 (2014) 34–41. <https://doi.org/10.1016/j.conb.2013.11.004>.
- [171] F. Stief, W. Züschratter, K. Hartmann, D. Schmitz, A. Draguhn, Enhanced synaptic excitation-inhibition ratio in hippocampal interneurons of rats with temporal lobe epilepsy, *Eur. J. Neurosci.* 25 (2007) 519–528. <https://doi.org/10.1111/j.1460-9568.2006.05296.x>.
- [172] J.M. Fritschy, Epilepsy, E/I balance and GABA_A receptor plasticity, *Front. Mol. Neurosci.* 1 (2008) 5. <https://doi.org/10.3389/neuro.02.005.2008>.
- [173] A.K. Tryba, E.M. Merricks, S. Lee, T. Pham, S.J. Cho, D.R. Nordli, T.L. Eissa, R.R. Goodman, G.M. McKhann, R.G. Emerson, C.A. Schevon, W. Van Drongelen, Role of paroxysmal depolarization in focal seizure activity, *J. Neurophysiol.* 122 (2019) 1861–1873. <https://doi.org/10.1152/jn.00392.2019>.
- [174] S.A. Weiss, R. Staba, A. Bragin, K. Moxon, M. Sperling, M. Avoli, J. Engel, Interneurons and principal cell firing in human limbic areas at focal seizure onset, *Neurobiol. Dis.* 124 (2019) 183–188. <https://doi.org/10.1016/j.nbd.2018.11.014>.
- [175] M. Avoli, M. De Curtis, V. Gnatkovsky, J. Gotman, R. Köhling, M. Lévesque, F. Manseau, Z. Shiri, S. Williams, Specific imbalance of excitatory/inhibitory signaling establishes seizure onset pattern in temporal lobe epilepsy, *J. Neurophysiol.* 115 (2016) 3229–3237. <https://doi.org/10.1152/jn.01128.2015>.
- [176] J. Žiburkus, J.R. Cressman, S.J. Schiff, Seizures as imbalanced up states: Excitatory and inhibitory conductances during seizure-like events, *J. Neurophysiol.* 109 (2013) 1296–1306. <https://doi.org/10.1152/jn.00232.2012>.
- [177] Y. Liu, V. Grigorovsky, B. Bardakjian, Excitation and Inhibition Balance Underlying Epileptiform Activity, *IEEE Trans. Biomed. Eng.* 67 (2020) 2473–2481. <https://doi.org/10.1109/TBME.2019.2963430>.
- [178] L. Medrihan, E. Ferrea, B. Greco, P. Baldelli, F. Benfenati, Asynchronous GABA release is a key determinant of tonic inhibition and controls neuronal excitability: A study in the synapsin II^{-/-} mouse, *Cereb. Cortex.* 25 (2015) 3356–3368.

- <https://doi.org/10.1093/cercor/bhu141>.
- [179] A. Klaassen, J. Glykys, J. Maguire, C. Labarca, I. Mody, J. Boulter, Seizures and enhanced cortical GABAergic inhibition in two mouse models of human autosomal dominant nocturnal frontal lobe epilepsy, *Proc. Natl. Acad. Sci.* 103 (2006) 19152–19157. <https://doi.org/10.1073/pnas.0608215103>.
- [180] M. Helmstaedter, J.F. Staiger, B. Sakmann, D. Feldmeyer, Efficient recruitment of layer 2/3 interneurons by layer 4 input in single columns of rat somatosensory cortex, *J. Neurosci.* 28 (2008) 8273–8284. <https://doi.org/10.1523/JNEUROSCI.5701-07.2008>.
- [181] J.H.O. Hoffmann, H.S. Meyer, A.C. Schmitt, J. Straehle, T. Weitbrecht, B. Sakmann, M. Helmstaedter, Synaptic conductance estimates of the connection between local inhibitor interneurons and pyramidal neurons in layer 2/3 of a cortical column, *Cereb. Cortex.* 25 (2015) 4415–4429. <https://doi.org/10.1093/cercor/bhv039>.
- [182] T.J. Ellender, J. V. Raimondo, A. Irkle, K.P. Lamsa, C.J. Akerman, Excitatory effects of parvalbumin-expressing interneurons maintain hippocampal epileptiform activity via synchronous afterdischarges, *J. Neurosci.* 34 (2014) 15208–15222. <https://doi.org/10.1523/JNEUROSCI.1747-14.2014>.
- [183] I. Mody, Interneurons and the ghost of the sea, *Nat. Neurosci.* 1 (1998) 434–436. <https://doi.org/10.1038/2151>.
- [184] A. Bragin, P. Claeys, K. Vonck, D. Van Roost, C. Wilson, P. Boon, J. Engel, Analysis of Initial Slow Waves (ISWs) at the seizure onset in patients with drug resistant temporal lobe epilepsy, *Epilepsia.* 48 (2007) 1883–1894. <https://doi.org/10.1111/j.1528-1167.2007.01149.x>.
- [185] T.L. Babb, J.K. Pretorius, W.R. Kupfer, P.H. Crandall, Glutamate decarboxylase-immunoreactive neurons are preserved in human epileptic hippocampus, *J. Neurosci.* 9 (1989) 2562–2574. <https://doi.org/10.1523/jneurosci.09-07-02562.1989>.
- [186] I. Cohen, V. Navarro, S. Clemenceau, M. Baulac, R. Miles, On the origin of interictal activity in human temporal lobe epilepsy in vitro., *Science.* 298 (2002) 1418–21. <https://doi.org/10.1126/science.1076510>.
- [187] M. Avoli, Epileptiform discharges and a synchronous GABAergic potential induced by 4-

- aminopyridine in the rat immature hippocampus, *Neurosci. Lett.* 117 (1990) 93–98.
[https://doi.org/10.1016/0304-3940\(90\)90125-S](https://doi.org/10.1016/0304-3940(90)90125-S).
- [188] M. Avoli, C. Psarropoulou, V. Tancredi, Y. Fueta, On the synchronous activity induced by 4-aminopyridine in the CA3 subfield of juvenile rat hippocampus, *J. Neurophysiol.* 70 (1993) 1018–1029. <https://doi.org/10.1152/jn.1993.70.3.1018>.
- [189] V. Lopantsev, M. Avoli, Participation of GABA(A)-mediated inhibition in ictallike discharges in the rat entorhinal cortex, *J. Neurophysiol.* 79 (1998) 352–360.
<https://doi.org/10.1152/jn.1998.79.1.352>.
- [190] R. Benini, M. D’Antuono, E. Pralong, M. Avoli, Involvement of amygdala networks in epileptiform synchronization in vitro, *Neuroscience.* 120 (2003) 75–84.
[https://doi.org/10.1016/S0306-4522\(03\)00262-8](https://doi.org/10.1016/S0306-4522(03)00262-8).
- [191] M. Avoli, M. Barbarosie, A. Liicke, T. Nagao, V. Lopantsev, R. KGhling, Synchronous GABA-Mediated Potentials and Epileptiform Discharges in the Rat Limbic System In Vitro, *J. Neurosci.* 76 (1996) 3912–3924.
- [192] M. Barbarosie, J. Louvel, I. Kurcewicz, M. Avoli, CA3-released entorhinal seizures disclose dentate gyrus epileptogenicity and unmask a temporoammonic pathway, *J. Neurophysiol.* 83 (2000) 1115–1124. <https://doi.org/10.1152/jn.2000.83.3.1115>.
- [193] M. Barbarosie, J. Louvel, M. D’Antuono, I. Kurcewicz, M. Avoli, Masking synchronous GABA-mediated potentials controls limbic seizures, *Epilepsia.* 43 (2002) 1469–1479.
<https://doi.org/10.1046/j.1528-1157.2002.17402.x>.
- [194] I. Timofeev, F. Grenier, M. Steriade, The role of chloride-dependent inhibition and the activity of fast-spiking neurons during cortical spike-wave electrographic seizures, *Neuroscience.* 114 (2002) 1115–1132. [https://doi.org/10.1016/S0306-4522\(02\)00300-7](https://doi.org/10.1016/S0306-4522(02)00300-7).
- [195] A.J. Trevelyan, D. Sussillo, R. Yuste, Feedforward inhibition contributes to the control of epileptiform propagation speed, *J. Neurosci.* 27 (2007) 3383–3387.
<https://doi.org/10.1523/JNEUROSCI.0145-07.2007>.
- [196] M. Derchansky, D. Rokni, J.T. Rick, R. Wennberg, B.L. Bardakjian, L. Zhang, Y. Yarom, P.L. Carlen, Bidirectional multisite seizure propagation in the intact isolated hippocampus: The multifocality of the seizure “focus,” *Neurobiol. Dis.* 23 (2006) 312–328.

- <https://doi.org/10.1016/j.nbd.2006.03.014>.
- [197] J. Žiburkus, J.R. Cressman, E. Barreto, S.J. Schiff, Interneuron and pyramidal cell interplay during in vitro seizure- like events, *Early Hum. Dev.* 83 (2007) 255–262. <https://doi.org/10.1016/j.earlhumdev.2006.05.022>.
- [198] Y. Höller, J. Bergmann, M. Kronbichler, J.S. Crone, E.V. Schmid, S. Golaszewski, G. Ladurner, Preserved oscillatory response but lack of mismatch negativity in patients with disorders of consciousness, *Clin. Neurophysiol.* 122 (2011) 1744–1754. <https://doi.org/10.1016/j.clinph.2011.02.009>.
- [199] Z. Maglóczy, T.F. Freund, Impaired and repaired inhibitory circuits in the epileptic human hippocampus, *Trends Neurosci.* 28 (2005) 334–340. <https://doi.org/10.1016/j.tins.2005.04.002>.
- [200] F.E. Dudek, T.P. Sutula, Epileptogenesis in the dentate gyrus: a critical perspective, *Prog. Brain Res.* 163 (2007) 755–773. [https://doi.org/10.1016/S0079-6123\(07\)63041-6](https://doi.org/10.1016/S0079-6123(07)63041-6).
- [201] L. Williams, C. Bernard, R. Cossart, J.C. Hirsch, M. Esclapez, Y. Ben-Ari, What is GABAergic Inhibition? How Is it Modified in Epilepsy?, in: *Epilepsia*, Lippincott Williams and Wilkins, 2000: pp. S90–S95. <https://doi.org/10.1111/j.1528-1157.2000.tb01564.x>.
- [202] Z. Shiri, F. Manseau, M. Lévesque, S. Williams, M. Avoli, Interneuron activity leads to initiation of low-voltage fast-onset seizures, *Ann. Neurol.* 77 (2015) 541–546. <https://doi.org/10.1002/ana.24342>.
- [203] J. Engel, T.R. Henry, M.W. Risinger, J.C. Mazziotta, W.W. Sutherling, M.F. Levesque, M.E. Phelps, Presurgical evaluation for partial epilepsy: Relative contributions of chronic depth-electrode recordings versus fdg-pet and scalp-sphenoidal ictal eeg, *Neurology.* 40 (1990) 1670–1677. <https://doi.org/10.1212/wnl.40.11.1670>.
- [204] M. Lévesque, P. Salami, J. Gotman, M. Avoli, Two seizure-onset types reveal specific patterns of high-frequency oscillations in a model of temporal lobe epilepsy, *J. Neurosci.* 32 (2012) 13264–13272. <https://doi.org/10.1523/JNEUROSCI.5086-11.2012>.
- [205] A. Bragin, J. Engel, C.L. Wilson, E. Vizenin, G.W. Mathern, Electrophysiologic analysis of a chronic seizure model after unilateral hippocampal KA injection, *Epilepsia.* 40 (1999)

- 1210–1221. <https://doi.org/10.1111/j.1528-1157.1999.tb00849.x>.
- [206] Z.J. Zhang, J. Koifman, D.S. Shin, H. Ye, C.M. Florez, L. Zhang, T.A. Valiante, P.L. Carlen, Transition to seizure: Ictal discharge is preceded by exhausted presynaptic GABA release in the hippocampal CA3 region, *J. Neurosci.* 32 (2012) 2499–2512. <https://doi.org/10.1523/JNEUROSCI.4247-11.2012>.
- [207] M. Lévesque, P. Salami, C. Behr, M. Avoli, Temporal lobe epileptiform activity following systemic administration of 4-aminopyridine in rats, *Epilepsia.* 54 (2013) 596–604. <https://doi.org/10.1111/epi.12041>.
- [208] D. Boido, N. Jesuthasan, M. De Curtis, L. Uva, Network dynamics during the progression of seizure-like events in the hippocampal-parahippocampal regions, *Cereb. Cortex.* 24 (2014) 163–173. <https://doi.org/10.1093/cercor/bhs298>.
- [209] V. Gnatkovsky, L. Librizzi, F. Trombin, M. De Curtis, Fast activity at seizure onset is mediated by inhibitory circuits in the entorhinal cortex in vitro, *Ann. Neurol.* 64 (2008) 674–686. <https://doi.org/10.1002/ana.21519>.
- [210] B. Lasztóczy, G. Nyitrai, L. Héja, J. Kardos, Synchronization of GABAergic inputs to CA3 pyramidal cells precedes seizure-like event onset in juvenile rat hippocampal slices, *J. Neurophysiol.* 102 (2009) 2538–2553. <https://doi.org/10.1152/jn.91318.2008>.
- [211] D. Depannemaecker, A. Destexhe, V. Jirsa, C. Bernard, Modeling seizures: From single neurons to networks, *Seizure.* 90 (2021) 4–8. <https://doi.org/10.1016/j.seizure.2021.06.015>.
- [212] F. Lopes Da Silva, W. Blanes, S.N. Kalitzin, J. Parra, P. Suffczynski, D.N. Velis, Epilepsies as Dynamical Diseases of Brain Systems: Basic Models of the Transition between Normal and Epileptic Activity, *Epilepsia.* 44 (2003) 72–83. <https://doi.org/10.1111/j.0013-9580.2003.12005.x>.
- [213] R.A. Stefanescu, R.G.G. Shivakeshavan, S.S. Talathi, Computational models of epilepsy, *Seizure.* 21 (2012) 748–759. <https://doi.org/10.1016/j.seizure.2012.08.012>.
- [214] T. Proix, V.K. Jirsa, F. Bartolomei, M. Guye, W. Truccolo, Predicting the spatiotemporal diversity of seizure propagation and termination in human focal epilepsy, *Nat. Commun.* 9 (2018) 1–15. <https://doi.org/10.1038/s41467-018-02973-y>.

- [215] J. Creaser, C. Lin, T. Ridler, J.T. Brown, W. D'Souza, U. Seneviratne, M. Cook, J.R. Terry, K. Tsaneva-Atanasova, Domino-like transient dynamics at seizure onset in epilepsy, *PLoS Comput. Biol.* 16 (2020). <https://doi.org/10.1371/journal.pcbi.1008206>.
- [216] J.R. Cressman, G. Ullah, J. Ziburkus, S.J. Schiff, E. Barreto, The influence of sodium and potassium dynamics on excitability, seizures, and the stability of persistent states: I. Single neuron dynamics, *J. Comput. Neurosci.* 26 (2009) 159–170. <https://doi.org/10.1007/s10827-008-0132-4>.
- [217] A. Buchin, A. Chizhov, G. Huberfeld, R. Miles, B.S. Gutkin, Reduced efficacy of the KCC2 cotransporter promotes epileptic oscillations in a subiculum network model, *J. Neurosci.* 36 (2016) 11619–11633. <https://doi.org/10.1523/JNEUROSCI.4228-15.2016>.
- [218] K.H. Yang, P.J. Franaszczuk, G.K. Bergey, Inhibition modifies the effects of slow calcium-activated potassium channels on epileptiform activity in a neuronal network model, *Biol. Cybern.* 92 (2005) 71–81. <https://doi.org/10.1007/s00422-004-0532-0>.
- [219] M.L. Saggio, D. Crisp, J.M. Scott, P. Karoly, L. Kuhlmann, M. Nakatani, T. Murai, M. Dümpelmann, A. Schulze-Bonhage, A. Ikeda, M. Cook, S. V. Gliske, J. Lin, C. Bernard, V. Jirsa, W.C. Stacey, A taxonomy of seizure dynamotypes, *Elife.* 9 (2020) 1–56. <https://doi.org/10.7554/eLife.55632>.
- [220] H.R. Wilson, J.D. Cowan, A mathematical theory of the functional dynamics of cortical and thalamic nervous tissue, *Kybernetik.* 13 (1973) 55–80. <https://doi.org/10.1007/BF00288786>.
- [221] Y. Wang, A.J. Trevelyan, A. Valentin, G. Alarcon, P.N. Taylor, M. Kaiser, Mechanisms underlying different onset patterns of focal seizures, *PLoS Comput. Biol.* 13 (2017) 1–22. <https://doi.org/10.1371/journal.pcbi.1005475>.
- [222] P. Perucca, F. Dubeau, J. Gotman, Intracranial electroencephalographic seizure-onset patterns: Effect of underlying pathology, *Brain.* 137 (2014) 183–196. <https://doi.org/10.1093/brain/awt299>.
- [223] D. Jiménez-Jiménez, R. Nekkare, L. Flores, K. Chatzidimou, I. Bodi, M. Honavar, N. Mullatti, R.D.C. Elwes, R.P. Selway, A. Valentín, G. Alarcón, Prognostic value of intracranial seizure onset patterns for surgical outcome of the treatment of epilepsy, *Clin.*

- Neurophysiol. 126 (2015) 257–267. <https://doi.org/10.1016/j.clinph.2014.06.005>.
- [224] I. Soltesz, K. Staley, Computational Neuroscience in Epilepsy, Academic Press, 2008. <https://doi.org/10.1016/B978-0-12-373649-9.X5001-7>.
- [225] W. Löscher, R. Köhling, Functional, metabolic, and synaptic changes after seizures as potential targets for antiepileptic therapy, *Epilepsy Behav.* 19 (2010) 105–113. <https://doi.org/10.1016/j.yebeh.2010.06.035>.
- [226] F. Zubler, A. Steimer, H. Gast, K.A. Schindler, Seizure termination, *Int. Rev. Neurobiol.* 114 (2014) 187–207. <https://doi.org/10.1016/B978-0-12-418693-4.00008-X>.
- [227] D.A. McCormick, D. Contreras, On the cellular and network bases of epileptic seizures, *Annu. Rev. Physiol.* 63 (2001) 815–846. <https://doi.org/10.1146/annurev.physiol.63.1.815>.
- [228] C.M. O’Dell, A. Das, G. Wallace, S.K. Ray, N.L. Banik, Understanding the basic mechanisms underlying seizures in mesial temporal lobe epilepsy and possible therapeutic targets: A review, *J. Neurosci. Res.* 90 (2012) 913–924. <https://doi.org/10.1002/jnr.22829>.
- [229] E. Pereda, R.Q. Quiroga, J. Bhattacharya, Nonlinear multivariate analysis of neurophysiological signals, *Prog. Neurobiol.* 77 (2005) 1–37. <https://doi.org/10.1016/j.pneurobio.2005.10.003>.
- [230] J.P. Pijn, F. Lopes da Silva, Propagation of Electrical Activity: Nonlinear Associations and Time Delays between EEG Signals, in: *Basic Mech. EEG*, Birkhäuser Boston, 1993: pp. 41–61. https://doi.org/10.1007/978-1-4612-0341-4_4.
- [231] K. Ansari-Asl, L. Senhadji, J.-J. Bellanger, F. Wendling, Quantitative evaluation of linear and nonlinear methods characterizing interdependencies between brain signals, *Phys. Rev. E.* 74 (2006) 031916. <https://doi.org/10.1103/PhysRevE.74.031916>.
- [232] J.P. Lachaux, E. Rodriguez, J. Martinerie, F.J. Varela, R. Cameron, Measuring phase synchrony in brain signals, *Hum. Brain Mapp.* 8 (1999) 194–208. [https://doi.org/10.1002/\(SICI\)1097-0193\(1999\)8:4<194::AID-HBM4>3.0.CO;2-C](https://doi.org/10.1002/(SICI)1097-0193(1999)8:4<194::AID-HBM4>3.0.CO;2-C).
- [233] F. Mormann, K. Lehnertz, P. David, C. E. Elger, Mean phase coherence as a measure for phase synchronization and its application to the EEG of epilepsy patients, *Phys. D Nonlinear Phenom.* 144 (2000) 358–369. [https://doi.org/10.1016/S0167-2789\(00\)00087-7](https://doi.org/10.1016/S0167-2789(00)00087-7).

- [234] J.-P. Eckmann, S.O. Kamphorst, D. Ruelle, Recurrence Plots of Dynamical Systems, *Europhys. Lett.* 4 (1987) 973–977. <https://doi.org/10.1209/0295-5075/4/9/004>.
- [235] J.P. Zbilut, C.L. Webber, Embeddings and delays as derived from quantification of recurrence plots, *Phys. Lett. A.* 171 (1992) 199–203. [https://doi.org/10.1016/0375-9601\(92\)90426-M](https://doi.org/10.1016/0375-9601(92)90426-M).
- [236] J.P. Zbilut, C.L. Webber, Recurrence Quantification Analysis, *Wiley Encycl. Biomed. Eng.* (2006). <https://doi.org/10.1002/9780471740360.ebs1355>.
- [237] F. Takens, *Detecting strange attractors in turbulence*, Springer, Berlin, Heidelberg, 1981. <https://doi.org/10.1007/bfb0091924>.
- [238] A.M. Fraser, H.L. Swinney, Independent coordinates for strange attractors from mutual information, *Phys. Rev. A.* 33 (1986) 1134–1140. <https://doi.org/10.1103/PhysRevA.33.1134>.
- [239] L. Cao, Practical method for determining the minimum embedding dimension of a scalar time series, *Phys. D Nonlinear Phenom.* 110 (1997) 43–50. [https://doi.org/10.1016/S0167-2789\(97\)00118-8](https://doi.org/10.1016/S0167-2789(97)00118-8).
- [240] M.B. Kennel, R. Brown, H.D.I. Abarbanel, Determining embedding dimension for phase-space reconstruction using a geometrical construction, *Phys. Rev. A.* 45 (1992) 3403–3411. <https://doi.org/10.1103/PhysRevA.45.3403>.
- [241] N. Marwan, M.C. Romano, M. Thiel, J. Kurths, M. Carmen Romano, M. Thiel, J. Kurths, Recurrence plots for the analysis of complex systems, *Phys. Rep.* 438 (2007) 237–329. <https://doi.org/10.1016/J.PHYSREP.2006.11.001>.
- [242] N. Marwan, *Recurrence Plots At A Glance*, (2000). <http://www.recurrence-plot.tk/glance.php>.
- [243] M.C. Romano, M. Thiel, J. Kurths, W. von Bloh, Multivariate recurrence plots, *Phys. Lett. A.* 330 (2004) 214–223. <https://doi.org/10.1016/J.PHYSLETA.2004.07.066>.
- [244] J.P. Zbilut, A. Giuliani, C.L. Webber Jr., Recurrence quantification analysis as an empirical test to distinguish relatively short deterministic versus random number series, *Phys. Lett. A.* 267 (2000) 174–178. [https://doi.org/10.1016/S0375-9601\(00\)00098-0](https://doi.org/10.1016/S0375-9601(00)00098-0).

- [245] C. Mocenni, A. Facchini, A. Vicino, Comparison of recurrence quantification methods for the analysis of temporal and spatial chaos, *Math. Comput. Model.* 53 (2011) 1535–1545. <https://doi.org/10.1016/j.mcm.2010.04.008>.
- [246] J.P. Zbilut, C.L. Webber, *Recurrence Quantification Analysis*, Springer International Publishing, Cham, 2006. <https://doi.org/10.1002/9780471740360.ebs1355>.
- [247] G. Nolte, A. Ziehe, V. V. Nikulin, A. Schlögl, N. Krämer, T. Brismar, K.R. Müller, Robustly estimating the flow direction of information in complex physical systems, *Phys. Rev. Lett.* 100 (2008) 1–4. <https://doi.org/10.1103/PhysRevLett.100.234101>.
- [248] E.R. Kandel, J.H. Schwartz, T. Jessel, *Principles of Neural Science*, 4th edition, 2000.
- [249] G.J. Goodhill, M.Á. Carreira-Perpiñán, Cortical Columns, in: *Encycl. Cogn. Sci.*, John Wiley & Sons, Ltd, Chichester, 2006. <https://doi.org/10.1002/0470018860.s00356>.
- [250] J. Nolte, *The Human Brain. An Introduction to Its Functional Anatomy*, 6th Edition, J. Neuro-Ophthalmology. 30 (2010) 107. <https://doi.org/10.1097/01.wno.0000369168.32606.54>.
- [251] B.H. Jansen, V.G. Rit, Electroencephalogram and visual evoked potential generation in a mathematical model of coupled cortical columns, *Biol. Cybern.* 73 (1995) 357–366. <https://doi.org/10.1007/BF00199471>.
- [252] F.H. Lopes da Silva, A. Hoeks, H. Smits, L.H. Zetterberg, Model of brain rhythmic activity - The alpha-rhythm of the thalamus, *Kybernetik.* 15 (1974) 27–37. <https://doi.org/10.1007/BF00270757>.
- [253] F.H. Lopes da Silva, A. van Rotterdam, P. Barts, E. van Heusden, W. Burr, Models of Neuronal Populations: The Basic Mechanisms of Rhythmicity, *Prog. Brain Res.* 45 (1976) 281–308. [https://doi.org/10.1016/S0079-6123\(08\)60995-4](https://doi.org/10.1016/S0079-6123(08)60995-4).
- [254] A.L. Goldberger, D.R. Rigney, J. Mietus, E.M. Antman, S. Greenwald, Nonlinear dynamics in sudden cardiac death syndrome: Heart rate oscillations and bifurcations, *Experientia.* 44 (1988) 983–987. <https://doi.org/10.1007/BF01939894>.
- [255] L. Glass, D. Kaplan, Time series analysis of complex dynamics in physiology and medicine, *Med. Prog. Technol.* 19 (1993) 115–128.

- [256] N. Marwan, N. Wessel, U. Meyerfeldt, A. Schirdewan, J. Kurths, Recurrence-plot-based measures of complexity and their application to heart-rate-variability data, *Phys. Rev. E.* 66 (2002) 1–8. <https://doi.org/10.1103/PhysRevE.66.026702>.
- [257] N. Marwan, J. Kurths, Nonlinear analysis of bivariate data with cross recurrence plots, *Phys. Lett. A.* 302 (2002) 299–307. [https://doi.org/10.1016/S0375-9601\(02\)01170-2](https://doi.org/10.1016/S0375-9601(02)01170-2).
- [258] K. Shockley, M. Butwill, J.P. Zbilut, C.L. Webber, Cross recurrence quantification of coupled oscillators, *Phys. Lett. A.* 305 (2002) 59–69. [https://doi.org/10.1016/S0375-9601\(02\)01411-1](https://doi.org/10.1016/S0375-9601(02)01411-1).
- [259] J.P. Zbilut, A. Giuliani, C.L. Webber, Detecting deterministic signals in exceptionally noisy environments using cross-recurrence quantification, *Phys. Lett. A.* 246 (1998) 122–128. [https://doi.org/10.1016/S0375-9601\(98\)00457-5](https://doi.org/10.1016/S0375-9601(98)00457-5).
- [260] M.C. Casdagli, Recurrence plots revisited, *Phys. D Nonlinear Phenom.* 108 (1997) 12–44. [https://doi.org/10.1016/S0167-2789\(97\)82003-9](https://doi.org/10.1016/S0167-2789(97)82003-9).
- [261] H. Kantz, T. Schreiber, *Nonlinear time series analysis*, Cambridge University Press, 2001. <https://doi.org/10.1201/9780429109553-11>.
- [262] J. Kurths, H. Herzel, An attractor in a solar time series, *Phys. D Nonlinear Phenom.* 25 (1987) 165–172. [https://doi.org/10.1016/0167-2789\(87\)90099-6](https://doi.org/10.1016/0167-2789(87)90099-6).
- [263] D. Chakerian, B.B. Mandelbrot, The Fractal Geometry of Nature, *Coll. Math. J.* 15 (1984) 175. <https://doi.org/10.2307/2686529>.
- [264] A. Wolf, Estimating the dominant Lyapunov exponent from a Time Series, (1985) 1–25.
- [265] H.D.I. Abarbanel, R. Brown, J.J. Sidorowich, L.S. Tsimring, The analysis of observed chaotic data in physical systems, *Rev. Mod. Phys.* 65 (1993) 1331–1392. <https://doi.org/10.1103/RevModPhys.65.1331>.
- [266] D. Gribkov, V. Gribkova, Learning dynamics from nonstationary time series: Analysis of electroencephalograms, *Phys. Rev. E.* 61 (2000) 6538–6545. <https://doi.org/10.1103/PhysRevE.61.6538>.
- [267] F. Sylos Labini, A. Meli, Y.P. Ivanenko, D. Tufarelli, Recurrence quantification analysis of gait in normal and hypovestibular subjects, *Gait Posture.* 35 (2012) 48–55.

<https://doi.org/10.1016/J.GAITPOST.2011.08.004>.

- [268] J. Rolink, M. Kutz, P. Fonseca, X. Long, B. Misgeld, S. Leonhardt, Recurrence quantification analysis across sleep stages, *Biomed. Signal Process. Control.* 20 (2015) 107–116. <https://doi.org/10.1016/J.BSPC.2015.04.006>.
- [269] C.L. Webber, J.P. Zbilut, Dynamical assessment of physiological systems and states using recurrence plot strategies., *J. Appl. Physiol.* 76 (1994) 965–73. <https://doi.org/10.1152/jappl.1994.76.2.965>.
- [270] U. Großekathöfer, N. V. Manyakov, V. Mihajlović, G. Pandina, A. Skalkin, S. Ness, A. Bangerter, M.S. Goodwin, Automated Detection of Stereotypical Motor Movements in Autism Spectrum Disorder Using Recurrence Quantification Analysis, *Front. Neuroinform.* 11 (2017) 9. <https://doi.org/10.3389/fninf.2017.00009>.
- [271] C.L. Webber, N. Marwan, A. Facchini, A. Giuliani, Simpler methods do it better: Success of Recurrence Quantification Analysis as a general purpose data analysis tool, *Phys. Lett. A.* 373 (2009) 3753–3756. <https://doi.org/10.1016/J.PHYSLETA.2009.08.052>.
- [272] A. Facchini, C. Mocenni, N. Marwan, A. Vicino, E. Tiezzi, Nonlinear time series analysis of dissolved oxygen in the Orbetello Lagoon, *Ecol. Modell.* 203 (2007) 339–348. <https://doi.org/10.1016/j.ecolmodel.2006.12.001>.
- [273] J.M. Zaldívar, F. Strozzi, S. Dueri, D. Marinov, J.P. Zbilut, Characterization of regime shifts in environmental time series with recurrence quantification analysis, *Ecol. Modell.* 210 (2008) 58–70. <https://doi.org/10.1016/j.ecolmodel.2007.07.012>.
- [274] J.P. Zbilut, N. Thomasson, C.L. Webber, Recurrence quantification analysis as a tool for nonlinear exploration of nonstationary cardiac signals, *Med. Eng. Phys.* 24 (2002) 53–60. [https://doi.org/10.1016/S1350-4533\(01\)00112-6](https://doi.org/10.1016/S1350-4533(01)00112-6).
- [275] N. Marwan, A. Meinke, Extended recurrence plot analysis and its application to ERP data, *Int. J. Bifurcat. Chaos.* 14 (2004) 761–771. <https://doi.org/10.1142/S0218127404009454>.
- [276] K. Iwayama, Y. Hirata, K. Takahashi, K. Watanabe, K. Aihara, H. Suzuki, Characterizing global evolutions of complex systems via intermediate network representations, *Sci. Rep.* 2 (2012) 1–5. <https://doi.org/10.1038/srep00423>.

- [277] M.E.J. Newman, Fast algorithm for detecting community structure in networks, *Phys. Rev. E - Stat. Physics, Plasmas, Fluids, Relat. Interdiscip. Top.* 69 (2004) 5. <https://doi.org/10.1103/PhysRevE.69.066133>.
- [278] D.S. Bassett, M.A. Porter, N.F. Wymbs, S.T. Grafton, J.M. Carlson, P.J. Mucha, Robust detection of dynamic community structure in networks, *Chaos*. 23 (2013). <https://doi.org/10.1063/1.4790830>.
- [279] A. Buchin, C.C. Kerr, G. Huberfeld, R. Miles, B. Gutkin, Adaptation and inhibition control pathological synchronization in a model of focal epileptic seizure, *ENeuro*. 5 (2018) ENEURO.0019-18.2018. <https://doi.org/10.1523/ENEURO.0019-18.2018>.
- [280] M.A. Kramer, W. Truccolo, U.T. Eden, K.Q. Lepage, L.R. Hochberg, E.N. Eskandar, J.R. Madsen, J.W. Leek, A. Maheshwari, E. Halgren, C.J. Chu, S.S. Cash, Human seizures self-terminate across spatial scales via a critical transition, *Proc. Natl. Acad. Sci. U. S. A.* 109 (2012) 21116–21121. <https://doi.org/10.1073/pnas.1210047110>.
- [281] S.M. Kay, *Modern Spectral Estimation*, 12 (1988) 217–230. <https://doi.org/10.1038/nrn3008.A>.
- [282] P. Tass, M.G. Rosenblum, J. Weule, J. Kurths, A. Pikovsky, J. Volkmann, A. Schnitzler, H.J. Freund, Detection of n:m phase locking from noisy data: Application to magnetoencephalography, *Phys. Rev. Lett.* 81 (1998) 3291–3294. <https://doi.org/10.1103/PhysRevLett.81.3291>.
- [283] W. Truccolo, J.A. Donoghue, L.R. Hochberg, E.N. Eskandar, J.R. Madsen, W.S. Anderson, E.N. Brown, E. Halgren, S.S. Cash, Single-neuron dynamics in human focal epilepsy, *Nat. Neurosci.* 14 (2011) 635–643. <https://doi.org/10.1038/nn.2782>.
- [284] S. Noachtar, I. Borggraefe, Epilepsy surgery: A critical review, *Epilepsy Behav.* 15 (2009) 66–72. <https://doi.org/10.1016/j.yebeh.2009.02.028>.
- [285] S. Lagarde, F. Bonini, A. McGonigal, P. Chauvel, M. Gavaret, D. Scavarda, R. Carron, J. Régis, S. Aubert, N. Villeneuve, B. Giusiano, D. Figarella-Branger, A. Trebuchon, F. Bartolomei, Seizure-onset patterns in focal cortical dysplasia and neurodevelopmental tumors: Relationship with surgical prognosis and neuropathologic subtypes, *Epilepsia*. 57 (2016) 1426–1435. <https://doi.org/10.1111/epi.13464>.

- [286] K. Schindler, C.E. Elger, K. Lehnertz, Increasing synchronization may promote seizure termination: Evidence from status epilepticus, *Clin. Neurophysiol.* 118 (2007) 1955–1968. <https://www.sciencedirect.com/science/article/pii/S1388245707002957> (accessed April 29, 2019).
- [287] B. Wen, H. Qian, J. Feng, R.J. Ge, X. Xu, Z.Q. Cui, R.Y. Zhu, L.S. Pan, Z.P. Lin, J.H. Wang, A portion of inhibitory neurons in human temporal lobe epilepsy are functionally upregulated: An endogenous mechanism for seizure termination, *CNS Neurosci. Ther.* 21 (2015) 204–214. <https://doi.org/10.1111/cns.12336>.
- [288] F. Lado, How do seizures stop?, *Epilepsia.* 49 (2009) 1651–1664. <https://doi.org/10.1111/j.1528-1167.2008.01669.x>.How.
- [289] E. Evangelista, C. Bénar, F. Bonini, R. Carron, B. Colombet, J. Régis, F. Bartolomei, Does the thalamo-cortical synchrony play a role in seizure termination?, *Front. Neurol.* 6 (2015) 192. <https://doi.org/10.3389/fneur.2015.00192>.
- [290] C.P. Warren, S. Hu, M. Stead, B.H. Brinkmann, M.R. Bower, G.A. Worrell, Synchrony in normal and focal epileptic brain: The seizure onset zone is functionally disconnected, *J. Neurophysiol.* 104 (2010) 3530–3539. <https://doi.org/10.1152/jn.00368.2010>.
- [291] M.R. Bower, M. Stead, F.B. Meyer, W.R. Marsh, G.A. Worrell, Spatiotemporal neuronal correlates of seizure generation in focal epilepsy, *Epilepsia.* 53 (2012) 807–816. <https://doi.org/10.1111/j.1528-1167.2012.03417.x>.
- [292] M.A. Kramer, E.D. Kolaczyk, H.E. Kirsch, Emergent network topology at seizure onset in humans, *Epilepsy Res.* 79 (2008) 173–186. <https://doi.org/10.1016/j.eplepsyres.2008.02.002>.
- [293] J. Sun, X. Hong, S. Tong, Phase synchronization analysis of eeg signals: An evaluation based on surrogate tests, *IEEE Trans. Biomed. Eng.* 59 (2012) 2254–2263. <https://doi.org/10.1109/TBME.2012.2199490>.
- [294] A.J. Kim, M.M. Kuroda, D.R. Nordli, Abruptly attenuated terminal ictal pattern in pediatrics, *J. Clin. Neurophysiol.* 23 (2006) 532–550. <https://doi.org/10.1097/01.wnp.0000229045.28725.5c>.
- [295] M. de Curtis, M. Avoli, M. De Curtis, M. Avoli, Initiation, propagation, and termination of

- partial (Focal) seizures, *Cold Spring Harb. Perspect. Med.* 5 (2015) 1–16.
<https://doi.org/10.1101/cshperspect.a022368>.
- [296] D. Boido, V. Gnatkovsky, L. Uva, S. Francione, M. de Curtis, Simultaneous enhancement of excitation and postburst inhibition at the end of focal seizures, *Ann. Neurol.* 76 (2014) 826–836. <https://doi.org/10.1002/ana.24193>.
- [297] A. Destexhe, D.A. McCormick, T.J. Sejnowski, Thalamic and thalamocortical mechanisms underlying 3 Hz spike-and-wave discharges, *Prog. Brain Res.* 121 (2008) 289–307. [https://doi.org/10.1016/s0079-6123\(08\)63080-0](https://doi.org/10.1016/s0079-6123(08)63080-0).
- [298] M. Steriade, F. Amzica, D. Contreras, Cortical and thalamic cellular correlates of electroencephalographic burst-suppression, *Electroencephalogr. Clin. Neurophysiol.* 90 (1994) 1–16. [https://doi.org/10.1016/0013-4694\(94\)90108-2](https://doi.org/10.1016/0013-4694(94)90108-2).
- [299] N. Brunel, X.J. Wang, What determines the frequency of fast network oscillations with irregular neural discharges? I. Synaptic dynamics and excitation-inhibition balance, *J. Neurophysiol.* 90 (2003) 415–430. <https://doi.org/10.1152/jn.01095.2002>.
- [300] A. Ylinen, A. Bragin, Z. Nádasdy, G. Jandó, I. Szabó, A. Sik, G. Buzsáki, Sharp wave-associated high-frequency oscillation (200 Hz) in the intact hippocampus: Network and intracellular mechanisms, *J. Neurosci.* 15 (1995) 30–46.
<https://doi.org/10.1523/jneurosci.15-01-00030.1995>.
- [301] X.J. Wang, G. Buzsáki, Gamma oscillation by synaptic inhibition in a hippocampal interneuronal network model, *J. Neurosci.* 16 (1996) 6402–6413.
<https://doi.org/10.1523/jneurosci.16-20-06402.1996>.
- [302] P.J. Uhlhaas, W. Singer, High-frequency oscillations and the neurobiology of schizophrenia, *Dialogues Clin. Neurosci.* 15 (2013) 301–313.
<https://doi.org/10.31887/dcns.2013.15.3/puhlhaas>.
- [303] W.W. Lytton, T.J. Sejnowski, Simulations of cortical pyramidal neurons synchronized by inhibitory interneurons, *J. Neurophysiol.* 66 (2017) 1059–1079.
<https://doi.org/10.1152/jn.1991.66.3.1059>.
- [304] A.K. Ngugi, C. Bottomley, I. Kleinschmidt, J.W. Sander, C.R. Newton, Estimation of the burden of active and life-time epilepsy: A meta-analytic approach, *Epilepsia.* 51 (2010)

- 883–890. <https://doi.org/10.1111/j.1528-1167.2009.02481.x>.
- [305] P. Kwan, A. Arzimanoglou, A.T. Berg, M.J. Brodie, W.A. Hauser, G. Mathern, S.L. Moshé, E. Perucca, S. Wiebe, J. French, Definition of drug resistant epilepsy: Consensus proposal by the ad hoc Task Force of the ILAE Commission on Therapeutic Strategies, *Epilepsia*. 51 (2010) 1069–1077. <https://doi.org/10.1111/j.1528-1167.2009.02397.x>.
- [306] A.T. Berg, M.M. Kelly, Defining intractability: Comparisons among published definitions, *Epilepsia*. 47 (2006) 431–436. <https://doi.org/10.1111/j.1528-1167.2006.00440.x>.
- [307] Y. Wang, M. Goodfellow, P.N. Taylor, G. Baier, Dynamic Mechanisms of Neocortical Focal Seizure Onset, *PLoS Comput. Biol.* 10 (2014). <https://doi.org/10.1371/journal.pcbi.1003787>.
- [308] B.H. Jansen, G. Zouridakis, M.E. Brandt, A neurophysiologically-based mathematical model of flash visual evoked potentials., *Biol. Cybern.* 68 (1993) 275–83. <http://www.ncbi.nlm.nih.gov/pubmed/8452897> (accessed May 16, 2019).
- [309] L.A. Shokooh, D.H. Toffa, P. Pouliot, F. Lesage, D.K. Nguyen, Intracranial EEG seizure onset and termination patterns and their association, *Epilepsy Res.* 176 (2021) 106739. <https://doi.org/10.1016/j.eplepsyres.2021.106739>.
- [310] H.G.E. Meijer, T.L. Eissa, B. Kiewiet, J.F. Neuman, C.A. Schevon, R.G. Emerson, R.R. Goodman, G.M. McKhann, C.J. Marcuccilli, A.K. Tryba, J.D. Cowan, S.A. van Gils, W. van Drongelen, Modeling focal epileptic activity in the Wilson-Cowan model with depolarization block, *J. Math. Neurosci.* 5 (2015) 7. <https://doi.org/10.1186/s13408-015-0019-4>.
- [311] D. Bianchi, A. Marasco, A. Limongiello, C. Marchetti, H. Marie, B. Tirozzi, M. Migliore, On the mechanisms underlying the depolarization block in the spiking dynamics of CA1 pyramidal neurons, *J. Comput. Neurosci.* 33 (2012) 207–225. <https://doi.org/10.1007/s10827-012-0383-y>.
- [312] C.M. Kim, D.Q. Nykamp, The influence of depolarization block on seizure-like activity in networks of excitatory and inhibitory neurons, *J. Comput. Neurosci.* 43 (2017) 65–79. <https://doi.org/10.1007/s10827-017-0647-7>.
- [313] J. Ziburkus, J.R. Cressman, E. Barreto, S.J. Schiff, Interneuron and pyramidal cell

- interplay during in vitro seizure-like events, *J. Neurophysiol.* 95 (2006) 3948–3954.
<https://doi.org/10.1152/jn.01378.2005>.
- [314] G.S. Yi, J. Wang, K.M. Tsang, X. Le Wei, B. Deng, Biophysical insights into how spike threshold depends on the rate of membrane potential depolarization in Type I and Type II neurons, *PLoS One.* 10 (2015). <https://doi.org/10.1371/journal.pone.0130250>.
- [315] I. Toyoda, S. Fujita, A.K. Thamattoor, P.S. Buckmaster, Unit activity of hippocampal interneurons before spontaneous seizures in an animal model of temporal lobe epilepsy, *J. Neurosci.* 35 (2015) 6600–6618. <https://doi.org/10.1523/JNEUROSCI.4786-14.2015>.
- [316] O.J. Ahmed, M.A. Kramer, W. Truccolo, J.S. Naftulin, N.S. Potter, E.N. Eskandar, G.R. Cosgrove, A.S. Blum, L.R. Hochberg, S.S. Cash, Inhibitory single neuron control of seizures and epileptic traveling waves in humans, *BMC Neurosci.* 15 (2014) 2202. <https://doi.org/10.1186/1471-2202-15-S1-F3>.
- [317] L. Yekhleif, G.L. Breschi, S. Taverna, Optogenetic activation of VGLUT2-expressing excitatory neurons blocks epileptic seizure-like activity in the mouse entorhinal cortex, *Sci. Rep.* 7 (2017) 1–12. <https://doi.org/10.1038/srep43230>.
- [318] E.H. Kossoff, E.K. Ritzl, J.M. Politsky, A.M. Murro, J.R. Smith, R.B. Duckrow, D.D. Spencer, G.K. Bergey, Effect of an External Responsive Neurostimulator on Seizures and Electrographic Discharges during Subdural Electrode Monitoring, *Epilepsia.* 45 (2004) 1560–1567. <https://doi.org/10.1111/J.0013-9580.2004.26104.X>.
- [319] Y.D. Park, A.M. Murro, D.W. King, B.B. Gallagher, J.R. Smith, F. Yaghmai, The significance of ictal depth EEG patterns in patients with temporal lobe epilepsy, *Electroencephalogr. Clin. Neurophysiol.* 99 (1996) 412–415.
[https://doi.org/10.1016/S0013-4694\(96\)95120-2](https://doi.org/10.1016/S0013-4694(96)95120-2).
- [320] K. Boonyapisit, I. Najm, G. Klem, Z. Ying, C. Burrier, E. LaPresto, D. Nair, W. Bingaman, R. Prayson, H. Lüders, Epileptogenicity of focal malformations due to abnormal cortical development: Direct electrocorticographic-histopathologic correlations, *Epilepsia.* 44 (2003) 69–76. <https://doi.org/10.1046/j.1528-1157.2003.08102.x>.
- [321] R. Enatsu, Z. Piao, T. O'Connor, K. Horning, J. Mosher, R. Burgess, W. Bingaman, D. Nair, Cortical excitability varies upon ictal onset patterns in neocortical epilepsy: A

- cortico-cortical evoked potential study, *Clin. Neurophysiol.* 123 (2012) 252–260.
<https://doi.org/10.1016/j.clinph.2011.06.030>.
- [322] P.D. Welch, The Use of Fast Fourier Transform for the Estimation of Power Spectra: A Method Based on Time Averaging Over Short, Modified Periodograms, *IEEE Trans. Audio Electroacoust.* 15 (1967) 70–73. <https://doi.org/10.1109/TAU.1967.1161901>.
- [323] S. Fortunato, Community detection in graphs, *Phys. Rep.* 486 (2010) 75–174.
<https://doi.org/10.1016/j.physrep.2009.11.002>.
- [324] M.E.J. Newman, Modularity and community structure in networks, 103 (2006) 8577–8582. <https://doi.org/10.1073/pnas.0601602103>.
- [325] M.E.J. Newman, M. Girvan, Finding and evaluating community structure in networks, *Phys. Rev. E - Stat. Nonlinear, Soft Matter Phys.* 69 (2004) 1–15.
<https://doi.org/10.1103/PhysRevE.69.026113>.
- [326] S. Fortunato, M. Barthélemy, Resolution limit in community detection, *Proc. Natl. Acad. Sci. U. S. A.* 104 (2007) 36–41. <https://doi.org/10.1073/pnas.0605965104>.
- [327] H.-O. Peitgen, H. (Hartmut) Jürgens, D. Saupe, *Chaos and fractals : new frontiers of science*, Springer, 2004.
- [328] U. Simonsohn, L.D. Nelson, J.P. Simmons, P-curve: A key to the file-drawer, *J. Exp. Psychol. Gen.* 143 (2014) 534–547. <https://doi.org/10.1037/a0033242>.
- [329] M.I. Banks, J.A. White, R.A. Pearce, Interactions between Distinct GABAA Circuits in Hippocampus, *Neuron.* 25 (2000) 449–457. [https://doi.org/10.1016/S0896-6273\(00\)80907-1](https://doi.org/10.1016/S0896-6273(00)80907-1).

APPENDIX A

Patient-specific frequency bands

Using Welch's method for 1 s time-windows with 75% overlap the power spectrum was calculated [322] and averaged over interictal and ictal recordings which resulted in the average ictal and interictal spectra (P_{int} and P_{ict} respectively). In the next step, the r-spectrum was calculated as follows:

$$R = \frac{P_{ict}}{P_{int}} \quad (A1)$$

Finally, for each patient, we calculated the averaged r-spectrum for Delta (1-4 Hz), Theta (5-8 Hz), Alpha (9-13 Hz), Beta (14-25 Hz), Gamma (25-120) and identified the frequency band with the largest r-spectrum [1] (Fig. A1).

State identification and resolution parameter

To identify the global states, we partitioned the configuration similarity matrix into communities. The communities were detected by optimizing an objective function known as modularity (Eq. A2) [323–325]. This function compares the density of links in communities with the links between the communities.

$$Q = \frac{1}{2m} \sum_{i,j} \left[A_{ij} - \gamma \frac{k_i k_j}{2m} \right] \delta(c_i, c_j). \quad (A2)$$

Here, A_{ij} denotes the weight of the edge between i and j and $k_i = \sum_j A_{ij}$ calculates the overall weights of the edges attached to i and $m = \frac{1}{2} \sum_{i,j} A_{ij}$. The community that includes the node i , is shown by C_i . $\delta(c_i, c_j)$ is defined as follows:

$$\begin{cases} \delta(c_i, c_j) = 1 & \text{if } c_i = c_j \\ \delta(c_i, c_j) = 0 & \text{otherwise} \end{cases} \quad (A3)$$

In this algorithm, for a network with N nodes, we start with associating a community to each node of the network. Then, we calculate the gain of modularity by assigning each node i to its neighboring community j . Node i is finally placed in the community which maximizes the gain. We repeatedly do the previous step for all nodes until the modularity obtains no more improvement. As the modularity optimization cannot detect communities smaller than a scale -depending on the

total size of the network and its interconnections- the resolution parameter γ is introduced [326]. The resolution parameter γ for which the rate of change for modularity decreases is considered as optimal [278]. Therefore, to find the optimal γ , we detected the inflection point on the modularity vs γ plots [2]. Fig. A1 represents the calculated optimal resolution parameter (γ) that was applied within different approaches. Our results for method I, II and III showed no significant difference for the measured optimal resolution parameter among the ictal, pre- and post-ictal periods (p-value >0.05) while method IV showed significantly higher values during ictal period compared to pre-ictal period (p-value <0.001).

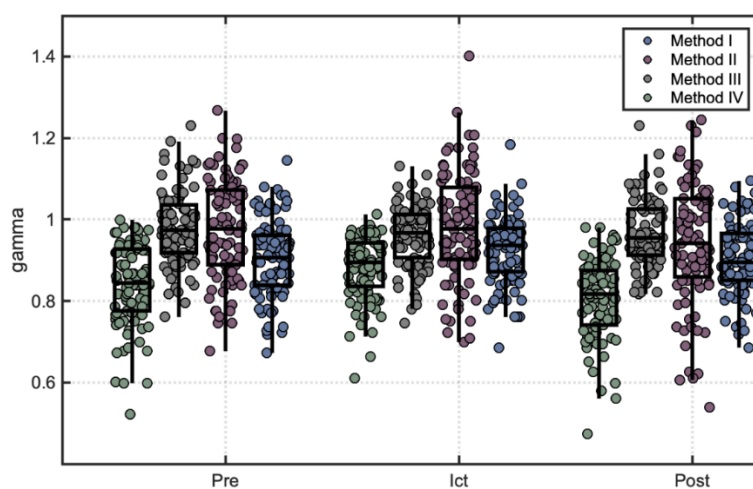


Figure A1 The optimal resolution parameter gamma (γ) used for state identification in methods I, II, III and IV for the pre-ictal, ictal and post-ictal periods.

Reconstructing the phase space

We can reconstruct the phase space from the observations of the system. A well-known example of a three-dimensional chaotic dynamical system is the Rössler system. In this example, the phase space is first constructed from the system equations and then it will be reconstructed from the time series of just one coordinate of the system. We will see that the two phase-spaces represent the same dynamic; however, for the construction of the later, we do not require the underlying equations.

The Rössler system is a set of three ordinary differential equations as follow [327]:

$$\begin{cases} x = -(y + z) \\ y = x + 0.2y \\ z = 0.2 + xz - 0.57z \end{cases} . \quad (\text{A4})$$

Solving Eq. A4, we obtain the trajectories in the phase space as depicted in Fig. A2.

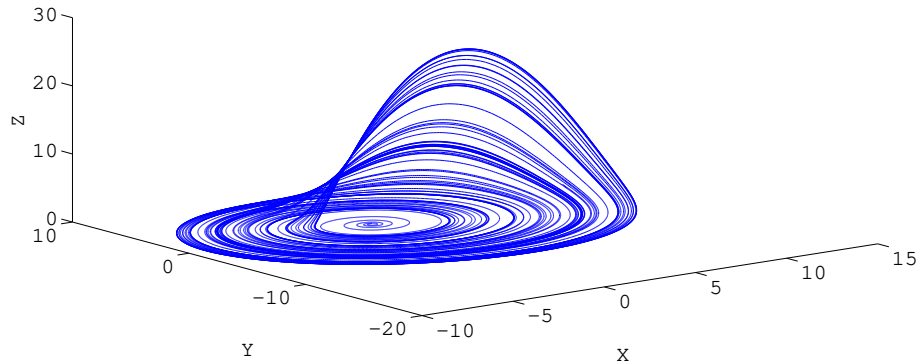


Figure A2 Reconstructing phase space for Rössler system from its equations

Takens theorem [237], indicates that it is possible to reconstruct the attractor from the time series without knowledge of the underlying dynamics. To achieve this, we require three quantities that can produce a phase space representation of system dynamics. One possible set of such quantities is the value of the coordinate with its values at two previous times, e.g. $x(t), x(t - \tau), x(t - 2\tau)$. Fig. A2 shows the two-dimensional representation of this reconstruction.

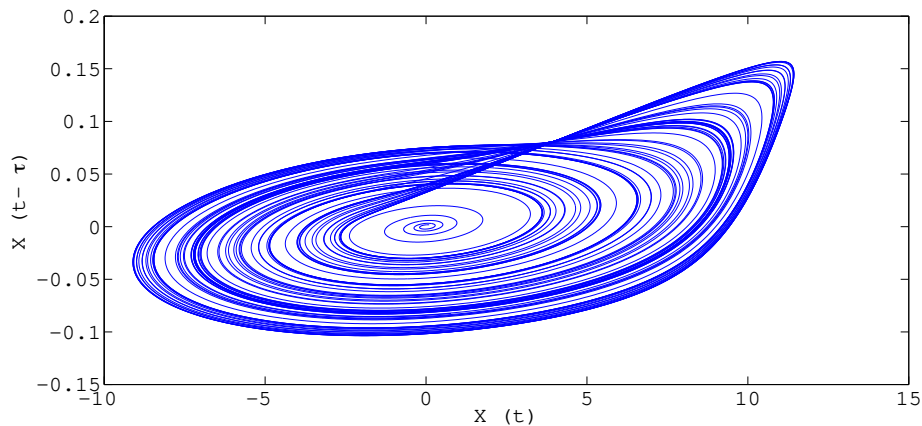
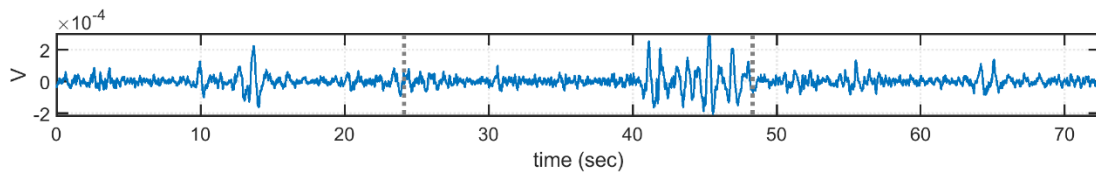


Figure A3 Reconstructing phase space for the Rössler system from X time series

By comparing Fig. A2 and Fig. A3 we can see that the geometrical form of the attractor stays intact (they show similar dynamical parameters like Lyapunov exponents and correlation dimension). This indicates an example of the possibility of studying the dynamical characteristics of a system based on an observed time series of that system. The above example provides the basic framework for reconstructing the phase space of an unknown dynamics from time-series data. However, for a time series from experimental observation, we have no prior knowledge about the number of dimensions required and the appropriate time delay. Techniques to obtain these parameters are provided below.

a)



b)

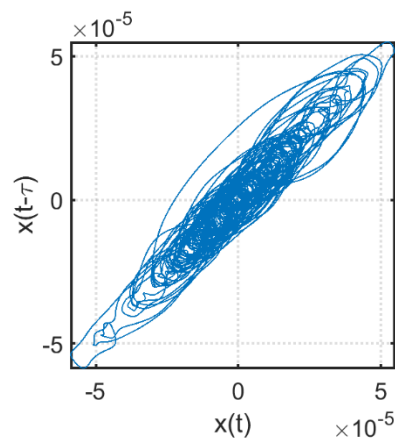


Figure A4 a) Recorded signal from one EEG channel for one patient. Gray lines depict seizure onset and offset. b) Phase space reconstruction from the ictal period of the signal represented in (a).

Finding the time delay

The mutual information of $x(t)$ and $x(t + \tau)$ gives us the information we can gain about $x(t + \tau)$ if we know $x(t)$ and the first minimum of it indicates the time lag for which $x(t + \tau)$ adds the maximum information to what we know from $x(t)$. Based on this idea using Shannon's entropy, Fraser et al. [238] presented an algorithm to obtain the time delay for the phase space reconstruction. Note that for large τ , $x(t)$ and $x(t + \tau)$ become decorrelated and the mutual information is zero.

Finding the embedding dimension

After finding the optimum time lag, we estimate the embedding dimension to reconstruct the time delay vectors in the form of:

$$y = (x_i, x_{i+m_0}, \dots, x_{i+m_0(d-1)}). \quad (A5)$$

In Eq. A5, d is the embedding dimension and x represents the time series data points. If d is a true dimension for the system, then the points which are close to each other in the d dimensional phase space are also neighbors in $d + 1$ dimension phase space and any two points fulfilling this condition are called true neighbors [239]. Based on this idea, Kennel et al. [240] have proposed the false nearest neighbor algorithm for determining the embedding dimension. This algorithm starts from a low value for the system dimension and finds false neighbors repeatedly until the number of false neighbors becomes zero. The dimension at which the number of false neighbors becomes zero is considered as the embedding dimension.

By calculating the time delay and embedding dimension, we can reconstruct the phase space.

The calculated embedding dimensions and time delays used in constructing the averaged over all channels for each seizure is represented in Fig. A5. As we can see in this figure, the averaged embedding dimension for both SF and NSF patients was significantly higher for the ictal period comparing the pre-ictal (p-value<0.05) and post-ictal (p-value<0.001) periods. The average time delay was significantly lower during the ictal period in comparison to both pre- and post-ictal periods for SF patients (p-value<0.05 and p-values<0.001 respectively) and only to the post-ictal period for NSF patients (p-value<0.001).

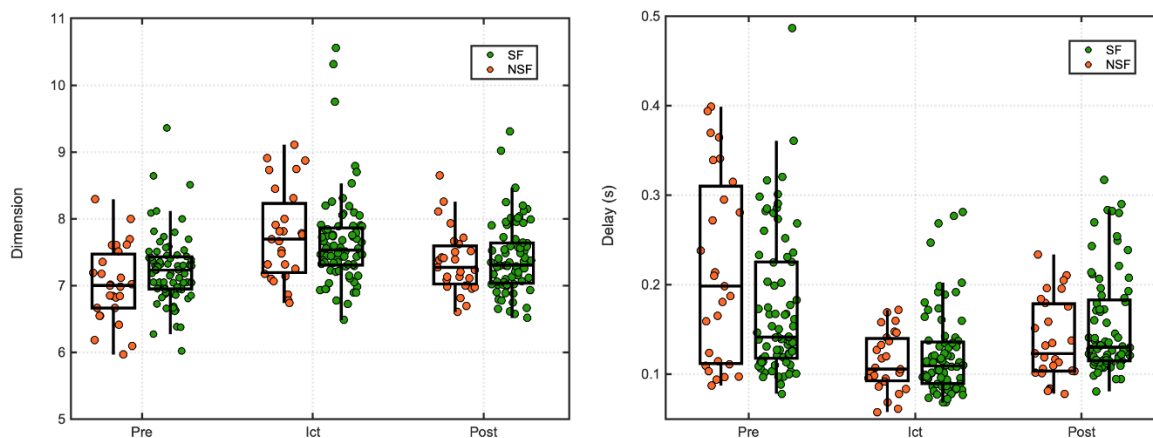


Figure A5 Embedding dimension and time delay calculated using false nearest neighbor and minimum mutual information and averaged over all channels for each seizure. The averaged embedding dimension for both SF and NSF patients was significantly higher for the ictal period comparing the pre-ictal (p -value <0.05) and post-ictal (p -value <0.001) periods. The averaged time delay was significantly lower during the ictal period in comparison to both pre- and post-ictal periods for SF patients (with p -values less than 0.05 and 0.001 respectively) and only to the post-ictal period for NSF patients (p -value <0.001).

Global and local measures calculated for all patients

While in the main text, the dynamic of global and local measures was reported separately for SF and NSF patients, herein we further investigated them for all patients.

As shown in Fig. S6, using all the methods, the state transition rates were lower during the ictal period compared to pre- and post-ictal periods. Tables S1 a and b, respectively, show the results from ANOVA and post-hoc analysis.

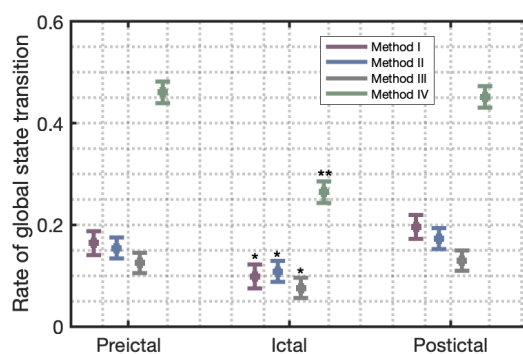


Figure A6 Rate of global state transition for all patients. The lines show 95% confidence intervals. * and ** denote p -value <0.05 and p -value <0.001 respectively compared to both pre- and post-ictal

periods. Our results indicated significantly lower global state transition rates for the ictal epoch compared to both pre- and post-ictal epochs (p-values_{adj} are represented in Table S1).

Table A1 a) Comparing global state transition rates between pre-ictal, ictal and post-ictal periods using one-way ANOVA conducted separately for all patients.

	<i>Method I</i>	<i>Method II</i>	<i>Method III</i>	<i>Method IV</i>
<i>F</i>	$F(2,303)=12.26$	$F(2,303)=7.07$	$F(2,303)=5.77$	$F(2,303)=77.31$
<i>P-values</i>	$7.5e-6$	$9.9e-4$	0.0035	$7.4e-28$

Table A1 b) The adjusted p-values (p-value_{adj}) based on the post-hoc analysis using Tukey-Kramer test to control for the family-wise error rate of 5% (FWER = 5%).

	<i>Method I</i>	<i>Method II</i>	<i>Method III</i>	<i>Method IV</i>
<i>Pre-ictal</i>	0.0031	0.0247	0.0133	$9.5e-10$
<i>Post-ictal</i>	$3.5e-6$	$7.6e-4$	0.0059	$9.5e-10$

The dynamic of the local measures (DET and LAM) for all patients (SF and NSF) is presented in Fig. A7. Table A2 represents the ANOVA and post-hoc analysis results. The same analysis is conducted separately for SF and NSF patients in the main text.

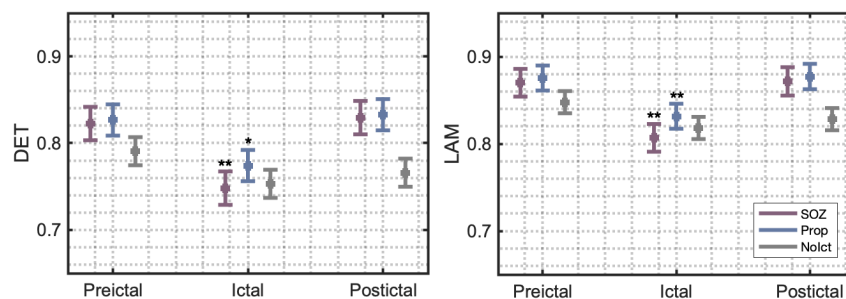


Figure A7 RQA measures for all patients (SF and NSF) averaged over three different channel groups (seizure onset channels (SOZ), the channels to which the seizure propagated within the first 10s of ictal activity (Prop) and the channels with no ictal activity during the seizure (NoIct)). Both DET and LAM showed a significant decrease during the ictal period compared to pre- and post-ictal periods for SOZ (p-values_{adj}<0.001) and Prop group (p-value_{adj} less than 0.05 and 0.001 for DET and LAM respectively). However, for the NoIct group, the decrease was only significant when compared to the pre-ictal epoch (p-value_{adj}<0.05) (the ANOVA results and p-values_{adj} are represented in Table A2).

Table A2 a) Calculated p-values for RQA measures for all patients (SF and NSF) using one-way ANOVA.

	DET			LAM		
	SOZ	Prop	NoIct	SOZ	Prop	NoIct
<i>F</i>	$F(2,291)=15.03$	$F(2,279)=8.80$	$F(2,159)=3.82$	$F(2,287)=14.68$	$F(2,276)=8.88$	$F(2,159)=3.83$
<i>P-values</i>	$6.09e-7$	$1.95e-4$	0.0239	$8.5e-7$	$1.82e-4$	0.0237

Table A2 b) The adjusted p-values (p-value_{adj}) based on the post-hoc analysis using Tukey-Kramer test to control for the family-wise error rate of 5% (FWER = 5%).

	DET			LAM		
	SOZ	Prop	NoIct	SOZ	Prop	NoIct
<i>Pre-ictal</i>	$1.76e-5$	0.0018	0.0180	$9.77e-6$	$9.63e-4$	0.0177
<i>Post-ictal</i>	$2.31e-6$	$3.97e-4$	0.6241	$7.20e-6$	$6.33e-4$	0.6211

P-value distribution

The database of this study consisted of 75 seizures from SF patients and 26 seizures from NSF patients. In order to investigate whether our findings for the comparison between SF and NSF patients remained unchanged with equal sample sizes, random samples from the SF group were selected with the same size as the available number of seizures from the NSF group (26 seizures). Then, we conducted the statistical analysis as described in section 2.3.4 of the main text, compared our global and local measures between SF and NSF groups, and calculated the p-values. We performed this analysis for 100 iterations and studied the distribution of the p-values (the number of iterations did not affect our findings as we obtained the same results with 1000 iterations as well).

The uniform p-value distribution indicates that the null hypothesis is true while the right-skewed (more weighted towards 0) p-values distribution shows that the null hypothesis is false [328]. More specifically, this method [328] treats p values as test statistics themselves and uses Fisher's method to find the statistically significant right-skewed p-value distributions ($pp < 0.05$).

As we can see in Fig. S8, our results for the global state transition rates displayed uniform distribution ($pp > 0.05$), suggesting insignificant difference in global state transition rates between SF and NSF patients. These results are consistent with our findings for unbalanced SF and NSF sample sizes.

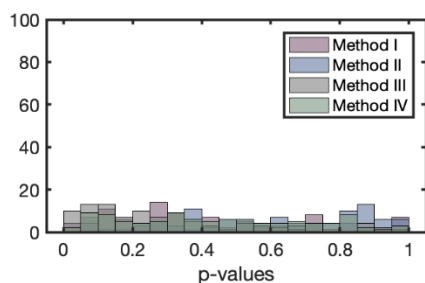


Figure A8 the distribution of p-values calculated based on the comparison of ictal global state transition rates between SF and NSF patients with equal sample sizes and 100 test iterations.

Our findings for both DET and LAM showed right-skewed p-value distributions. Fig. S10, displays the number of tests with p-values equal to 0.01, 0.02, 0.03, 0.04 and 0.05 for SOZ, Prop and NoIct channel groups. The p-value distribution was only significantly right-skewed for the SOZ channel group ($p < 0.05$).

Here, our findings based on equal SF and NSF sample sizes agree with our results based on unbalanced sample sizes reported in the main text.

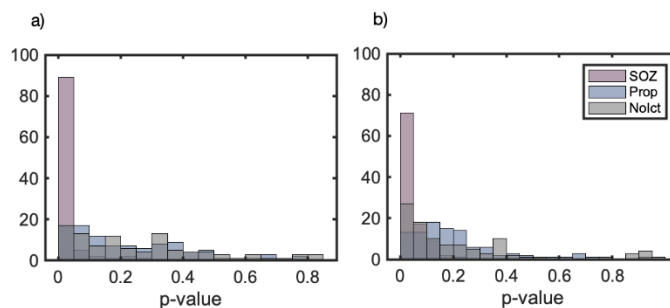


Figure A9 The distribution of p-values calculated based on the comparison of ictal DET (a) and LAM (b) between SF and NSF patients with equal sample sizes and 100 test iterations.

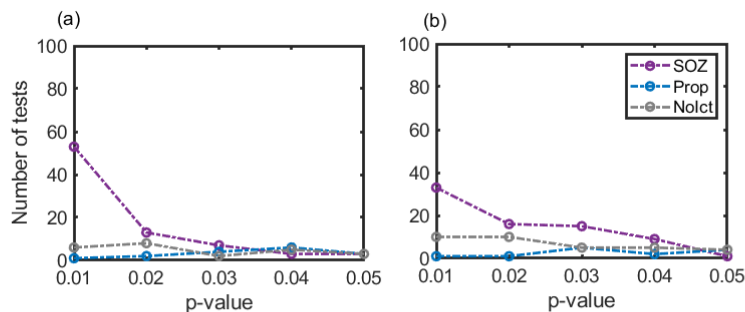


Figure A10 The number of tests with p-values equal to 0.01, 0.02, 0.03, 0.04 and 0.05 for the comparison of ictal DET (a) and LAM (b) between SF and NSF patients.

APPENDIX B

Onset patterns observed using the epicortical vs. intracortical recordings.

The proportion of seizures with different onset patterns for both epicortical and intracortical recordings are presented in Fig.B1. The most noticeable difference between these two groups is the absence of HAFA onset patterns recorded using intracortical implantation. This observation could suggest that the HAFA onset pattern does not originate from deep brain regions; however, it should be further verified using a larger database.

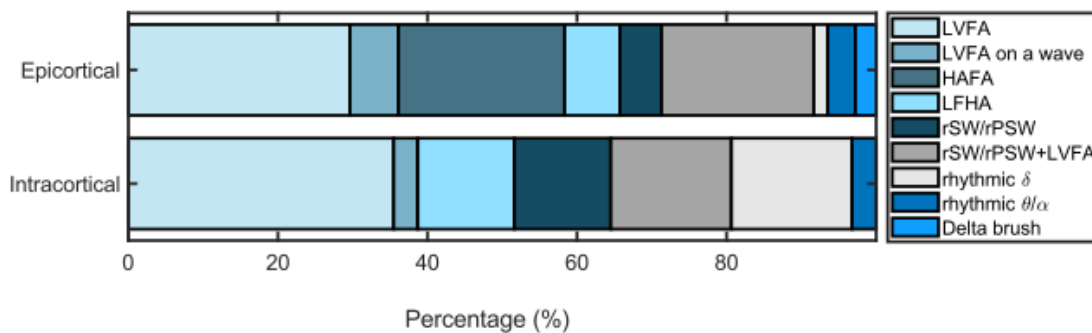


Figure B1 The percentage of different seizure onset patterns recorded using epicortical and intracortical implantation approaches.

The association between inter-channel distances and the functional connectivity measures

To investigate the effect of interchannel distances on our functional connectivity measures, we calculated the Pearson's correlation coefficients between the functional connectivity values and the Euclidean distances between all contacts. As presented in Fig.B2 the low Pearson's correlation coefficients (r) across all frequency bands ($\text{mean}(\text{abs}(r)) = 0.019$, $\text{min}(r) = -0.096$, $\text{max}(r) = 0.060$, $\sigma(r) = 0.024$) suggest that the functional connectivity values could not be associated with the channel locations. The distribution of these Pearson's correlation coefficients (r) is also depicted in Fig.B3.

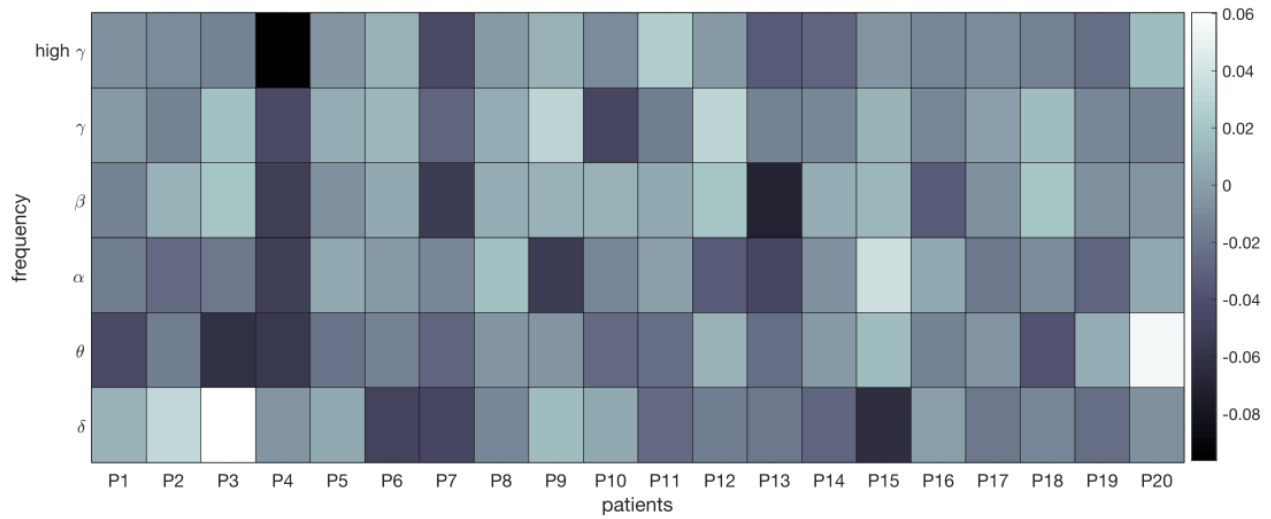


Figure B2 Pearson's correlation coefficients between the functional connectivity measures and the Euclidean distance between all channels and across all frequency bands.

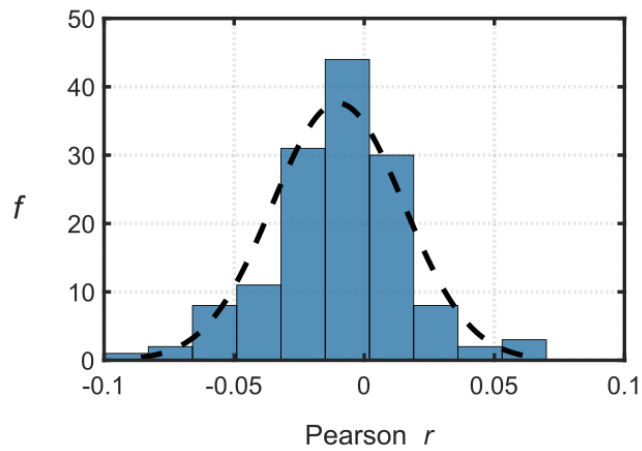


Figure B3 The distribution of Pearson's correlation coefficients between the functional connectivity measures and the Euclidean distance between all channels and across all frequency bands.

APPENDIX C

Our model is comprised of four neural populations: pyramidal cells, excitatory interneurons, dendrite targeting inhibitory interneurons and soma targeting inhibitory interneurons. In this model, based on [112], we have considered two types of inhibitory interneurons to account for two types of GABAergic inhibitions: the soma targeting inhibition with fast dynamics and dendrite targeting inhibition with slow dynamics. Based on the experimental studies dendrite targeting interneurons inhibit not only pyramidal cells but also soma targeting interneurons while soma targeting interneurons only inhibit pyramidal cells [329] which is considered in our model as well [112].

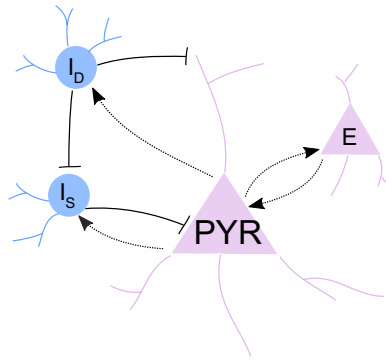


Figure C1 Excitatory inhibitory neuronal population model. The neuronal population model which is composed of excitatory and inhibitory components: pyramidal cells (PYR), excitatory interneurons (E), dendrite targeting inhibitory interneurons (I_D) and soma targeting inhibitory interneurons (I_S).

The structural configuration of our model is presented in Fig.C1 where PYR represents the pyramidal cells, E the excitatory interneurons, I_D and I_S respectively the dendrite targeting inhibitory interneurons and soma targeting inhibitory interneurons. In our model, presented in Eq.C3, each of these neural population subsets is characterized by two components: an activation function and a linear transfer function. The activation function describes a nonlinear relationship between the average postsynaptic potentials and the output firing rate for each neural population which is a bell shaped function in our model (Eq.C4) and presented as F in Eq.C3. The linear transfer function transforms the average presynaptic firing rate into average postsynaptic membrane potential with the impulse response $h_e(t)$, $h_d(t)$ and $h_s(t)$ respectively for excitatory,

dendrite targeting inhibitory and soma targeting inhibitory populations. The impulse responses are defined as below:

$$\begin{aligned}
 h_e(t) &= \frac{At}{\tau_a} e^{-\frac{t}{\tau_a}} \\
 h_d(t) &= \frac{Bt}{\tau_d} e^{-\frac{t}{\tau_d}} \\
 h_e(t) &= \frac{Gt}{\tau_g} e^{-\frac{t}{\tau_g}},
 \end{aligned} \tag{C1}$$

where $t > 0$. A, B and G show the synaptic gains and τ_a , τ_b and τ_g represent the time delays and respectively equates $1/a$, $1/b$ and $1/g$. Each of these linear transfer functions (Eq.C-1) could be written as a second order ordinary differential equations as below:

$$\ddot{y}(t) = Wgx(t) - 2g\dot{y}(t) - g^2y(t), \tag{C2}$$

where $x(t)$ represents the input and for coupling the differential equations to formulate our model (Eq.C3), it is replaced by the activation function outputs.

$$\begin{cases}
 \ddot{y}_1(t) = AaF_e[y_2(t), y_3(t), y_4(t)] - 2a\dot{y}_1(t) - a^2y_1(t) \\
 \ddot{y}_2(t) = Aa\{P(t) + C_2F_e[C_1y_1(t), 0,0]\} - 2a\dot{y}_2(t) - a^2y_2(t) \\
 \ddot{y}_3(t) = BbC_4F_s[C_3y_1(t), 0,0] - 2b\dot{y}_3(t) - b^2y_3(t) \\
 \ddot{y}_4(t) = GgC_7F_d[C_5y_1(t), C_6y_5(t), 0] - 2g\dot{y}_4(t) - g^2y_4(t) \\
 \ddot{y}_5(t) = BbF_s[C_3y_1(t), 0,0] - 2b\dot{y}_5(t) - b^2y_5(t)
 \end{cases} \tag{C3}$$

$$F_j(E, I_D, I_S) = \frac{2e_0}{1+e^{-\frac{(E-(v_j+I_D+I_S))}{r_j}}} * \frac{1}{1+e^{-\frac{(E-(v_j+I_D+I_S)-\theta_j)}{r_j}}} \tag{C4}$$

This system of ordinary differential equations (Eq.C3) is then solved using the fourth order Runge-Kutta numerical integration methods in Matlab.